CIVIL ENGINEERING STUDIES
Illinois Center for Transportation Series No. 16-015
UILU-ENG-2016-2015
ISSN: 0197-9191

INTEGRAL ABUTMENT BRIDGES UNDER THERMAL LOADING: NUMERICAL SIMULATIONS AND PARAMETRIC STUDY

Prepared By
James M. LaFave
Larry A. Fahnestock
Beth A. Wright
Joseph K. Riddle
Matthew W. Jarrett
Jeffrey S. Svatora
Huayu An
Gabriela Brambila
University of Illinois at Urbana-Champaign

Research Report No. FHWA-ICT-16-014

A report of the findings of

ICT PROJECT R27-115
Analysis of Superstructures of Integral Abutment Bridges

Illinois Center for Transportation

June 2016

TECHNICAL REPORT DOCUMENTATION PAGE

1. Report No.	2. Government Accession No.	3. Recipient's Catalog No.
FHWA-ICT-16-014		

4. Title and Subtitle	5. Report Date
Integral Abutment Bridges Under Thermal Loading: Numerical Simulations and Parametric Study	June 2016
	6. Performing Organization Code

7. Author(s)	8. Performing Organization Report No.
James M. LaFave, Larry A. Fahnestock, Beth A. Wright, Joseph K. Riddle, Matthew W. Jarrett, Jeffrey S. Svatora, Huayu An, and Gabriela Brambila	ICT-16-015 UILU-ENG-2016-2015

9. Performing Organization Name and Address	10. Work Unit No.
Illinois Center for Transportation Department of Civil and Environmental Engineering University of Illinois at Urbana-Champaign 205 North Mathews Avenue, MC-250 Urbana, IL 61801	N/A
	11. Contract or Grant No. R27-115

12. Sponsoring Agency Name and Address	13. Type of Report and Period Covered
Illinois Department of Transportation (SPR) Bureau of Material and Physical Research 126 East Ash Street Springfield, IL 62704	March 1, 2012 – May 31, 2016 (interim report)
	14. Sponsoring Agency Code FHWA

15. Supplementary Notes

Conducted in cooperation with the U.S. Department of Transportation, Federal Highway Administration, and the Illinois State Toll Highway Authority.

16. Abstract

Integral abutment bridges (IABs) have become of interest due to their decreased construction and maintenance costs in comparison to conventional jointed bridges. Most prior IAB research was related to substructure behavior, and, as a result, most limit states that have been considered in design guidelines have been based on substructure considerations. However, integral abutment construction also affects superstructure behavior and demands, and superstructure properties directly influence substructure behavior. This report presents numerical simulations evaluating the behavior of IABs with composite steel I-girders subjected to temperature changes consistent with seasonal fluctuations in the state of Illinois. Nonlinear bridge models are introduced in which key parameters are varied, such as span length, pile size, and skew. Other parameters that were deemed of less importance, like various pile and soil conditions, are studied as well. Three-dimensional finite element model results indicate that longitudinal bridge movement is directly dependent on IAB effective expansion length (EEL), regardless of other bridge design parameters. Structural responses such as girder superstructure elastic stress and pile substructure inelastic strain are influenced by EEL, pile type and size, superstructure rotational stiffness, and bridge skew. Results presented herein suggest that superstructure geometry—including bridge skew—should be considered in IAB substructure design and that thermally induced stresses and strains should be considered in superstructure and substructure design.

17. Key Words	18. Distribution Statement
Integral Abutment Bridges; Skewed Bridges; Thermal Loading; Steel I-Girders; Steel H-Piles; Pile Strain; Girder Stress; Superstructure-Substructure Interaction; Effective Expansion Length; Numerical Models.	No restrictions. This document is available through the National Technical Information Service, Springfield, VA 22161.

19. Security Classif. (of this report)	20. Security Classif. (of this page)	21. No. of Pages	22. Price
Unclassified	Unclassified	67 pp.	

Form DOT F 1700.7 (8-72) **Reproduction of completed page authorized**

ACKNOWLEDGMENT, DISCLAIMER, MANUFACTURERS' NAMES

This publication is based on the results of **ICT-R27-115, Analysis of Superstructures of Integral Abutment Bridges**. ICT-R27-115 was conducted in cooperation with the Illinois Center for Transportation; the Illinois Department of Transportation; the U.S. Department of Transportation, Federal Highway Administration; and the Illinois State Toll Highway Authority.

Members of the Technical Review panel were the following:

- Mark Shaffer, TRP Chair, Illinois Department of Transportation
- Nick Barnett, Illinois Department of Transportation
- Bill Flannigan, AECOM
- Steven Gillen, Illinois State Toll Highway Authority
- Chad Hodel, WHKS & Co.
- Micah Loesch, Federal Highway Administration
- Matt Pregmon, AECOM
- Kevin Riechers, Illinois Department of Transportation
- Bob Tessiatore, AECOM
- Dan Tobias, Illinois Department of Transportation

EXECUTIVE SUMMARY

Due to their lower maintenance and construction costs, as well as longer service life, integral abutment bridges (IABs) have gained popularity throughout the United States, although design practices still vary widely across the country and certain aspects of their structural behavior are still not fully understood. Most existing IAB research has focused on substructure demands, which have driven the design limit states considered by entities such as the Illinois Department of Transportation (IDOT). However, recent studies showed that significant forces might develop in the superstructure and, therefore, superstructure behavior should not be ignored in design. The goal of this research project was to investigate a broad range of parameters associated with IAB superstructure behavior in order to provide better-suited design recommendations. This would build upon the recommendations provided by two previous University of Illinois studies on IAB substructures.

Three-dimensional numerical models of IABs, including bridge superstructures, abutments, piers, and pile foundations, were developed in SAP2000 and used to determine structural demands for IABs subject to uniform temperature changes. Models were run using nonlinear analysis for various combinations of dead, thermal, and live loads. Based on AASHTO design provisions and communication with IDOT, a temperature change range of –80°F to +80°F was used. The parameters of this study were divided into primary and secondary categories. A much larger suite of models was evaluated for the primary parametric study, with bridges that had composite steel I-girders, a loose sand abutment backfill, a medium-stiff clay pile soil, and H-pile foundations (oriented with the web perpendicular to the bridge longitudinal axis). The parameters that were deemed most important in affecting IAB behavior, and thus used as variables to develop the suite of models, were abutment skew (ranging from 0° to 45°), pile size, span length, and number of spans. Secondary design parameters, studied in less detail, were end-span length, total width, extreme skew (60°), backfill springs, soil springs, pile orientation, number of piles, pile top relief, pile type, and abutment height. For most of the secondary study, only non-skew bridges with 100 ft spans and HP14×73 piles were used. Except for the parameter of interest, all other design variables were set to the default used in the primary study.

The three key issues related to IAB behavior that need to be considered in design were determined to be bridge displacement at the deck level (requiring some form of expansion detail), strains that develop in the piles due to integral abutment construction, and additional stresses that develop in the girders. Results from the base study showed that global movement can be simply predicted because it was seen to be directly proportional to effective expansion length (EEL). Regardless of span length or pile size, global movement was consistently around 90% of free expansion. However, proper expansion joint detailing at the end of an approach slab may be required to accommodate this predicted movement. Generally, increased bridge skew resulted in complicated bridge deck displacements, including amplified displacements at the acute bridge corner. Special detailing may also be required at the corners of highly skewed single-span bridges to accommodate the movement amplified by bridge rotation in plan.

Proper pile selection can allow for much longer permissible bridge lengths. Pile strain limits beyond yield strain can allow for permissible IAB lengths to increase, especially with the use of larger pile

sections. As expected, increased pile size acted to decrease total pile strains because more demand would be placed on the girders. However, pile strain demands were seen to be significantly exacerbated by abutment skew. The amplified displacements caused by skew resulted in larger pile biaxial bending moments. For a select four-span bridge, as skew was increased from 0° to 60°, the acute pile strain from a temperature change of +80°F alone increased from 0.00195 to 0.00550.

Girder stresses that develop in IABs due to thermal effects can be significant, particularly for bridges with large EEL and large pile sizes. Increased bridge skew was seen to decrease girder strong-axis demands but increase girder weak-axis bending. Thus, non-skew cases were most critical for girder stress demands because skew tended to reduce the longitudinal restraint placed on the bridge girders. For extreme non-skew cases, stresses at the abutment approached 25 ksi. Larger rotational restraint, which is a factor of the span length, was also seen to increase the magnitude of bottom fiber stress for a given girder design.

The following are key results from the secondary parameter study:

- Smaller end spans increased the superstructure rotational stiffness of the bridge. Greater rotational restraint acted to increase both pile strains and girder stresses.
- Larger widths were seen only to have an effect on pile demands. The effect of width was small for non-skew bridges, but it gained significance as skew was increased. A 30° skew bridge with four 100 ft spans experienced a 33.7% increase in pile strain when the width was increased from 36 ft to 96 ft. This is because the larger width acted to amplify the already increased transverse bridge movement caused by skew.
- Stiffer backfill increased relief of the pile head demands but caused larger internal forces and increased superstructure demands.
- Stiffer foundation soil increased pile strains by restraining pile deformations. Soft clays and loose sands allowed for more pile flexibility; thus, smaller forces and moments were distributed to the pile section and smaller girder demands were imposed. Similarly, stiff clays and dense sands reduced pile flexibility, which increased pile and girder demands.
- Pile top relief, which is the practice of encasing the top several feet of the pile foundation in a soft fill, acted similarly to softer foundation soils. These models resulted in larger pile deflections and decreased bending moment demands.
- Models with double piles (placing a pile both underneath each girder and in between) increased the foundation stiffness and reduced pile deflection, which reduced peak pile strains but increased internal forces.
- Pipe piles and strong-axis-oriented H-piles were seen to provide more lateral stiffness and moment capacity. However, their section properties heavily influenced pile biaxial demands and upon yielding pile stiffness (and stability) sharply decreased with increased lateral loads. Therefore, weak-axis bending was observed to be the preferred pile detail because it did not display any detrimental pile section stiffness loss after yielding.

- Deeper abutments resulted in reduced pile strains and deflections but increased girder stresses.

As a result of these studies, design aids and recommendations were developed. Nonlinear regressions were run using results from the primary parameter models to develop predictor equations for peak pile strains and girder stresses due to thermal loading. Additionally, comparisons were made to the current IDOT pile charts, but it was noted that such charts may be an oversimplification. A design aid that takes into account superstructure rotational stiffness and other key parameters could prove to be more useful. It was recommended that IDOT consider different expansion joint detailing to accommodate the longitudinal movement of longer IABs. This is because results from the numerical models showed that the 2 in. strip seal used by IDOT could accommodate the movement of non-skew bridges with total lengths up to approximately 700 ft only. Finally, it was advised that the use of larger pile sizes (mainly HP16s and HP18s) would be advantageous if longer bridges are desired. They would perform well as long as proper detailing at the abutment ensured that the increased forces from the larger piles could be transferred to the superstructure.

CONTENTS

LIST OF FIGURES

LIST OF TABLES

CHAPTER 1: INTRODUCTION

Integral abutment bridges (IABs) are gaining popularity among departments of transportation within the United States because of their lower maintenance and construction costs, as well as longer service life. Unlike conventional bridges, IABs act as a continuous unit when subjected to thermal loads. This is achieved through the monolithic casting of the abutment and deck, as well as via the embedment of the girders and the pile foundations into the abutment (Figure 1). However, the continuous structural form is more difficult to analyze, and design practice across the nation varies significantly. Many states, including Illinois, have been actively conducting research on IABs. Two research projects were conducted in Illinois from 2009 through 2012. Both of them evaluated substructure behavior, and design recommendations were provided based on substructure limit states. Research targeted at IAB superstructure is very limited, and the Illinois Department of Transportation (IDOT) still assumes simply supported end conditions in IAB girder design. However, superstructure behavior is suspected to be affected by integral abutments, and significant forces might develop in the superstructure. Because many uncertainties still remain with respect to IAB superstructure behavior and design, a third research project focused on IAB superstructures was initiated. Using the findings of the first two research projects as a starting point, the objective of the present research is to develop more rigorously grounded design recommendations through a detailed suite of numerical simulations and a comprehensive field monitoring program.

This report summarizes the preliminary work done to develop a suitable analysis framework and evaluate various potential modeling strategies before mass-producing 3D bridge models for the large parametric study. The tasks include a brief literature review, selecting parameters and their ranges, designing parametric bridge models following the current requirements of IDOT, and determining the assumptions and procedures for finite element modeling and analysis. Then, the report goes on to discuss results for non-skew and skewed bridges, as well as possible design tools and recommendations that have come from those results. The field monitoring implementation and analysis will be discussed in a subsequent volume of this report.

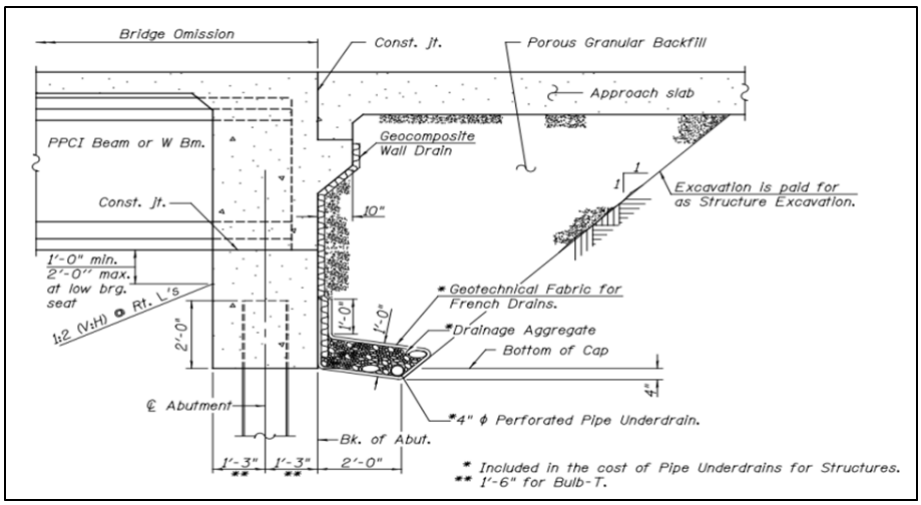

Figure 1. General Illinois Department of Transportation (IDOT) integral abutment detail.

CHAPTER 2: LITERATURE REVIEW

Overall, fairly limited research focus has been placed on IAB superstructure behavior and design. In general, the most important factor for IAB behavior is the effective expansion length (EEL), as has been established in a number of previous studies (Dicleli 2005; Ingram et al. 2004; Paul et al. 2005). In this study, EEL is simply taken equal to half of the overall bridge length, assuming similar soil properties exist at each abutment. However, in cases of asymmetric substructure stiffness, the calculation of EEL can be more involved. Chapter 2 summarizes IDOT practice and other research work that closely relates to the current parametric study.

2.1 IDOT CURRENT IAB DESIGN PRACTICE

The current IAB design guidance, which broadened the permissible IAB range, came out as a memorandum ("IDOT Memorandum," July 2012) to the 2012 IDOT Bridge Manual (IDOT 2012). Longer lengths and larger skews are allowed, and pile orientation changes from the prior configuration. As shown in Table 1, the maximum lengths in the previous practice were only 310 ft for steel girders and 410 ft for concrete girders. The maximum abutment skew was 30°. The current practice allows 550 ft length and 45° skew. (The IDOT IAB length limit will soon be further increased, to 610 ft.) The pile's strong axis used to be oriented co-linear with the abutment axis, but now the pile's weak axis is perpendicular to the bridge center line (the "weak-axis orientation"). The most significant change is in the design philosophy of H-piles. The previous limit state was to avoid pile yielding, which placed too much restriction on design length and skew. The current limit state allows a certain amount of pile yielding, and an Integral Abutment Pile Selection Chart was developed to facilitate pile design. The maximum pile size in the chart is HP14×117, but IDOT recently indicated they would like to permit HP16 and HP18 piles, which would be evaluated in the current research project by modeling piles with full nonlinear behavior near the pile head and applying a strain limit state (research team communication, IDOT).

Other IAB design modifications include eliminating corbel and the pile encasement around H-piles, removing the bar splice between the superstructure and approach slab, and increasing abutment cap widths, etc. Also, mechanically stabilized earth (MSE) abutment walls are not allowed with integral structures, differing from the design of the I-90 over UPRR Bridge (one of the bridges in the field monitoring program).

IDOT does not provide special design guidance for design of IAB superstructures. The girders are designed following the standard process assuming simply supported conditions at abutments and thereby overlooking the potential additional demand in the superstructure induced by the integral abutment (research team communication, IDOT).

Table 1. Changes in IDOT Policy

	Previous IDOT Policy	Current IDOT Policy
Maximum Bridge Length: Steel Girders	310 ft	550 ft
Maximum Bridge Length: Concrete Girders	410 ft	550 ft
Maximum Abutment Skew	30°	45°
Pile Orientation	Strong axis	Weak axis
Pile Limit State	No yielding allowed	Moderate yielding allowed

2.2 REVIEW OF THE PREVIOUS ILLINOIS RESEARCH

The previous IAB research conducted in Illinois consists of two phases, both of which focused on substructure behavior and design. The first phase was completed in August 2009 (Olson et al. 2009), in which 2D and 3D parametric studies were performed. That report concluded that the types of girders, pile soil, and the development of abutment backfill passive pressure have secondary effects on pile foundation performance. It recommended the use of compacted granular backfill, and it provided several options to reduce pile moment in order to release length and skew restrictions. Two bridges were selected and instrumented on the substructures in hope of validating the modeling procedure.

Recognizing the advantages of 3D modeling and analysis, a more comprehensive 3D parametric study was conducted in the second phase, which was completed in May 2012 (Olson et al. 2012). The study suggested that IDOT could consider the combined effects of length and skew and relax skew limitation. H-piles were recommended to be oriented with webs parallel to bridge center line (the "strong-axis orientation") due to lower flange tip stresses. It was concluded that thermal loading, combined with live loading, would create the maximum demands on piles. Even though the time-dependent effect was only slightly investigated in the second phase, supported by the findings of research in Indiana and Pennsylvania, the importance of creep and shrinkage was emphasized, which might significantly alter bridge long-term behavior from considering only thermal and live loadings.

Additionally, the 2012 study solely used the pile head stress "first yield" limit state, which is no longer the suggested limitation from IDOT (research team communication, IDOT). It did not take into account pile plasticity, which has been commonly assumed in the IAB design approaches of many other states (Olson et al. 2012). The design recommendations were provided without considering superstructure behavior. The study did not include bridge width as a parameter, and the girder sections were only approximately selected. To further investigate IAB bridge behavior and to potentially relax length and skew limitation while considering pile plasticity and superstructure behavior, the current project, as the third phase, was initiated.

These two previous studies (Olson et al. 2009, 2012) of Illinois IABs included a fairly extensive summary of the relevant prior research on IAB substructures, as well as information from a survey of other states' practices with respect to the design, construction, and performance of IABs. Therefore, this report will focus on summarizing some limited key recent work on IAB substructures (primarily from the state of Indiana) and then also in particular on IAB superstructures (and how their behavior can be intertwined with that of the substructure).

2.3 IAB SUBSTRUCTURE RESEARCH

A significant amount of research work on IABs has been done at Purdue University in recent years. The previous Illinois research (Olson et al. 2012) summarized most of those findings. Purdue conducted small-scale bridge tests in the laboratory and cyclic load tests on cantilever H-piles. One of the most relevant findings to the current Illinois research is the determination of a pile buckling strain limit. Cyclic load tests were done on different cantilever H-piles under constant axial load (representing bridge gravity load), and the cantilever length was estimated from pile head to first inflection point based on models with different design configurations. Analytical models were developed to match the experimental pile head displacements at pile buckling using a trial-and-error method, and the corresponding analytical extreme fiber strain near the pile head was considered as the buckling strain $\varepsilon_{buckling}$. The average buckling ductility ratio $\varepsilon_{buckling}/\varepsilon_{yield}$ is about 20 for H-piles according to Frosch et al. (2006). IDOT suggested using the strain at initiation of strain hardening as the pile head extreme fiber strain limit, which is approximately 8 to 10 times ε_{yield}, and well below the buckling strain found by Purdue (research team communication, IDOT).

Through a long-term field monitoring program, "ratcheting" of contraction displacements due to deck shrinkage was observed, and the amount of shrinkage contraction controlled over thermal contraction (Frosch and Lovell 2011). The previous and current Illinois numerical analyses ignore time-dependent effects because of the uncertainty about how to model time-dependent demands. This omission may lead to large discrepancies being observed later from field instrumentation data. With skew and shrinkage effects considered, Purdue recommended bridge lengths up to 1100 ft for 0° to 30° skew, and up to 1000 ft for 60° skew using H-piles with proper detailing (Frosch and Lovell 2011).

Another pertinent study on H-pile behavior in IABs was conducted at the University of Tennessee at Knoxville (Burdette et al. 1999). Field tests and numerical analyses were used to study the failure of piles at the abutment interface. In the field tests, seasonal thermal cycles were emulated through a combination of axial and lateral loads until failure occurred. Burdette et al. found that due to the confinement of the pile soil, the pile does not follow typical beam-column interaction. Even more, the confinement allowed the piles to withstand bending moments exceeding their theoretical maximum plastic capacity without losing stability. Pile embedment depth into the abutment was studied as well, with tests involving 1 ft embedment and 2 ft embedment. The tests were conducted in a manner to simulate a fixed pile head condition. It was found that the deeper, 2 ft embedment test case had higher deflection capacity without loss of structural integrity.

2.4 IAB RESEARCH ON SUPERSTRUCTURE BEHAVIOR

Most of the existing research regarding IABs focuses on behavior of the substructure, usually as a function of soil properties at the abutment and its pile foundation. This focus has been motivated by the significant increase in substructure demands for integral construction. As previously stated, EEL has been viewed to have significant influence on IAB behavior, with global bridge superstructure movement and pile displacement demand both being directly related to EEL. Other primary factors affecting IAB pile behavior include the backfill soil stiffness and pile soil stiffness (Dicleli 2005) because a stiffer backfill and less pile restraint can lead to a reduction in pile moments (Civjan et al.

2007). In addition to backfill and pile soil properties, the superstructure can also play a significant role in determining IAB substructure behavior. Most notably, a high degree of fixity in IABs at the connection between the abutment and girders restrains abutment rotation due to thermal movements and consequently causes the piles to deform in double curvature (Khodair and Hassiotis 2005). This interplay between the substructure and superstructure is also mentioned by Burdette et al. (2004), Kim and Laman (2010), and Olson et al. (2012), but there is a need for more detailed investigation of these superstructure effects on pile behavior (and vice versa).

Research done at Pennsylvania State University (Paul et al. 2005) investigated superstructure behavior under thermal loading by instrumenting girder top and bottom at midspan on a four-girder, prestressed concrete slab-on-beam bridge. The field girder forces might be affected by various factors, which are difficult to isolate. However, based on the numerical and field data, creep and shrinkage may significantly affect girder axial forces and calculated thermally induced stresses might lead to cracking. Paul et al. (2005) conducted 2D parametric analysis as well, which confirmed that significant moment and axial and shear forces could be generated in superstructures by seasonal variations in thermal loading. As shown by their results in Figure 2, thermally induced (±80°F temperature change) axial force and moment in the superstructure gains even more significance as EEL is increased. The increase in superstructure forces is due in part to the soil pressure applied to the abutment and piles during expansion and contraction; however, the curves in the plots appear to level off with increasingly large EEL because of nonlinear responses from the abutment and pile soil. They found that a uniform temperature gradient applied to the superstructure is sufficient for determining demands on superstructure and substructure elements; other researchers measured IAB thermal gradients in the field that were somewhat less than code-recommended values (Rodriguez et al. 2014).

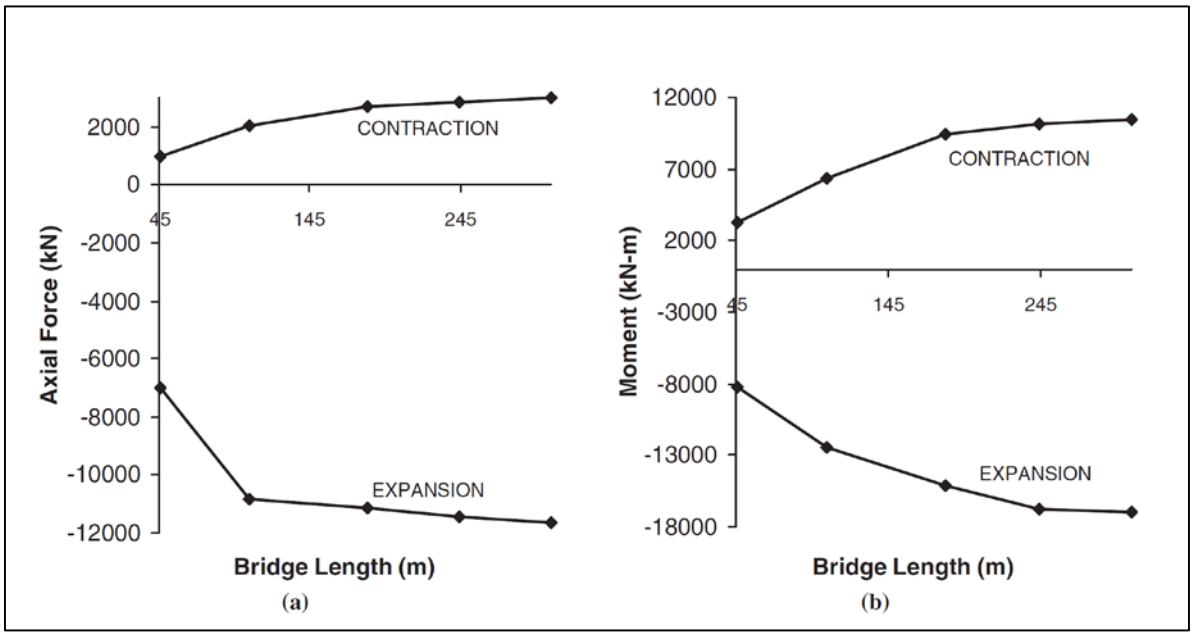

Figure 2. Thermally induced forces as a function of bridge length: (a) axial force and (b) moment. (Paul et al. 2005, Figure 8).

Pennsylvania later conducted similar long-term field monitoring programs on three other prestressed concrete bridges (Kim and Laman 2010), and the importance of thermally induced girder forces were again emphasized. Kim and Laman (2010) concluded that IAB girder bending moments and axial forces due to thermal load are significant and should be considered in design. Their comparison of measured and FEM-predicted data (see Figure 3) for four IABs revealed that girder axial forces are primarily influenced by end-span length, as opposed to overall bridge length. William et al. (2012) found that restrained movement of the integral abutment by the backfill and supporting piles induces axial forces in the superstructure that are not explicitly considered in typical bridge design procedures.

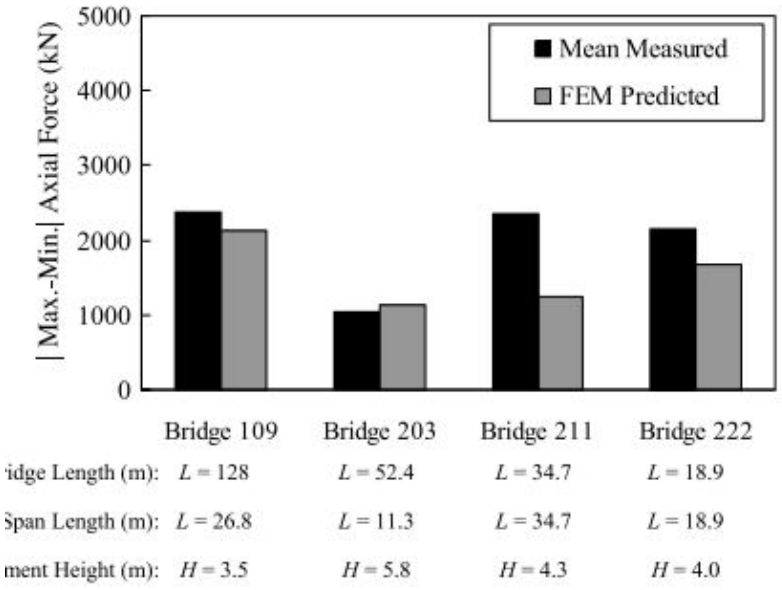

Figure 3. Comparison of thermally induced maximum girder axial force (Kim and Laman 2010, Figure 17).

Minnesota (Huang et al. 2004) also did field monitoring on a bridge with prestressed concrete girders and instrumented various cross-sections of the superstructure. It was found that due to creep and shrinkage, girder strains kept decreasing over the years. Even though girder strain variations across the cross-sections and different bridge locations were explained, no recommendation was provided with respect to modifications of IAB superstructure design. Huang et al. (2008) explored the relationship between girder stiffness and pile stiffness. For example, stiffer piles led to reduced pile stresses but increased girder stresses, whereas more flexible piles (e.g., in weak-axis bending as opposed to strong-axis bending) led to increased pile stresses but reduced girder stresses. Therefore, it appears that a balance needs to be struck between the stiffness of these two key bridge components.

All the girders in the research work discussed above are concrete beams. Because steel girders are mainly used by IDOT on IABs (research team communication, IDOT) and the current parametric study models were all designed with steel girders, the relevance of those studies' conclusions becomes more limited. It was deemed important to conduct a more comprehensive parametric study with heavier emphasis on the behavior and design of IAB superstructures.

CHAPTER 3: PARAMETRIC STUDY ORGANIZATION AND CONSIDERATIONS

A primary portion of the research project is to perform a parametric study for IABs across a number of different parameters. Initially, a full suite of non-skew IABs was studied to thoroughly vet the modeling approach and establish a baseline understanding of fundamental IAB behavior without the added complexity of skew. Afterward, the skewed bridges were studied in detail and compared with that baseline. Once the "base runs" were complete, which included groups of models with 0°, 15°, 30°, and 45° of abutment skew, various secondary studies were performed on less crucial parameters. With the large number of models that would end up being run for the study, it was crucial to have a simple, effective organization system. To accomplish this task, the concept of "runs" was introduced in which each "run" consisted of models with all parameters held constant except the number of spans. This system is outlined in Tables Table 2 and Table 3. The tables summarize all primary models that were run for the study. Note that for smaller pile sizes, not all spans were included; these determinations were made by not allowing the dead load on the piles to exceed 40% of the yield stress.

Table 2. Base Parametric Study Matrix

Batch	Pile Section	Characteristic Span Lengths
1–4	HP14×73	200 ft, 150 ft, 100 ft, 50 ft
5–8	HP14×89	
9–12	HP14×117	
13–16	HP12×84	
17–19	HP12×74	150 ft, 100 ft, 50 ft
20–22	HP12×63	
23–24	HP10×57	150 ft, 100 ft
25	HP10×42	50 ft
26	HP8×36	
27–29	HP16×101	200 ft, 150 ft, 100 ft
30–32	HP16×183	
33–35	HP18×135	
36–38	HP18×201	

Table 3. Example of a Batch Within the Parametric Study Matrix (Batch 1)

Model #	Span Name	Girder Name	EEL	Pile Section
1	1×200	PG76	100 ft	HP14×73
2	2×200	PG76	200 ft	HP14×73
3	3×200	PG76	300 ft	HP14×73
4	4×200	PG76	400 ft	HP14×73

Key parameters of this study were designated as primary or secondary. Abutment skew, pile size, span length, and number of spans (and, therefore, overall bridge length) were identified as the

primary parameters comprising the base study models, as defined above and in Tables Table 2 and Table 3.

A less detailed study was conducted on bridge variables deemed as secondary parameters. These parameters are listed in Table 4. (And there are still other possible secondary parameters—for example, intermediate support stiffness—that are simply beyond the scope of this study.) Each secondary parameter was analyzed with non-skew bridges of 100 ft spans, ranging from one to six spans, with HP14×73 piles (unless the secondary parameter requires a different pile). The "default" model referenced in the table contains 100 ft spans with HP14×73 piles (weak-axis orientation, spacing equal to that of the girders), backfill consisting of loose sand, and pile foundation soil consisting of medium-stiff clay. Numerical models representing secondary parameters differ from the default model only by end-span length, total width, bridge skew (in the case of the extreme skew bridges), backfill springs, soil springs, pile orientation, number of piles, pile top relief, pile type, or abutment height.

Table 4. Numerical Models Used to Evaluate Secondary Parameters

Model	Change from Default
Default	N/A
End-Span Ratio*	End spans have different length from interior spans (different superstructure rotational stiffness)
Width*	Bridge width is increased
Extreme Skew**	60° skew with altered meshing scheme
Stiff Clay	Soil springs represent stiff clay
Medium-Soft Clay	Soil springs represent medium-soft clay
Dense Sand	Soil springs represent dense sand
Loose Sand	Soil springs represent loose sand
Stiff Backfill	Backfill springs represent dense sand
Abutment	Abutment height increased
Double Piles	Pile spacing decreased (number of piles increased)
Pile Relief	Top 10 ft of soil springs adjusted to model bentonite slurry
Strong Axis	Piles oriented for strong-axis bending
Pipe 16×0.312	H-piles replaced by pipe pile with 0.312 in. thickness
Pipe 16×0.375	H-piles replaced by pipe pile with 0.375 in. thickness

*A more detailed study was conducted aside from the base secondary parameter models.

** This parameter will be discussed along with the primary parameters.

3.1 ABUTMENT SKEW

Due to the uncertainty of abutment backfill pressure modeling in the previous Illinois research, IDOT currently limits bridge skew to 45° (research team communication, IDOT). Therefore, the bulk of the parametric study consists of bridges with abutment skew up to only 45°. However, to investigate some more extreme behaviors, a select group of bridges were examined with abutment skew of 60°.

3.2 PILE SIZE

To encapsulate a wide variety of bridge configurations, pile sizes ranging from HP 8×36 to HP 18×204 were used in the study. By including a broad spectrum of piles, extreme behaviors could be observed. The current IDOT Integral Abutment Pile Selection Chart was not used in the design of piles for each bridge; however, analyzed strain values were compared with the various limits enforced by the chart.

3.3 INDIVIDUAL ("CHARACTERISTIC") SPAN LENGTH

The current IDOT policy limits the maximum single-span bridge length to 170 ft, and the maximum end-span length for multi-span bridges is limited to 200 ft. For this reason, the parametric study models have a maximum characteristic span length of 200 ft. This study includes models with characteristic span lengths of 50, 100, 150, and 200 ft (regardless of whether spans as long as that would necessarily be used for precast prestressed concrete superstructures, as they are in fact sometimes used in the case of structural steel superstructures).

3.4 OVERALL BRIDGE LENGTH

Bridges with total lengths ranging from 100 to 1200 ft were examined in this study. According to IDOT correspondence and the IDOT Integral Abutment Pile Selection Chart, the current maximum IAB length is 550 ft. However, previous University of Illinois IAB researchers have suggested that longer bridges are feasible. The limiting factors for overall bridge length include the following: overall bridge deformations that must be accommodated by an expansion detail at the approach slab–transition slab interface, extreme fiber strains at the top of the H-piles, and the build-up of additional stresses in the superstructure due to thermal loading combined with integral construction. Currently, IDOT uses a strip seal with an allowable range of ±2.5 in., according to the fabricator. This range is reduced by AASHTO to ±2 in. of movement (research team communication, IDOT). The joint is adjusted at the time of installation based on the current temperature such that the joint will be able to accommodate movement for the full range of temperatures expected in that particular geographic area, according to the AASHTO maps. In the future, a different type of seal could be used with a higher deformation capacity; therefore, IDOT made the decision not to limit this research to bridges with an expansion of less than 2 in.

3.5 SUPERSTRUCTURE ROTATIONAL STIFFNESS

Preliminary research showed that the rotational restraint the superstructure provides to the substructure is a critical variable governing IAB behavior. In a sense, this value is a primary parameter as it is implicitly varied along with span length. In this study, the rotational restraint has been defined as the parameter k_θ. To first determine this value, an elastic model of the superstructure was created, with fixed supports at the abutments and pin support conditions elsewhere. At one "abutment," a moment causing bending was then applied, and the resulting rotation at the "abutment" was noted. The superstructure rotational stiffness, k_θ, was taken as the moment divided by the rotation. A schematic of this concept can be seen in Figure 3. As the number of spans increases, the value of k_θ becomes nearly constant. Table 5 lists the rotational stiffnesses used to characterize the various bridge configurations of this study.

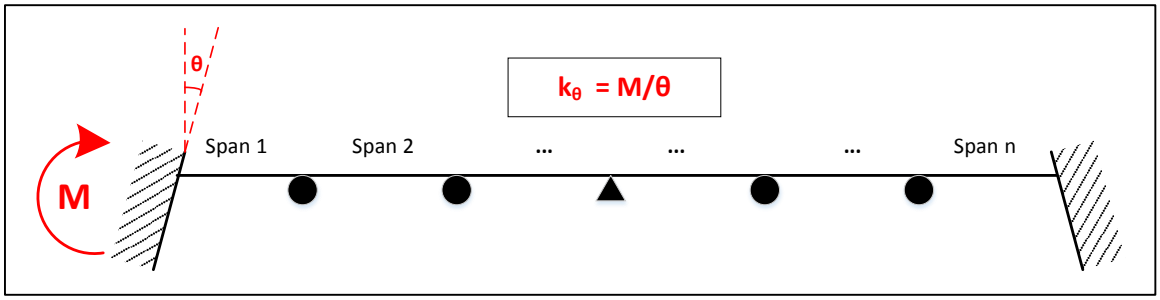

Figure 3. Superstructure rotational stiffness calculation.

Table 5. Superstructure Rotational Stiffness Values for Given Span Length Combinations

Span Case Name	Interior-Span Length (ft)	End-Span Length (ft)	Girder Designation	Abutment Height (ft)	k_θ (10^6 k*in./rad)
150	150	150	PG76	10.56	7.90
150–200	200	150	PG76	10.56	7.72
200	200	200	PG76	10.56	5.92
50–100	100	50	W36×194	7.27	4.67
100	100	100	W36×194	7.27	2.45
50	50	50	W24×84	6.24	1.33

3.6 END-SPAN RATIO

IDOT has indicated that 2:1 is a reasonable upper limit for end-span ratio (research team communication, IDOT). Models with varying end-span ratios (see Table 5) have been created and analyzed (the end-span girder size was not altered in such cases, although this could of course be done as part of future work). As expected, smaller end spans result in larger k_θ values for a given EEL.

3.7 BRIDGE WIDTH

Typical IDOT IAB designs are in the range of 30 to 50 ft wide, while a few bridges exceed 100 ft in width. The research team decided to use 36 ft as the default, which was also the only bridge width considered in the previous Illinois research (Olson et al. 2012). However, a more selective group of wider bridges, with widths of 60 and 96 ft, have been analyzed in this current study as well. Girder and lane arrangements are also taken into account with bridge width. All parametric study bridges were designed with a 6 ft girder spacing, providing a 3 ft deck overhang beside the edge of the girders. With each vehicle lane being 12 ft wide, the three different widths used in this study comprise two lanes and two 6 ft shoulders, three lanes and two 12 ft shoulders, and six lanes and two 12 ft shoulders, respectively. The 48 ft width option was eliminated because it was advised as uncommon by IDOT (research team communication, IDOT).

3.8 PILE SOIL STIFFNESS

Based on IDOT suggestions, the default pile soil was chosen as a medium-stiff clay with an undrained shear strength of 1500 psf (Q_u = 1.5 ksf) and unit weight of 120 pcf. The effects of stiffer and softer soils on IAB behavior have been investigated as well, on a more limited basis. Pile foundation soil properties for these models range from soft clay (s_u = 1000 psf) to stiff clay (s_u = 3000 psf) and loose sand to dense sand.

3.9 ABUTMENT BACKFILL STIFFNESS

It was indicated by IDOT that compacted backfill, as well as maximized abutment wall friction, might be beneficial to reduce the rotational demands of abutment piles during thermal expansion (research team communication, IDOT). However, stiffer backfill might induce excessive axial force demand on the superstructure. Additionally, uncompacted backfill can be expected to consolidate due to vibratory compaction caused by vehicles crossing the bridge. Because uncertainty still prevails, it was decided that the default abutment backfill soil should be uncompacted, based on the current IDOT policy.

The assumed default backfill was set with the properties of a loose sand with unit weight of 115 pcf and a friction angle Φ of 30°. For the secondary parameter study, backfill properties ranging from loose sand (uncompacted, Φ = 30°, γ = 115 pcf) to dense sand (compacted, Φ = 45°, γ = 130 pcf) were examined.

3.10 PILE TYPE, ORIENTATION, AND LOCATION

3.10.1 Type

The default pile type of this study was the steel H-pile. Steel pipe pile sections were also examined, with 16 in. outside diameters and thicknesses of 0.312 in. and 0.375 in. (material = A992).

3.10.2 Orientation

The current IDOT policy orients H-piles such that pile web is perpendicular to the longitudinal direction of the bridge (i.e., the “weak-axis orientation”). This is contrary to the recommendations of the former University of Illinois researchers who used the “first yield” limit state. For most IABs with moderate skew, weak-axis orientation provides more flexibility due to smaller pile bending stiffness, which reduces the restraint on a superstructure under thermal loading. Therefore, weak-axis orientation agrees better with the current IDOT IAB girder design procedure, assuming simply supported boundary conditions at abutments (research team communication, IDOT). Weak axis–oriented piles tend to reach first yield more easily and rely on pile nonlinearity and ductility; however, because first-yield performance criterion was abandoned and nonlinearity has been modeled at the pile top in this parametric study, weak-axis orientation might prove to be more advantageous. For a selected group of models, the effects of strong-axis orientation were also explored.

3.10.3 Location

The default model configuration consists of one pile directly underneath each girder. To provide more options for the designer and further understand the effects of pile stiffness on a superstructure, a select group of models was run with "double piles," meaning that there are piles directly beneath and in between the girders (i.e., a six-girder bridge would have 11 piles).

3.11 PILE TOP RELIEF

The default models for the primary study include no additional relief near the top of the pile. However, both of the bridges instrumented as part of the field monitoring program were constructed with 10 ft pre-drilled holes backfilled with soft material at the pile head. Pile top relief is used in order to reduce demands placed on the pile. Because of its practical applications, pile top relief was included in the secondary parameter study.

CHAPTER 4: DESIGN, MODELING, AND ANALYSIS

4.1 GENERAL DESIGN AND MODELING STRATEGY

Parametric study bridges were designed in accordance with IDOT and AASHTO standards, after their general configurations and proportions were first determined using plans from similar existing IDOT bridges. Finite element models were created using the structural analysis program SAP2000 v14 (CSI 2009). Figure 4 illustrates a typical model configuration for the study.

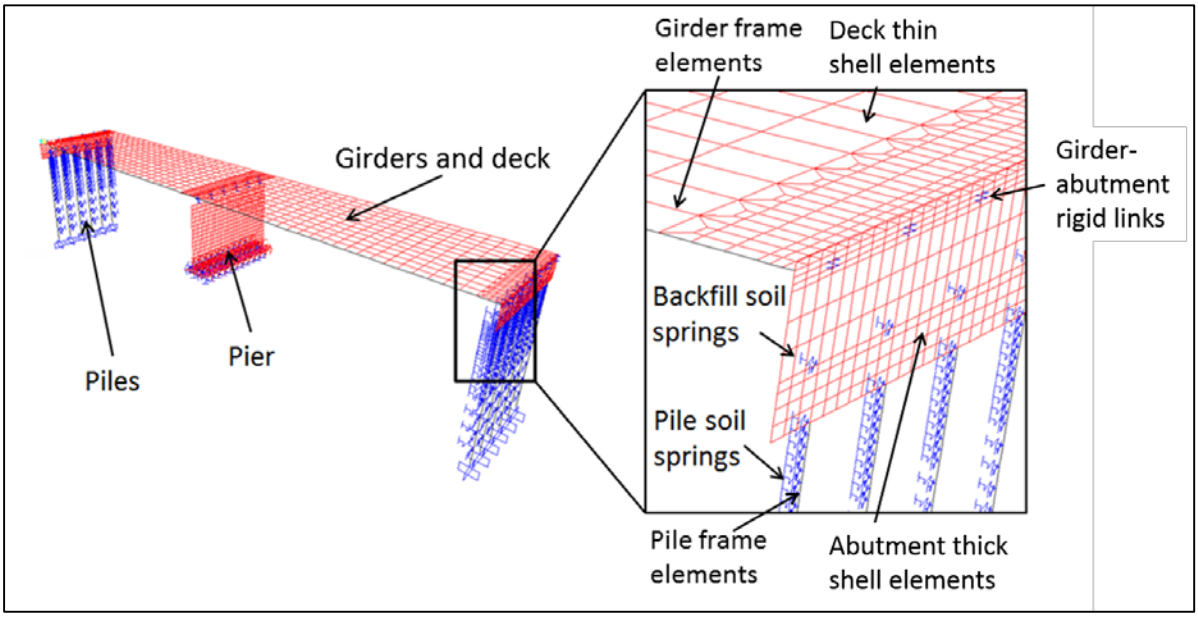

Figure 4. Finite element model of integral abutment bridge.

4.1.2 Deck and Abutments

Standard dimensions for deck and abutment were taken from the IDOT Bridge Manual. The deck of the study models was designed to be 8 in. thick. The abutment height equals the deck thickness (8 in.) plus the concrete fillet (0.75 in.) plus girder depth plus abutment cap depth (42 in.). The standard integral abutment cap width is 40 in. for steel beam bridges and 44 in. for concrete beam bridges ("IDOT Memorandum," July 2012). Therefore, the abutment varies only in height with respect to girder depths and is not an independent variable in the parametric study. The cold joint between the two parts of an integral abutment has also been assumed as fixed (research team communication, IDOT). Following the design of the instrumented bridges, deck concrete was given a compressive strength of 4000 psi and abutment concrete was given a compressive strength of 3500 psi.

Thin and thick shell elements were used for deck and abutment modeling, respectively. Based on the assumption that minimal cracking occurs under service loading, these elements were modeled as linear elastic without reinforcement.

4.1.3 Girders

All parametric study models were designed with wide flange sections or plate girders. Girder dimensions were designed according to the IDOT Bridge Manual (2012), per IDOT LRFD Composite Steel Beam Design Guide 3.3.4, as well as the AASHTO LRFD Bridge Design Specifications (6th edition, 2012). The design assumed that all girder ends had simply supported boundary conditions at abutments and therefore did not account for any effects of integral construction. Girders were designed for both positive and negative moment regions. Using influence lines and trial-and-error analysis on line models in SAP2000, the maximum moment and shear demands for the positive and negative girder moment regions were computed for each bridge for the constructability limit state, service limit state, and strength limit state. Fatigue moment demand was determined using load train analysis in F-Tool. A fatigue truck went from one end to the other on each bridge line model at a small distance increment, and then the local maximum positive and negative moments at each bridge point were recorded after comparing all the truck locations. The maximum moment differences were found for positive and negative girder moment regions using a spreadsheet.

Minimum girder depths were initially determined by using the girder depth to span length ratios from the AASHTO LRFD Bridge Design Specifications and the recently designed IDOT IABs. The girder design followed an iterative process in which girder dimensions were modified to provide adequate capacity that exceeded the calculated demands. Standard rolled wide-flange sections (W24×84 and W36×194) made of AASHTO M270 Gr. 50 steel were selected as the girders for 50 and 100 ft spans, respectively, with only one section chosen for both positive and negative moment regions. For 200 and 150 ft spans, 76 in. deep spliced plate girders made of AASHTO M270 Gr. 50 steel were designed, with different sections for positive and negative moment regions. For simplicity, this overall girder configuration was named PG76.

For simplicity in both modeling and post-processing, girders were modeled using frame elements. These elements were made composite with the deck shell elements via the insertion point method (CSI 2013), with the girder and deck elements sharing nodes (Figure 5). Girder stiffness was corrected by using an offset at both ends, equal to half deck thickness (4 in.) plus concrete fillet thickness (0.75 in.), while the insertion point was at the middle of the top flange. This software configuration was proved to be accurate by some additional composite beam analysis in SAP2000, as well as comparison with hand calculations.

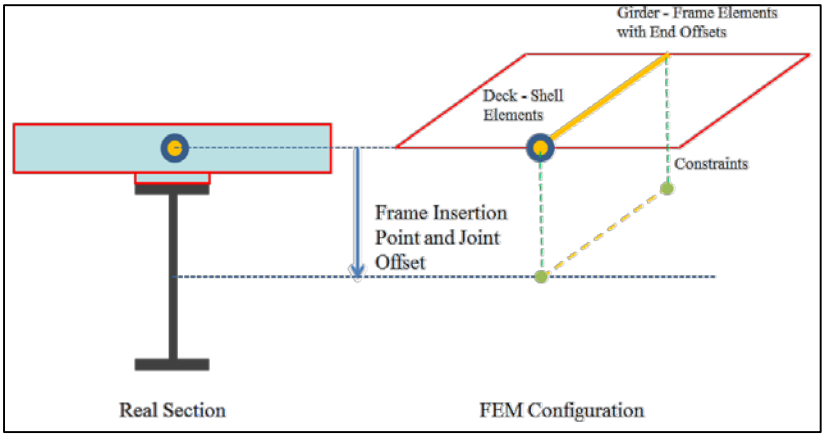

Figure 5. Composite section modeling and girder end offset (adapted from CSI Technical Knowledge Base "Composite Section Tutorial").

Unlike the simply supported approximation used to initially design the girders, a fixed connection was assumed when modeling due to the nature of the girder embedment in the abutment. A rigid link was used to attach the girder frame elements to the abutment shell elements.

4.1.4 Piers

Based on IDOT correspondence and the design of the instrumented bridges, bridges with an even number of spans have fixed bearings at the middle pier and expansion bearings elsewhere. Bridges in the parametric study that have an odd number of spans have all expansion bearings. At the fixed bearings, a wall pier was designed that mimics the design of one of the field monitoring bridges (I-90 over the Kishwaukee River). The pier height is 25 ft, and the footing is 9 ft wide by 4 ft thick. Piles underneath the pier footing are metal shell 14 × 0.312 in., spaced at every 3 ft and extending 50 ft down from the footing.

Like the abutments, the intermediate pier is modeled with thick shell elements. Below the wall pier footing, each pile is represented by a linear 6-DOF nodal spring. Spring stiffnesses were calculated primarily in LPILE (Ensoft 2005) by applying a small deformation at the pile top with proper boundary conditions in each degree of freedom. Torsional and axial stiffnesses were computed by hand. The fixed bearings connecting the intermediate pier to the bridge superstructure were modeled as rigid links, while the expansion elastomeric bearings were modeled as rollers.

4.1.5 Piles

As indicated in Section 3.1, piles were not designed for each bridge; rather, piles served as a primary parameter to be varied in the different "runs" of the study.

Piles were modeled using frame elements, fixed at a depth of 40 ft. To account for nonlinear behavior in the critical region, a series of 6 in. long elements with fiber section hinges were used for the top 5 ft of each pile. A fiber section comprises 60 fibers (20 for each flange and 20 for the web); web-flange fillets were not modeled. Each fiber behaves according to a uniaxial nonlinear strain–strain relationship, and the individual fiber responses are integrated over the cross-section, with overall

member behavior determined considering a hinge length equal to the length of the element. Like the girders, piles were assumed fixed to the abutment. The pile–abutment interface was modeled as rigid by constraining the degrees of freedom of the pile frame element to the degrees of freedom of the shell elements representing the bottom of the abutment.

4.1.5.1 Length of Pile Yield Region

The length of yield region on a pile can be approximated by the distance from the pile head down to where first yield occurs. Because the piles use the weak-axis orientation and minor moment is much larger than major moment for most of the parametric models, only minor moment is used in the calculation of yield region length. IDOT suggested that the limit of pile head extreme fiber strain should be the strain at initiation of strain hardening (research team communication, IDOT), which was assumed to be ten times the yield strain for this calculation. Based on the strain and stress distribution at the pile head as shown in Figure 6(a), pile head moment should be very close to plastic moment M_p. Figure 6(b) illustrates that using similar triangles, the length of yield region (or softening region) L_s can be obtained from the distance L between the pile head and the first inflection point.

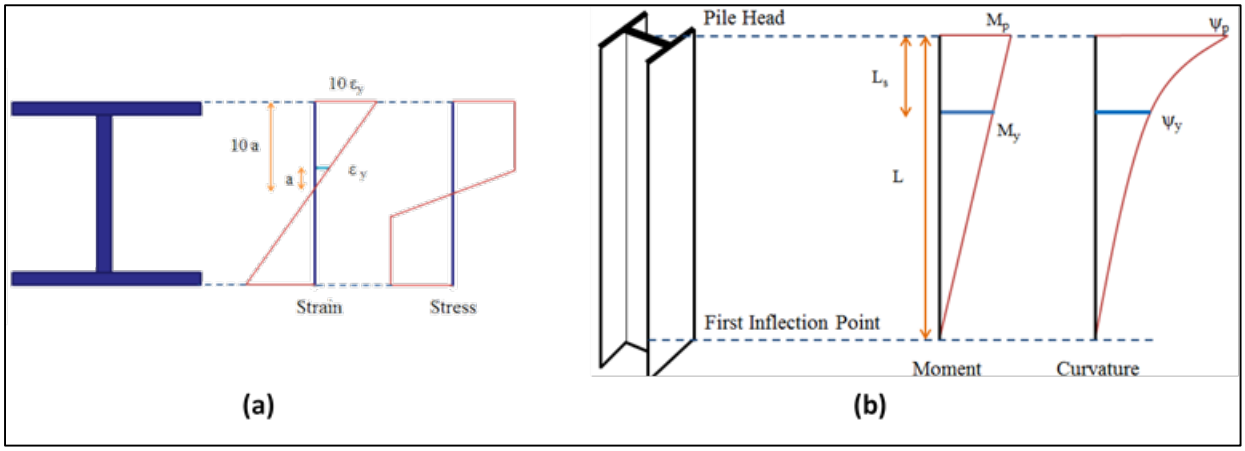

Figure 6. Calculation for length of yield region near pile head.

Based on bridge models with lengths varying from 400 ft to 1000 ft, the distance L between the pile head and first inflection point is about 5 ft. Using similar triangles, L_s is:

$$L_s = L\,(M_p - M_y) / M_p = L\,(Z_{yy} - S_{yy}) / Z_{yy}$$

The ratio $(Z_{yy} - S_{yy}) / Z_{yy}$ is about 0.35 for all the HP14 piles; therefore:

$$L_s = 0.35\ L = 0.35 \times 5 = 1.75\ \text{ft}$$

Pile fiber hinges were assigned for 1.5 ft downward from the pile head for several models with lengths from 400 ft to 1000 ft, and the bottom hinge always showed linear behavior with extreme fiber stress below yielding. Therefore, the approximated softening length is reasonable.

4.1.5.2 Individual Hinge Length

To facilitate post-processing, only one fiber hinge is assigned at the middle of each frame element and occupies the entire element length; thus, the element nodal displacements and forces can be used to calculate hinge behavior through MATLAB automatically. The gradients of pile curvature and extreme fiber strain become much greater when pile moment gets close to full plastic moment near the pile head. Therefore, to more accurately represent the yield region, individual hinge length must be shortened near the pile head. The topmost fiber hinge has the greatest curvature gradient and consequently must be very small to correctly capture the pile head strain, which is of the most interest at this particular location.

A comparison test was performed on a bridge with four 100 ft spans and 2.5 times the normal thermal loading. When the topmost element (or fiber hinge) had a length of 0.5 in., for which the hinge location was at 0.25 in. from pile top, the curvature should be very close to the actual pile head curvature. However, a smaller length is always more accurate. Also, the hinge might be assigned at the top node instead of the middle of the topmost element to provide a direct output of hinge results at the pile head. This approach might soften the piles a little bit, but that effect appeared to be negligible on the test model. In the end, fiber hinges were placed at the middle of frame elements for the top 5 ft of pile.

4.1.6 Superstructure Meshing

Deck stresses and girder forces can be inaccurate near the abutment–superstructure connections due to stress concentrations and force transfer between various elements and links. According to tests on several simple strip models, the composite force transfer at the abutment–superstructure connection is accurate; however, the deck stress and girder force individually are incorrect within the two to three lines of elements near the connections.

For this reason, a refined meshing pattern, shown in Figure 7, was developed for the parametric study models. Near each abutment or pier, the deck is divided into three parallel strips containing small quadrilateral elements, and larger elements take their place after a gradual mesh transition.

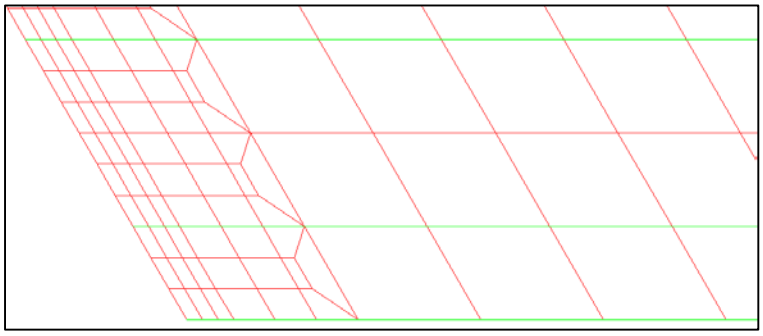

Figure 7. Final meshing pattern near supports.

However, this meshing pattern loses accuracy with skews above 45°. According to the CSI SAP2000 Manual, the inside angles of a quadrilateral should be within 45° to 135°. With skews beyond 45°, the

interior angles of all of the elements become either less than 45° or greater than 135°. Therefore, for the select 60° skew models created, a new triangular meshing scheme was developed (Figure 8). The triangular elements satisfy mesh preferences of nearly 60° corner angles, which prevents ill-conditioning that the quadrilateral elements would create for these extreme skew bridges.

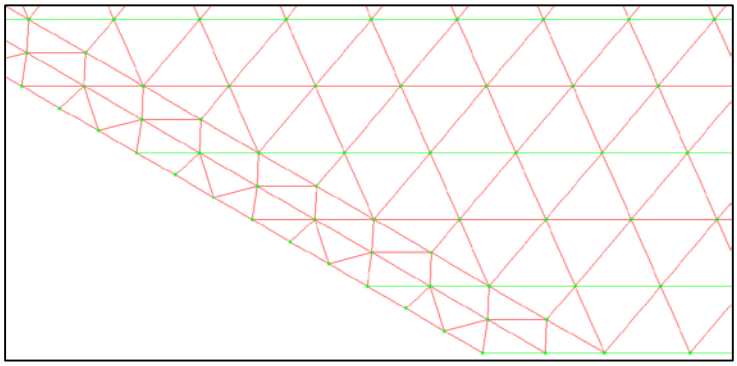

Figure 8. Triangular mesh for 60° skew models.

4.1.7 Soil

4.1.7.1 Pile Soil

A series of nonlinear springs represent soil resistance along each pile. Each spring has two orthogonal components aligned with the bridge direction instead of the skewed abutment direction because the main thermal movement is in the bridge longitudinal direction regardless of skew. Springs were distributed every 6 in. for the top 5 ft, every 1 ft for the next 5 ft, every 2 ft for the next 10 ft, and every 5 ft for the last 20 ft. The lateral load-displacement (P-y) curves were generated in LPILE. Based on the additional overburden stress from the abutment backfill, soil spring stiffness was calculated separately for expansion and contraction directions.

4.1.7.2 Abutment Backfill

Abutment backfill was modeled as a single spring throughout the abutment height at the pressure-resultant location. This method was chosen as a simplification, and its accuracy was validated with an investigation on distributed versus concentrated links. Like the pile soil springs, the backfill springs have two orthogonal components, but they are aligned to the abutment axis. One of the components is normal to the abutment surface, representing soil pressure, and the other represents soil friction parallel to the abutment surface. This friction force was calculated based on a constant normal force from base non-skew bridge models. Although the normal force may be larger for skewed cases, this approach is conservative for the estimation of bridge demands.

4.1.7.2.1 Backfill Spring Capacity

To simplify calculation, the at-rest soil pressure before thermal loading is applied and the active pressure during thermal contraction are both considered to be zero (personal communication, Professor James Long, University of Illinois at Urbana-Champaign). From Table 10-1 of the Navy Soil Mechanics, Foundations, and Earth Structures Design Manual (Department of the Navy 1971), the angle of skin friction δ between the abutment front face and backfill was assumed to be 15°. The internal friction angle Ø of the uncompacted backfill was assumed to be 30°. According to Figure 10-3

of the Design Manual, when Ø is 30° and the slope angle is zero, the passive pressure coefficient K_p is 6.5 for $-\delta / \emptyset = -1$. When $-\delta / \emptyset = -0.5$, Ø = 30°, the reduction factor for K_p is 0.746. Therefore,

$$K_p = 0.746 \times 6.5 = 4.849$$

The horizontal component of passive pressure coefficient during thermal expansion would be

$$K_H = K_p \text{ Cos } \delta = 4.849 \times \text{Cos } 15° = 4.6873$$

The abutment backfill links are all modeled at the resultant location of the passive pressure. Therefore, the limiting resultant force normal to abutment face is

$$N = K_H \gamma H \bullet \tfrac{1}{2} H = \tfrac{1}{2} K_H \gamma H^2$$

The limiting friction resultant force is

$$F = N \mu = N \tan \delta$$

It was also assumed that the backfill would reach limiting passive pressure after 1 in. displacement (Olson et al. 2012 and personal communication, Professor James Long, University of Illinois at Urbana-Champaign).

4.1.7.2.2 Discretization of Backfill Model

Although backfill pressure acts against the entire abutment in a distributed manner, abutment backfill pressure can be modeled with a single spring at the pressure-resultant location. Comparison tests were performed on three 400 ft long bridge models with one, two, and eight horizontal layers of abutment backfill links, respectively. No significant differences were found in girder forces, pile forces, or bridge deformation. Therefore, it was decided to use one layer of abutment links at the resultant elevation in the parametric models.

The current methodology used to model backfill is a lumped elastic-perfectly plastic (EPP) spring at the centroid of the abutment. This method neglects the effects of differential yielding in the soil. Due to abutment rotations, it should be expected that the soil near the top of the abutment will experience slightly higher displacements than the soil at the backfill centroid. The displacement at the backfill centroid controls the yielding and it hasn't yet reached yielding when the soil at the top of the abutment begins to yield. This is a modeling simplification that is not apparently justified.

To investigate this further, an extreme rotation of the abutment was obtained from the SAP2000 results. This value was chosen to be θ = 0.007 radians. This value of rotation was then used to determine the correct backfill "force vs. displacement" relationship, which can be seen in Figure 9. The EPP model appears to be a reasonable assumption. Additionally, this is a transient phase in the evolution of the model. The final force and displacements will be correct.

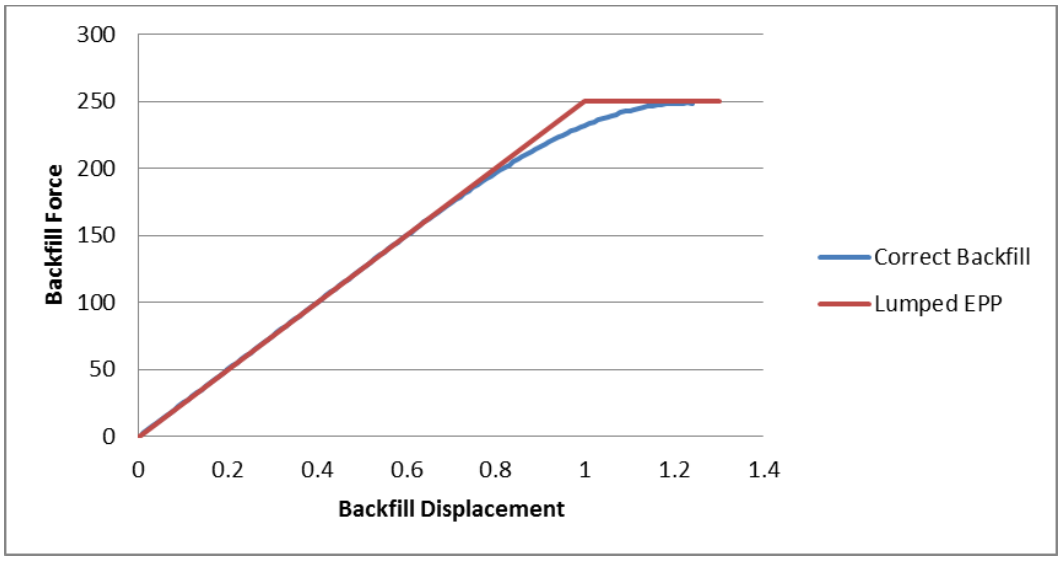

Figure 9. Correct vs. assumed backfill force displacement relationships.

The backfill stiffness centroid is also an additional matter that will introduce small errors. The backfill spring was placed at two-thirds of the abutment depth. This implies that the centroid of the backfill stiffness will be at this location throughout the model evolution. However, the stiffness will rarely be at this location. The correct location will be slightly higher during the linear range because the displacement is higher at the top of the abutment during this stage due to rotations. As the soil at the top of the abutment yields, the stiffness centroid will shift downward.

In the fully plastic range, the stiffness of the abutment backfill is 0, so its location is irrelevant. The only matter of concern in the plastic range is that force that is being applied and what its value is. Both the force and its location will be correct assuming the constitutive model of the soil is correct at any given depth (i.e., as depth increases, the ultimate soil force increases linearly).

4.1.8 Parapets

The design parapet weight was determined to be 0.45 k/ft (research team communication, IDOT). This weight was added to bridge edges using frame elements with concrete material assigned. Parapets were designed with a cross-section of 38 in. × 12 in. with all property modifiers set to zero except weight and mass.

4.2 MODELING SIMPLIFICATIONS

To simplify bridge modeling, the importance of modeling wingwalls, approach slab, girder camber, and cross frames was investigated.

Even though 3D solid elements are more accurate in representing structural components, due to the large number of bridge models being analyzed and the corresponding processing effort required, the simpler element types formerly used by the Illinois researchers were largely maintained for this study, with support from new trial analyses and comparison tests.

4.2.1 Wingwalls

Based on the previous research (Olson et al. 2012) and a research project done in Minnesota (Huang et al. 2004), it was concluded that wingwalls, regardless of the different orientations, should have only a minor effect on IAB behavior. Therefore, wingwalls are excluded from the parametric models and are excluded from the sensitivity analysis.

4.2.2 Approach Slabs

Approach slabs were suspected to be exerting some level of axial force into the superstructure. To see its general effect, a 400 ft bridge model was made in SAP2000 with approach slabs connected to both abutments. Following the current IDOT policy, the approach slab–abutment connection could transfer only vertical shear and axial force because the bar splicer was removed. The 30 ft long approach slab was modeled with shell elements using actual concrete properties and slab thickness. It was supported by many discrete horizontal links representing the soil friction forces that could be generated from the tributary slab weight. Vertical links represented the normal force generated by the concrete–soil interface. Under positive thermal loading, the forces in the superstructure due to approach slab friction were negligible. The bridge behavior was not affected by the presence of the approach slab, and the research team consequently decided to exclude approach slabs from the parametric models.

4.2.3 Girder Camber

Due to the P-Δ effect, camber might cause a change in superstructure forces under thermal loading. SAP2000 has an option to modify the undeformed geometry such that the shape can be changed according to the results of one load case, so that after the loading is applied, the deformed structural shape can be the same as the original shape when the structure is first defined. Camber can be created using this option by modifying the undeformed geometry after staged construction case is run, thus girder and deck will “bow up.”

Comparisons were made between models with and without modified undeformed geometry with the P-Δ option turned on during analysis. The two bridge designs selected were 4 × 100 ft spans, 30° skew, 36 ft width; and 2 × 200 ft spans, 30° skew, 36 ft width. It was found that girder forces, pile forces, superstructure, and abutment–pile displacements were all very close. Therefore, camber can safely be ignored for bridges with 100 ft to 200 ft spans.

As a verification, another test was done in which the girders were assigned a low stiffness value, thus creating very large deflections under dead load and, accordingly, a large amount of camber when the undeformed geometry was modified. A significant change in girder forces was observed. Therefore, a large amount of camber can play an important role, but the parametric models with realistic designs most likely will have small deflection under dead load and thus little camber will be required. Based on the assumption that the parametric study bridges would likely be configurations requiring a small amount of camber, as well as the validation models discussed above, camber was ignored in the modeling process.

4.2.4 Cross Frames

Two bridges were modeled—one with angle cross frames and one with horizontal channel diaphragms. It was found that even though axial force developed in cross-frame members, the bridge behavior remained largely unaffected except that swings along the girder length were observed for girder minor moment, which is minimal compared with major moment. Under negative thermal plus full live loading, the 600 ft long bridge with 96 ft width and 45° skew showed larger differences in edge girder moments in the span where truck load was applied. Because thermal loading is the focus of the project, the conclusion was drawn that cross frames could be eliminated in the parametric models.

4.3 LOAD CASES AND SEQUENCES

Because the main goal of the project was to investigate bridge behavior under service conditions, all applied loadings were unfactored. Table 6 lists all load cases analyzed in the study. The staged dead load case used nonlinear staged construction analysis, while the thermal and live load cases used nonlinear static analysis.

Table 6. Load Cases Used in the Parametric Study

Method	Actual Loading	Shorthand
Analyzed in SAP2000	Dead: Staged Construction	Dead Staged
	Dead + HL-93 Live	HL-93
	Dead + Positive Thermal	Positive Thermal
	Dead + Negative Thermal	Negative Thermal
	Dead + Positive Thermal + HL-93 Live	HL-93 Positive Thermal
	Dead + Negative Thermal + HL-93 Live	HL-93 Negative Thermal
Computed from results	Dead + Positive Thermal—Dead Staged	Pure Positive Thermal
	Dead + Negative Thermal—Dead Staged	Pure Negative Thermal

4.3.1 Dead Load—Staged Construction Case

To represent the behavior under dead load and to obtain the deformed bridge shape and stiffness at the end of dead loading, staged construction analysis was used for the dead load case. Table 7 lists the sequence of stages modeled in SAP2000.

Table 7. Explanation for Each Step of Staged Construction Analysis

Stage No.	Action	Result	Reason
1	Add structure	Add the entire structure	—
	Remove structure	Remove parapets	Parapets should be loaded only after deck is cured
	Change modifiers	Make girders heavy to include deck weight	Let deck have zero stiffness to simulate soft deck before curing. Deck must also be weightless, and the weight is taken by girders; otherwise, the soft deck will have large deflections between girders due to self-weight
	Change modifiers	Make deck soft and weightless	
	Load objects if added	Load everything except parapets	—
2	Change modifiers	Let girders have original self-weight	—
	Change releases	Fix girder ends	To simulate the abutment hardening and restraints placed on girder ends
	Change modifiers	Let deck have supposed stiffness and weight	Deck weight is already applied through modified girder weight. After deck hardens, deck elements can be used to apply the weight of future wearing surface
3	Add structure	Add parapets	—
	Load objects	Load parapets	—
	Load objects	Load deck	Future wearing surface weight is actually applied. The scale factor is 0.5, which is the weight ratio of future wearing surface to deck

4.3.2 Thermal Load Case

Based on the previous Illinois research (Olson et al. 2012) and IDOT correspondence, the thermal range was maintained as –80°F to +80 °F. The coefficients of thermal expansion used for concrete and steel are 5.5×10^{-6} / °F and 6.5×10^{-6} /°F, respectively. All bridge components except for the piles were subjected to this thermal loading, but only 60% of the temperature change was applied on the pier footing to avoid excessive thermal deformation that could cause issues with the pier–superstructure connection. For typical locations in Illinois, the AASHTO (2012) total uniform temperature *range* for "Procedure B" is only 125°F or less. Therefore, bridges with a base construction temperature between 40°F and 75°F would allow for the full range of –80°F to +80°F temperature change.

Thermal loading was uniformly applied to girder frame and deck shell elements, which was found by Paul et al. (2005) to produce similar results when compared with those including imposed temperature gradients through the depth of the bridge superstructure. Neither temperature gradient nor other secondary superimposed deformation effects (e.g., differential shrinkage, creep, or settlement) were typically included in the analyses. This finding is generally in line with AASHTO (2012) as far as these effects not necessarily needing to be investigated for all types of bridges. Additionally, IDOT does not typically consider temperature gradient in routine analysis and design of IABs.

4.3.3 Live Load Case

An HL-93 truck load was used as the live load case for this study. It was applied as a uniform load on the entire bridge to represent the design lane load, in addition to another equivalent uniform load placed at the center of one end span to represent the design truck. These equivalent loads were placed across the entire bridge width for the length of a standard truck. Bridges that were modeled to be wider than the standard two-lane bridges of the primary study also had the equivalent truck load placed as a uniform load across the entire bridge width. This equivalent uniform truck load placement was used because it allowed for automation of the bridge modeling procedures while having only a negligible effect on global bridge behavior compared with the standard point truck loads. The multiple presence factor was kept at unity throughout the analyses—the base set of bridges had only two lanes, and the subset of additional bridges with greater widths had the equivalent truck loading placed as a uniform load across the entire bridge width.

4.4 MODELING AND ANALYSIS AUTOMATION PROCESS

To streamline the process of creating and analyzing such a large number of models, automation processes were created. Using Visual Basic for Applications (VBA), an Excel spreadsheet was created that would generate the SAP2000 models for the given bridge geometries entered by the user. Similarly, a post-processor spreadsheet was created that would collect resulting nodal and element data from the analyzed models, and call upon MATLAB to perform any necessary calculations.

CHAPTER 5: RESULTS FOR STANDARD NON-SKEW AND SKEW CASES (PRIMARY PARAMETERS)

5.1 FUNDAMENTAL IAB BEHAVIOR

Because IAB construction provides a frame-like structure at the abutment location, thermal changes result in a distribution of forces to the abutment and substructure (pile foundation). Both thermal expansion and thermal contraction of the superstructure are partially restrained; this induces forces into the superstructure. A schematic free-body diagram of the abutment reveals how the internal forces (axial force and bending moment) in the superstructure are distributed to the substructure. The two main sources of thermal resistance are the backfill passive pressure (engages only in thermal expansion) and the soil resistance applied to the pile foundation. Figure 10 shows free-body diagrams for the abutment under thermal expansion and thermal contraction.

The soil resistance to thermal expansion is larger because the backfill provides additional overburden. Therefore, soil resistance at the foundation is larger during thermal expansion than during thermal contraction. While the backfill acts to relieve demands placed on the pile under thermal expansion of the superstructure, the soil is stiffer at the foundation and may attract higher forces (when compared with the abutment response to thermal contraction). These competing effects are influenced by backfill soil properties, foundation soil properties, abutment depth, and pile stiffness. The combination of each of these variables will determine whether the thermal expansion or contraction load case governs thermal structural demands (i.e., pile bending moments, girder axial force, and bending moments).

For most of the cases analyzed in this parametric study (using the default soil parameters), thermal expansion of the superstructure governed demands versus thermal contraction. Thermal contraction governed only in select bridge cases with all 50 ft spans, and several of the cases presented with alternate soil properties and pile configurations. For secondary parameter bridges with stiffer soils (both foundation and backfill), alternate pile shape or orientation, double piles, or pile top relief, and which reached beyond a threshold EEL, the governing case switched from thermal expansion to thermal contraction. It should be noted that service load demands at the critical pile and within the superstructure are still governed by the HL93-EXP load case (dead + live + positive thermal). This is because thermal contraction acts to relieve stress due to gravity loads and thermal expansion acts to increase stress due to gravity loads. For example, applying gravity loads to the bridge end span causes a clockwise rotation of the abutment shown in Figure 10—this adds to expansion demands and relieves contraction demands.

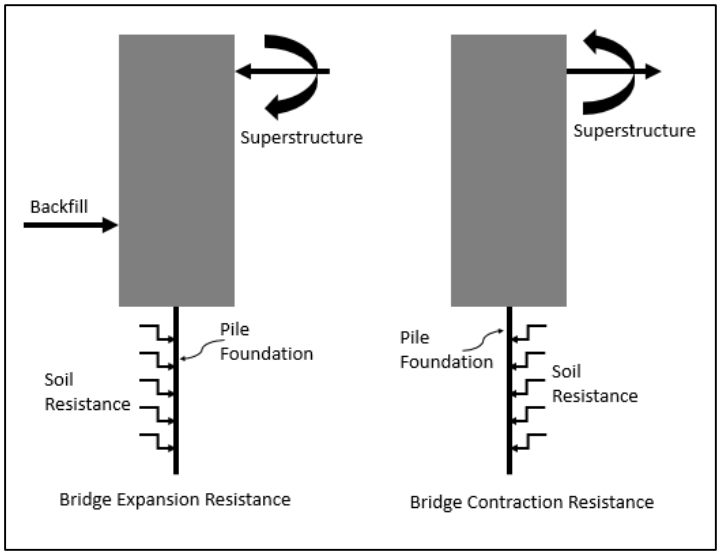

Figure 10. Free body diagram of abutment.

5.2 GLOBAL MOVEMENTS

Expected movement at the deck level due to thermal expansion and contraction is a very important factor in the analysis and design of IABs. Regardless of boundary conditions, volumetric changes in the structure itself need to be accommodated, which is done through various forms of expansion joints at the end of each approach slab. IDOT, for example, uses a strip seal that can accommodate approximately 2 in. of movement in either direction. Other options for accommodating more movement include finger plate joints, modular joints, and bituminous asphalt seals (Iowa DOT 2012; Chang and Lee 2001).

A plan view of an IAB deck is shown in Figure 11, with U1 and U2 indicating the direction of longitudinal and transverse movement, respectively. Average longitudinal movement at the deck level along the abutment of the non-skew parametric study model bridges can be seen in Figure 12. This corresponds directly to the movement that would be seen by a strip seal or other expansion detail. As expected, the movement is almost exclusively dependent on the thermal component of loading. Therefore, the movement is mainly only a function of effective expansion length (EEL) and temperature change, which was held at ±80°F for this study. The small variations at each EEL resulting from the slight longitudinal movement caused by the rotation from gravity loads were considered negligible, allowing for longitudinal movement to be predicted by a simple linear regression. Resulting model displacements are approximately 90% of free expansion/contraction as determined by a weighted average of concrete and steel coefficients of thermal expansion. Because there is no backfill resistance in the case of contraction, the displacements are slightly greater than those from expansion.

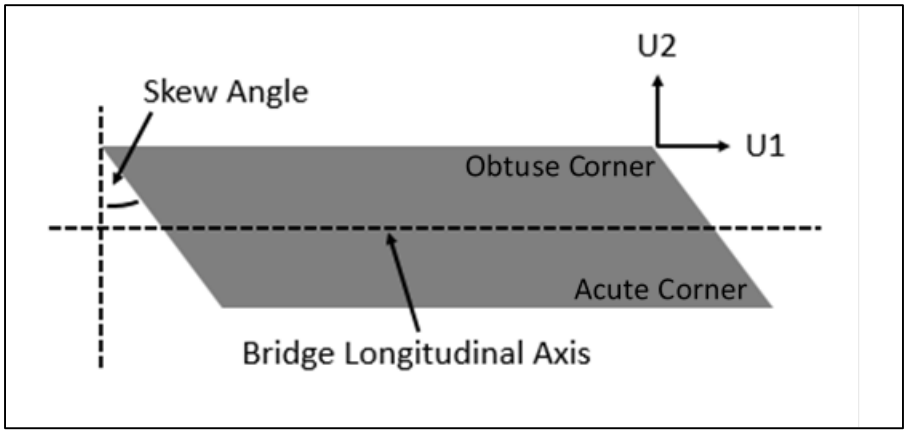

Figure 11. Plan view of IAB deck.

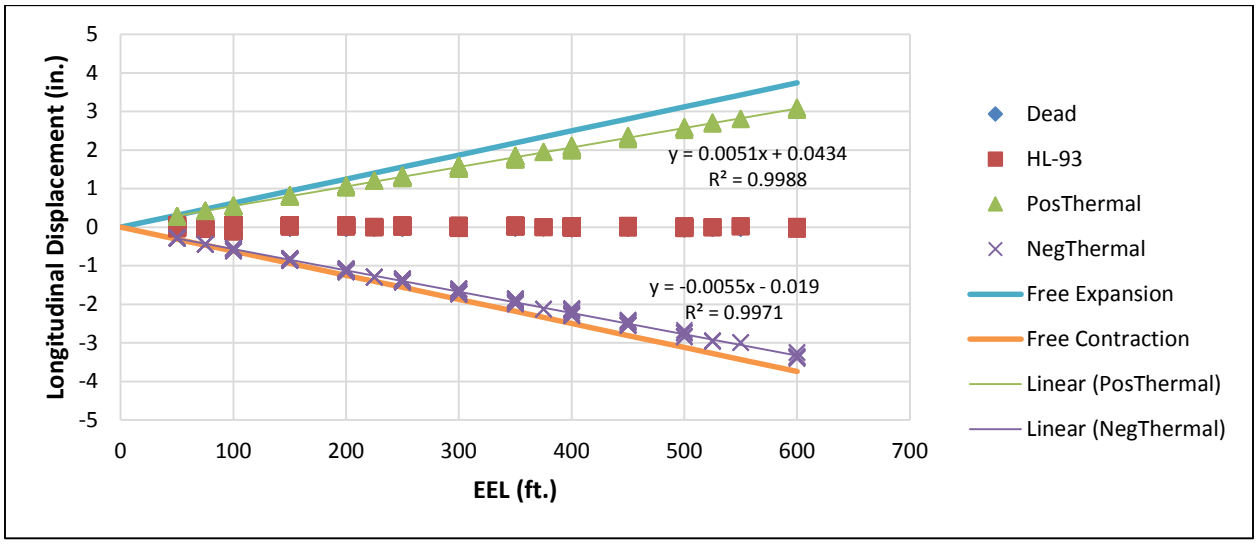

Figure 12. Average longitudinal bridge movement vs. EEL for non-skew bridges.

When skew is introduced, there is not a drastic change in average longitudinal bridge movement. As seen in Figure 13, the linear trend lines for expansion and contraction of the 45° skew models are nearly identical to those generated from the non-skew bridges. The longitudinal displacement at the acute and obtuse corners differs slightly, though the difference between the two is negligible. However, transverse displacements are significantly influenced by skew.

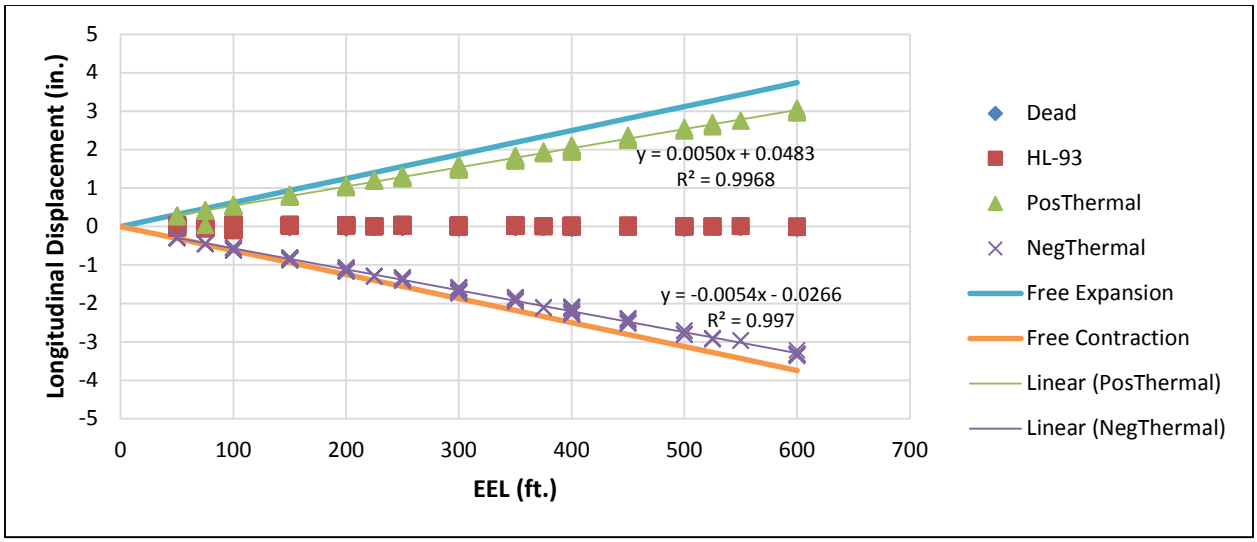

Figure 13. Average longitudinal bridge movement vs. EEL for 45° skew bridges.

Figures 15 and 16 display the longitudinal and transverse displacements due to the positive thermal load case of a four-span continuous IAB with 100 ft spans and HP14×73 piles with skew varying from 0° to 60°. Response due to thermal contraction is not shown here, but it is analogous to the expansion case. Though the acute corner displacements increase with skew while those of the obtuse corner decrease, each location still indicates positive thermal displacements. The transverse displacements shown in Figure 15 indicate rigid-body displacement of the abutment in the horizontal plane. This is shown by the linear trend of displacements at various points along the abutment. Transverse displacements for a non-skew bridge are equal in magnitude for both corners, but increased bridge skew results in non-symmetric movement of the acute and obtuse corners. In comparison to the non-skew case, transverse movement of bridges with skew between 0° and 30° tends more toward the obtuse corner. However, with skews above 30°, this movement is toward the acute corner. In both cases, there is a slight amount of overall abutment movement in the transverse direction.

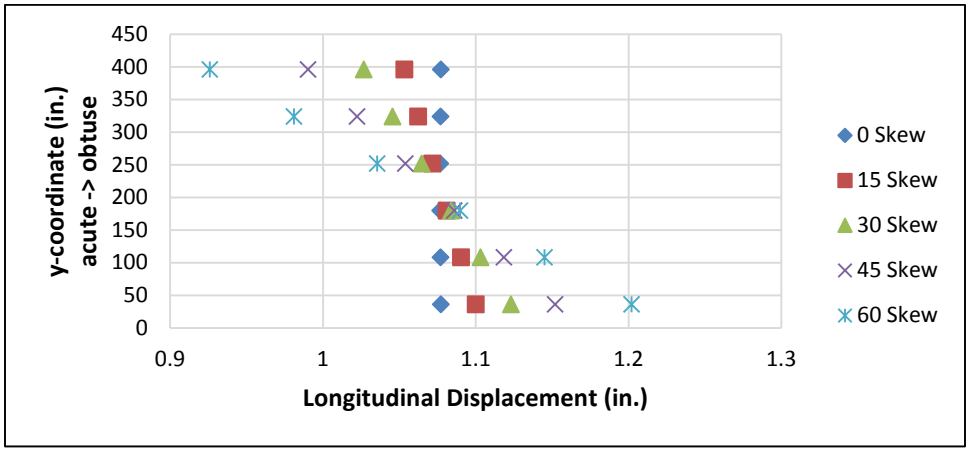

Figure 14. Longitudinal displacements from positive thermal load case for a four-span bridge with 100 ft spans (HP14×73 piles).

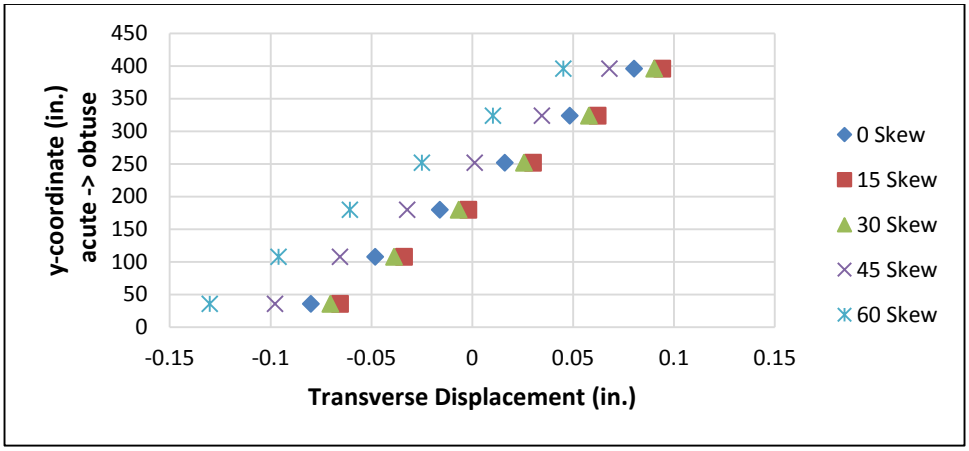

Figure 15. Transverse displacements from positive thermal load case for a four-span bridge with 100 ft spans (HP14×73 piles).

5.3 PILE STRAINS

As previously stated, when bridge skew is increased, the longitudinal and transverse displacements of the acute and obtuse bridge corners are altered. This, in turn, affects the frictional and normal forces acting on the pile head, thus altering pile behavior. Figures 17 through 22 depict schematics of typical pile behavior for bridges with 100 ft spans and HP14x73 piles under both positive and negative thermal loadings with various skew scenarios. The direction of bridge movement is dependent upon pile size and span length, so the schematic skew thresholds do not necessarily hold true for all cases. However, various directions of bridge corner movement observed in the parametric study models are covered by the figures, and the pile behavior corresponding to each scenario can be clearly observed. As stated in the previous section, global movements for skewed bridges are complex. The direction of movement of the acute and obtuse corners of the bridge directly correlates to the pile behavior. In all cases, the rotational restraint of the abutment causes double curvature of the pile head. Based on the direction each corner moves under positive or negative thermal loads, the combatting frictional force can either relieve the double curvature (reducing pile strains) or exacerbate the double curvature (increasing pile strains).

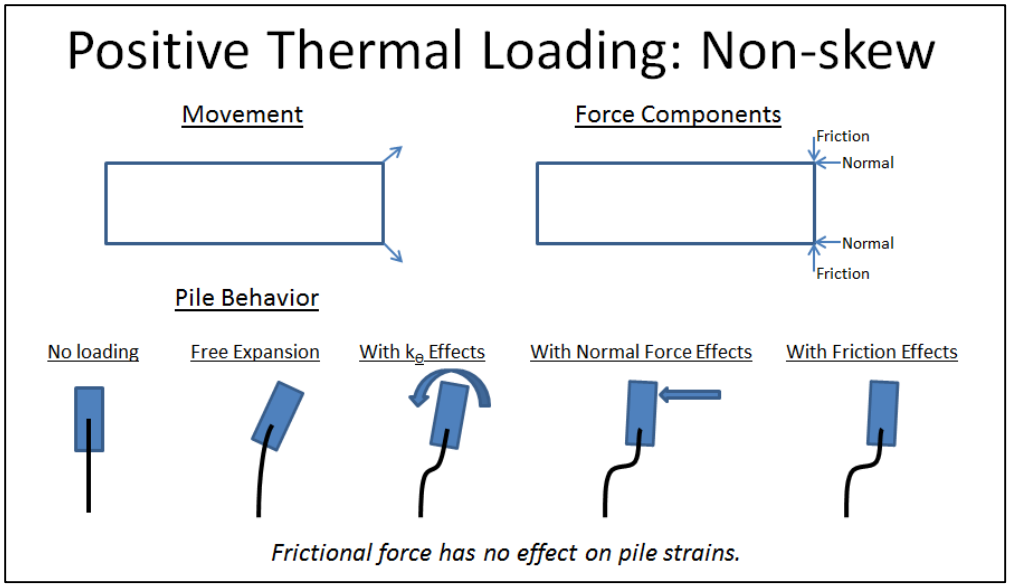

Figure 16. Schematic of pile behavior under positive thermal loading for non-skew bridges.

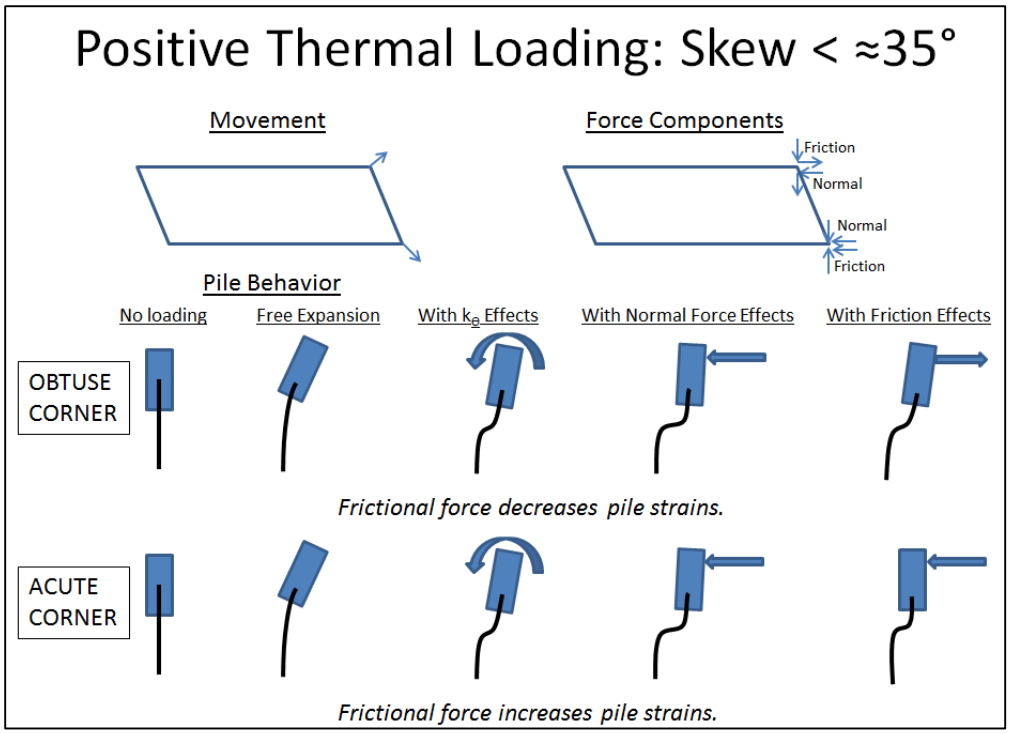

Figure 17. Schematic of pile behavior under positive thermal loading for bridges with skew < ≈35°.

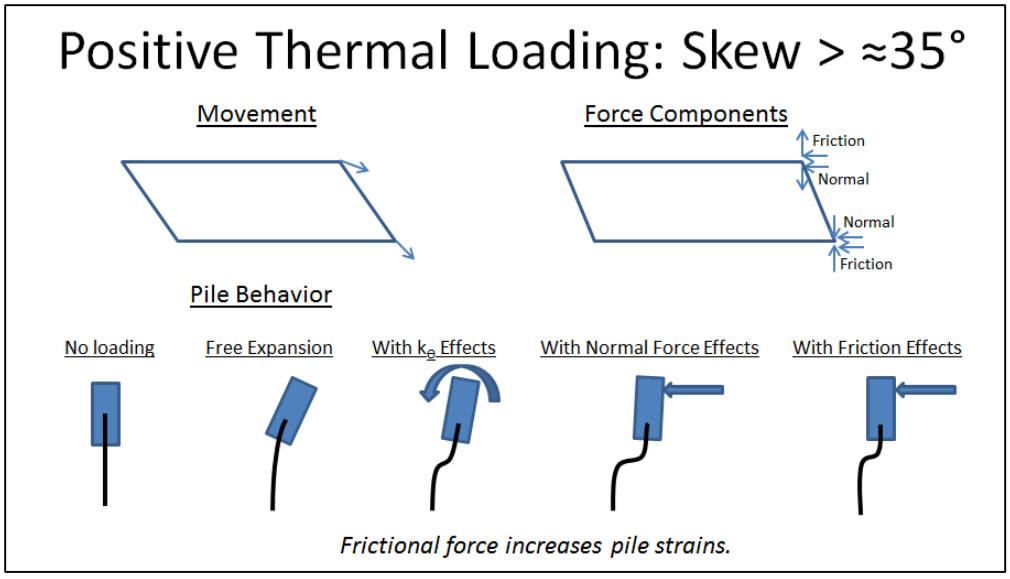

Figure 18. Schematic of pile behavior under positive thermal loading for bridges with skew > ≈35°.

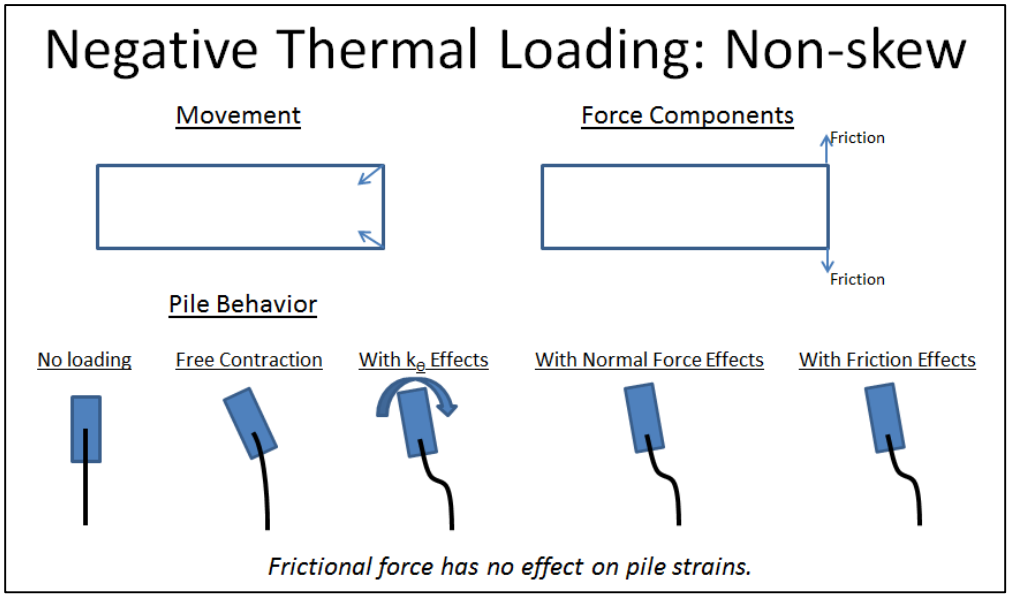

Figure 19. Schematic of pile behavior under negative thermal loading for non-skew bridges.

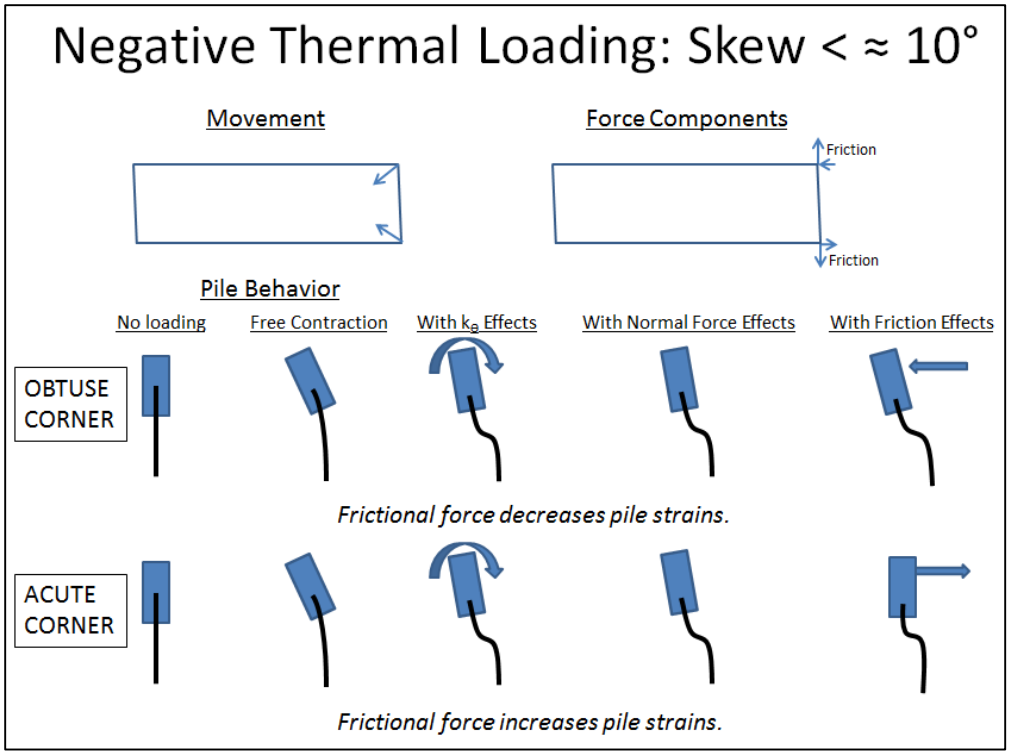

Figure 20. Schematic of pile behavior under negative thermal loading for bridges with skew < ≈10°.

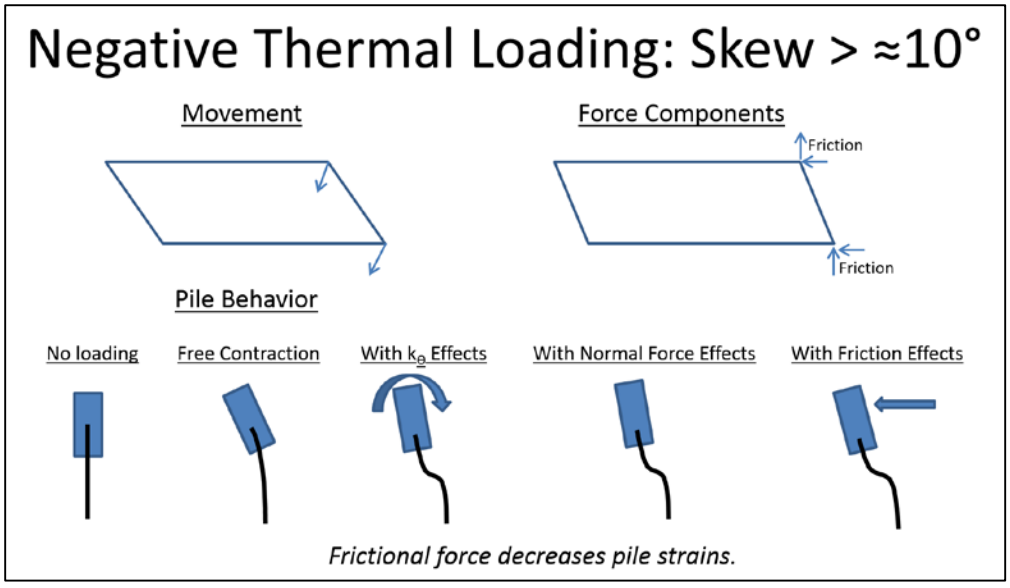

Figure 21. Schematic of pile behavior under negative thermal loading for bridges with skew > ≈10°.

Due to increased longitudinal displacements at the acute corner with increased skew, the acute pile is the location of the critical pile head. This is made evident in Figure 22, which depicts the pile deflection along the longitudinal axis of the bridge (weak-axis bending of the H-pile) for a 45° bridge

case subjected to positive thermal loading. These larger displacements produce larger lateral displacement of the pile head, which increases pile bending demands.

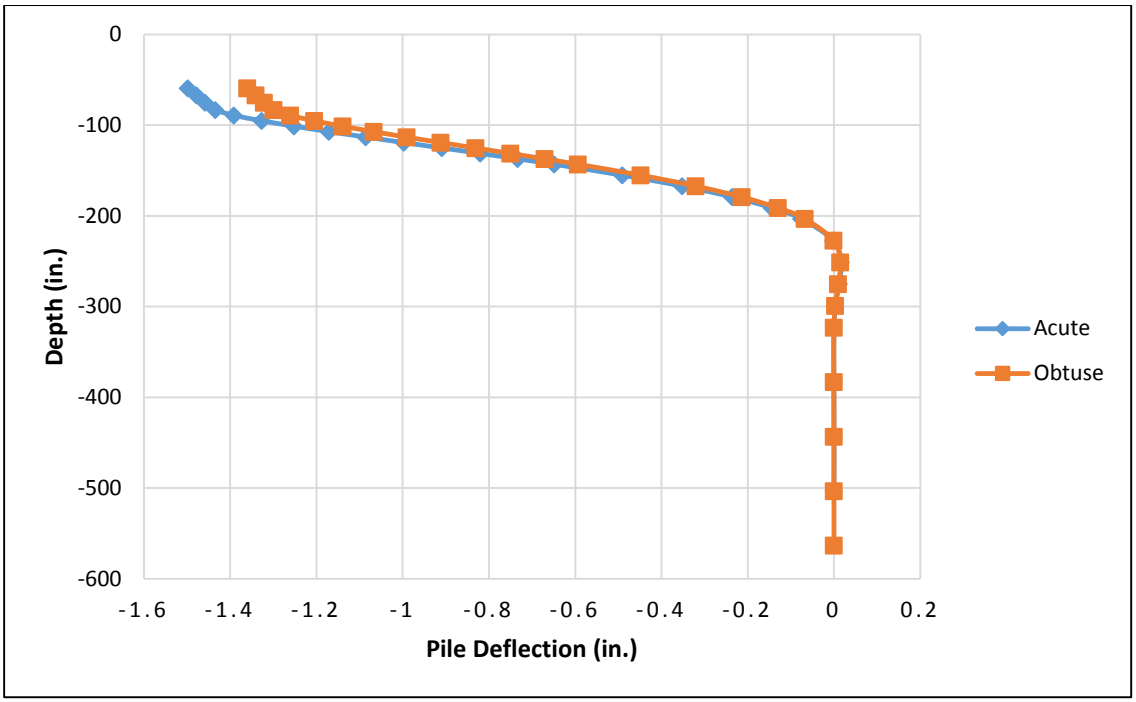

Figure 22. Acute and obtuse pile deflections due to positive thermal loading for a six-span, 45° skew bridge with 100 ft spans and HP14×73 piles.

As abutment skew is increased, the deflection of the acute pile in the longitudinal bridge direction due to positive thermal loads is also increased. However, as can be seen in Figure 23, once a certain depth is reached, the pile essentially becomes fixed, with negligible deflection for any skew. This directly correlates to the trends of the weak-axis bending moment of the pile, depicted in Figure 24. The figure plots the weak-axis pile moments for an extreme bridge case, with an EEL of 300 ft. It can be seen that the greatest magnitude moments do occur at the pile head, transitioning from the negative moment region to the positive moment region until moments eventually remain 0 below the fixity location observed in the deflection plot.

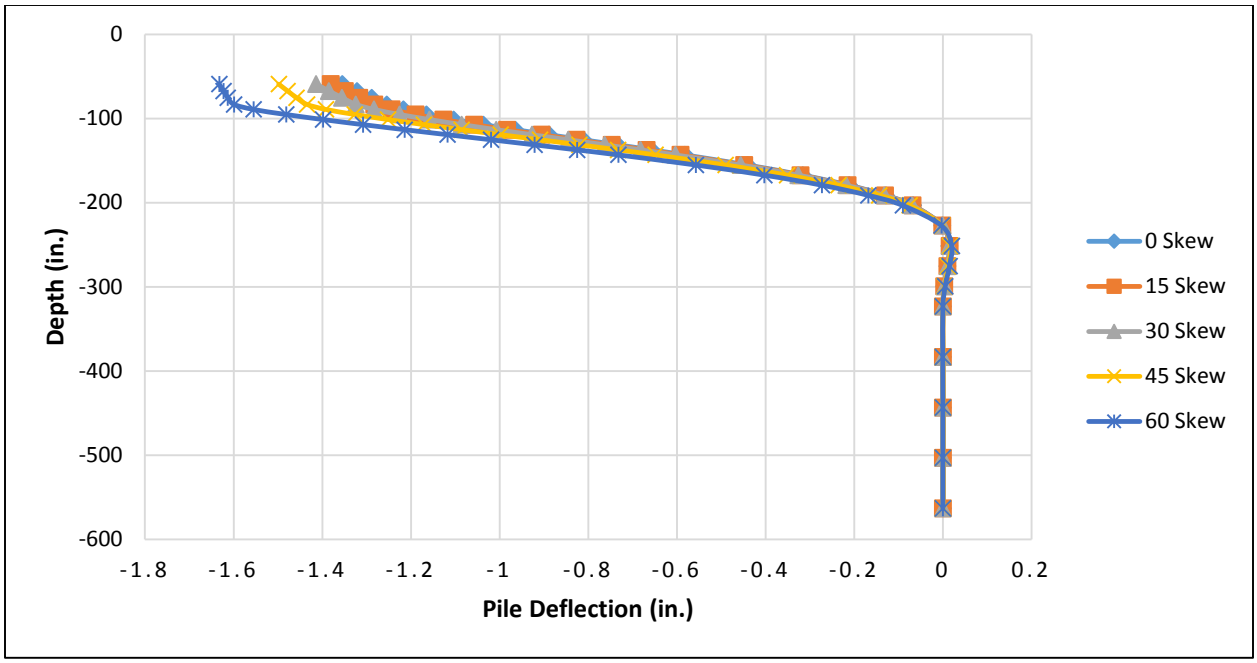

Figure 23. Acute pile deflections due to positive thermal loading for six-span bridges with 100 ft spans and HP14×73 piles.

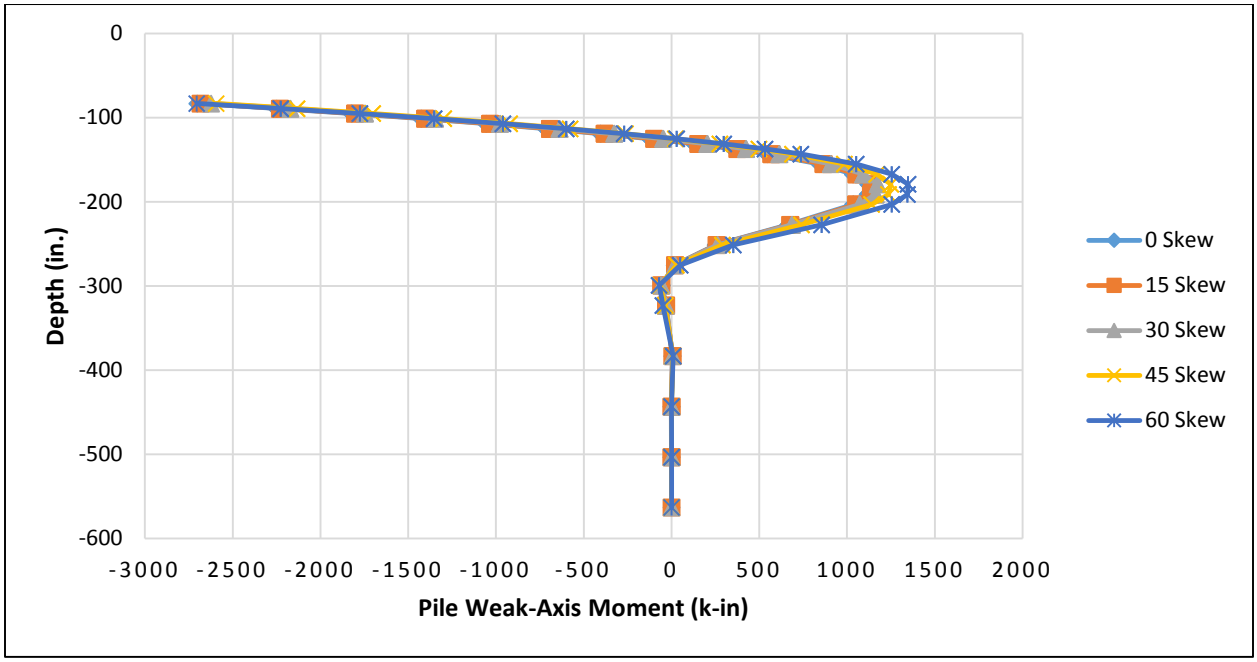

Figure 24. Acute pile moments due to positive thermal loading for six-span bridges with 100 ft spans and HP14×73 piles.

Peak pile strain for each pile along the abutment of a four-span IAB with 100 ft spans and HP14×73 piles under pure positive thermal loading is shown in Figure 25. As skew is increased from 0° to 60°, the acute pile strain from a temperature change of +80°F alone increases from 0.00195 to 0.00550. This trend is not only at the acute corner, but peak pile strains across the entire abutment increase as a result of increased skew.

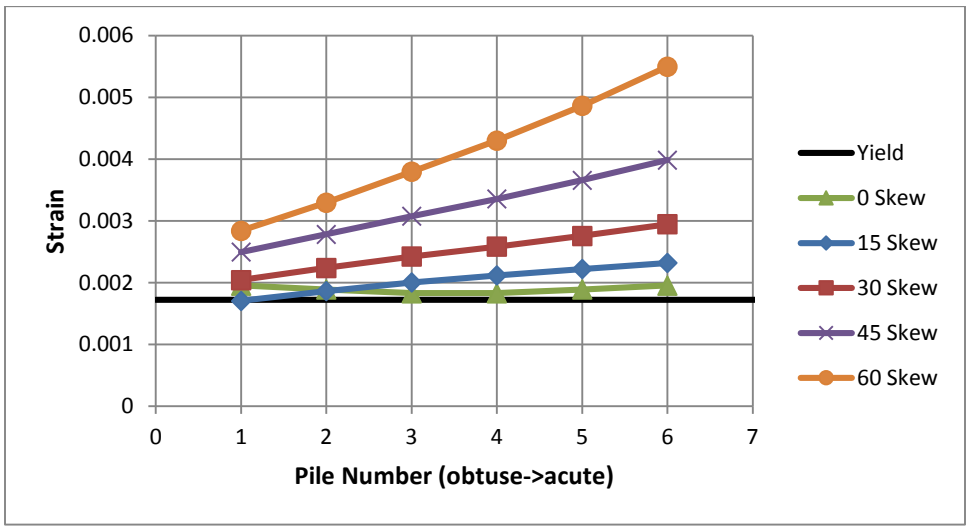

Figure 25. Peak pile strain under pure positive thermal loading for a four-span bridge with 100 ft spans and HP14×73 piles.

One of the most obvious relationships related to pile strain is with the EEL of the bridge. With an increased EEL, the change in bridge length due to thermal changes also increases, which causes the pile rotations and displacements to increase as well. These increased deformations clearly lead to an increase in pile strain. However, the exact relationship between maximum pile strain and EEL will vary based on properties of the superstructure, the substructure, and the soil–structure interaction. Figure 26 shows peak pile strains (at the acute corner) under pure positive thermal loading for IABs with 100 ft spans and HP14×73 piles. As noted above, an increase in skew results in increased peak pile strains. The effect of skew also works to amplify the effect of increased EEL. This is because the amplification of transverse bridge deformation is more pronounced for bridges with large EEL and skew.

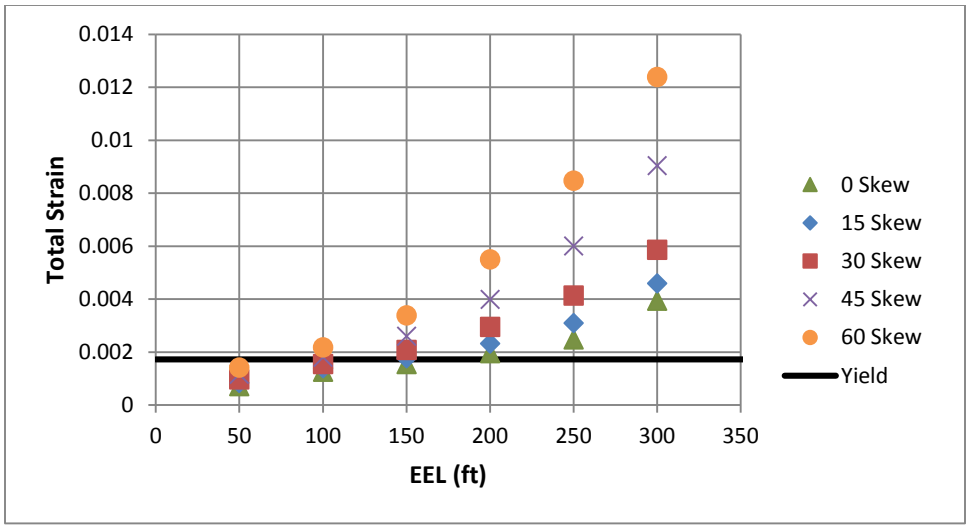

Figure 26. Total pile strains under pure positive thermal loading for bridges with 100 ft spans and HP14×73 piles.

Other crucial parameters affecting pile strain are superstructure rotational stiffness (k_θ) and pile size. For the plots of non-skew bridge pile strains shown in Figures 28 and 29, the value of k_θ is approximately held constant, while the section properties of the pile are varied. When comparing the total strain for a given pile size in Figure 27 with that of the same pile size and EEL in Figure 28, it can be seen that critical pile strains increase with increased k_θ (200 ft span bridges have a larger k_θ than 100 ft spans). This is largely due to the fact that as abutment rotation approaches zero, the pile approaches the behavior of a fully fixed head condition; whereas, as the abutment is allowed to rotate freely, the pile approaches the behavior of a free head condition. Additionally, pile strains decrease with increased pile size. By observing the trend with which the maximum pile strain changes with change in pile size, it is clear that some combination of pile area and weak-axis moment of inertia plays a role in determining pile behavior for a given k_θ. It should be noted that with increased skew, the strong-axis moment of inertia will play an increasingly important role in pile behavior.

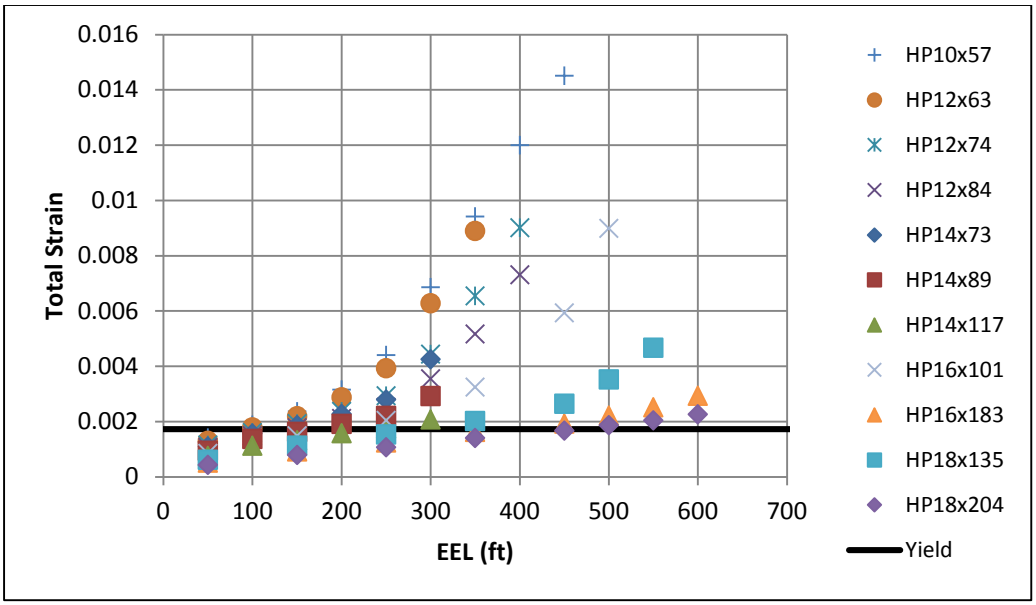

Figure 27. Total pile strain under positive thermal loading for non-skew bridges with 100 ft spans.

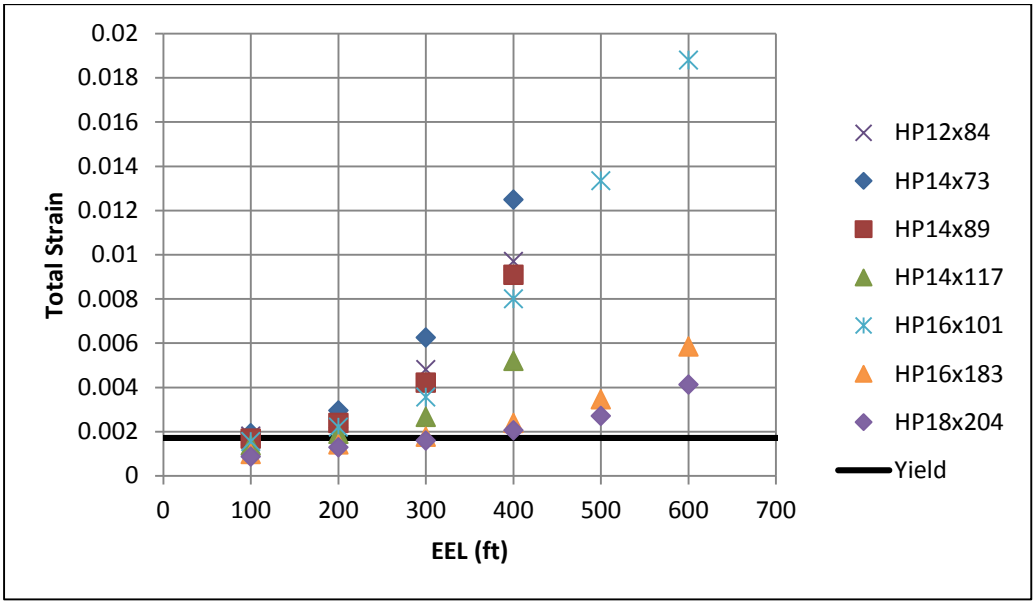

Figure 28. Total pile strain under positive thermal loading for non-skew bridges with 200 ft spans.

5.4 GIRDER STRESSES

Thermal loads applied to a conventional steel girder bridge with composite concrete deck will produce a small amount of flexure due to the unequal coefficients of thermal expansion for concrete and steel, but these stresses are small enough—reaching a maximum on the order of 3 ksi—to be neglected when proportioning girders. In IABs, the restraint that the abutments provide to the girders causes additional stresses to develop within the girder cross section under thermal loads (Fennema et al. 2005), and these stresses are significant enough to warrant consideration when proportioning

girders (Kim and Laman 2010). EEL heavily influences girder stresses because it directly affects longitudinal global movements. These global movements impose forces on the girders depending on other variables such as pile stiffness, soil stiffness, and the rotational restraint imposed on the abutment by the superstructure.

Girder stress results presented herein are taken from the extreme fiber of the bottom flange at mid-width. That is, only strong axis bending and axial force contribute to the stress value. Weak axis bending acts to increase the total stress at one of the bottom flange tips, and decrease the total stress at the other. In general, as will be discussed below, the increase in the reported stress value due to weak axis bending increases along with skew. However, this increase is significant only near supports. As the distance from a support gets greater, weak axis flexure becomes more and more negligible. For select extreme cases, the stress at the abutment of the flange tip due to thermal loading including weak axis flexure can be double what is seen from just strong axis flexure and axial force alone.

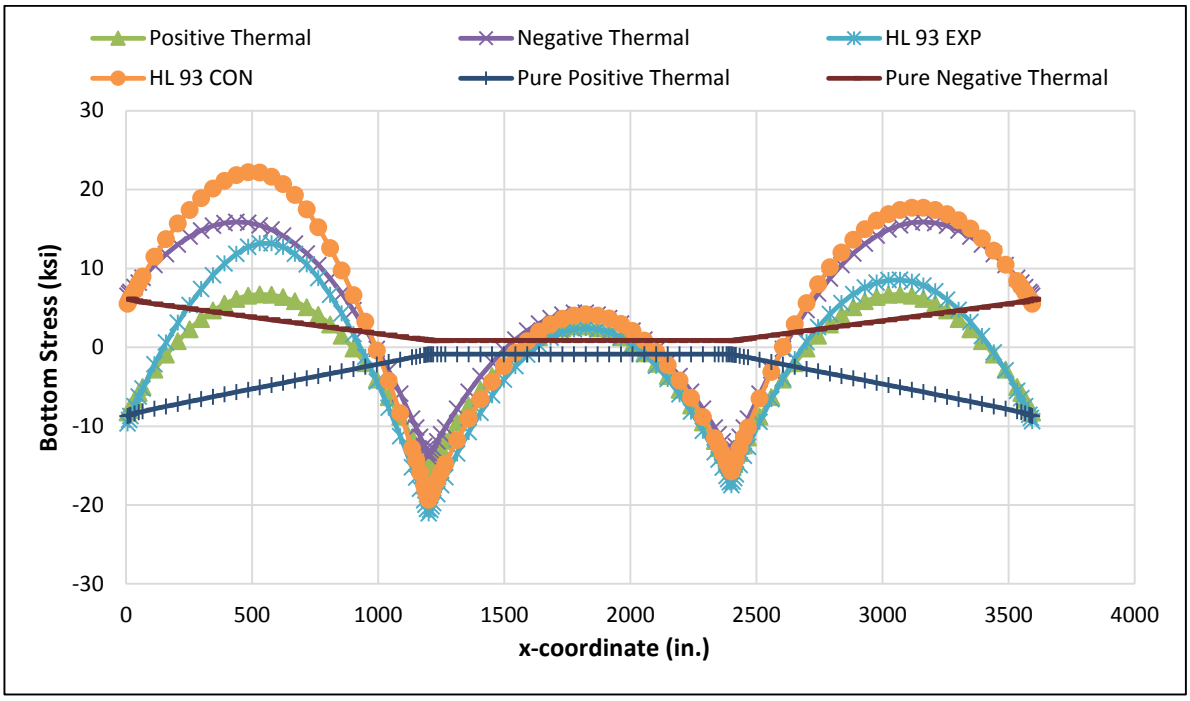

Figure 29. Girder bottom flange stresses for a three-span non-skew bridge with 100 ft spans and HP14×73 piles.

Figure 29 plots the stress at the center of the extreme fiber of the bottom flange of a steel girder for a three-span IAB with HP14×73 piles. Girder stresses for each load case analyzed are plotted along the longitudinal axis of the bridge. For the cases that include live load, the HL-93 live load was applied at the left end span of the bridge, which results in higher stresses in that span. Also included in the plot are girder stresses for the pure positive thermal and pure negative thermal load cases, as defined above. Stresses due only to thermal loads are maximum at the abutment due to the girder bending imposed by its fixed connection to the abutment, which dissipates as one moves away from the

abutment. The HL-93 contraction load case produces the maximum bottom fiber stress near the mid-span of the first span. This load case includes service loads for dead, live, and thermal loads. Near the middle of the first span, girder bottom fiber stress reaches 22 ksi in tension under this load case. At this location, superstructure contraction increases girder demands already created by gravity loads. Negative moment regions reach maximum compressive stresses around 21 ksi due to gravity loads; however, thermally induced stresses reach only 1 ksi. Thermal expansion increases girder bottom fiber stresses in negative moment regions and relieves bottom fiber stresses in positive moment regions. Similarly, thermal contraction relieves girder bottom fiber stresses in negative moment regions and increases bottom fiber stresses in positive moment regions.

When skew is introduced, the same trends as observed in Figure 29 hold; however, magnitudes are altered. Figures 31 and 32 show the girder bottom fiber stress for each girder section at the abutment for an IAB with four 100 ft spans. These stresses represent the girder bottom stress resulting from thermal expansion and thermal contraction of the superstructure alone (no gravity loads). As bridge skew is increased, the bending stress magnitudes in each girder decrease; or, in other words, strong-axis bending of the girder is reduced as skew is increased. This phenomenon is more pronounced for thermal expansion than thermal contraction. For example, increasing the skew from 0° to 30° results in a 2 ksi reduction in bottom fiber stress due to thermal expansion and effectively no reduction in bottom fiber stress due to thermal contraction (at the obtuse corner, where girder demands are largest). As skew increases, the boundary conditions of the abutment gravitate toward increased transverse resistance and decreased longitudinal resistance of the bridge deck. Thus, strong-axis bending demands reduce, but weak-axis bending demands increase due to significant transverse displacement of the abutment.

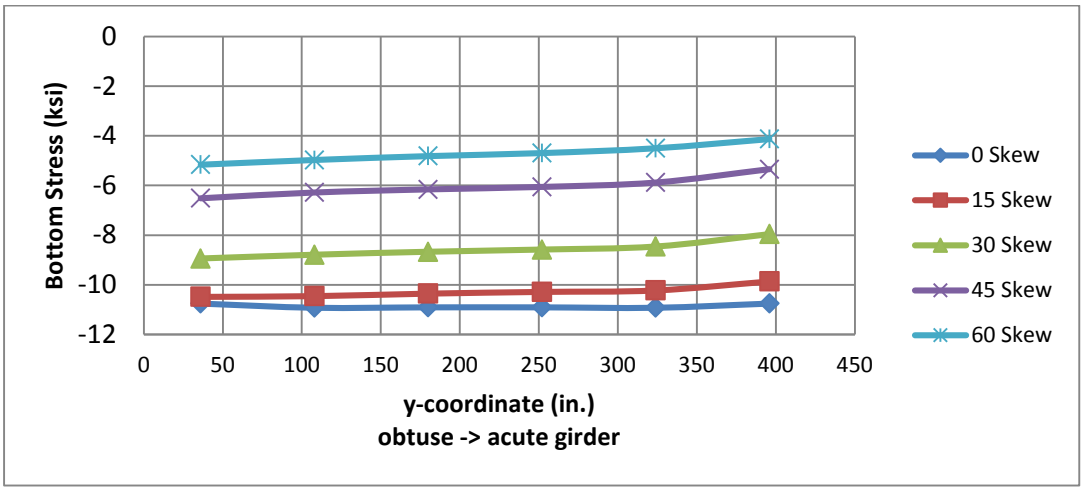

Figure 30. Girder bottom flange stresses at the abutment due to pure positive thermal loading for four-span bridges with 100 ft spans and HP14×73 piles.

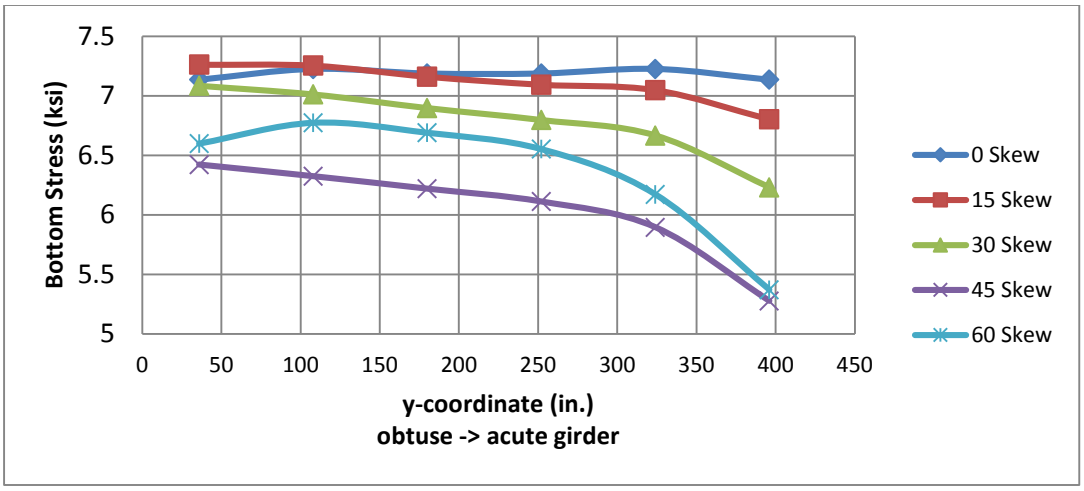

Figure 31. Girder bottom flange stresses at the abutment due to pure negative thermal loading for four-span bridges with 100 ft spans and HP14×73 piles.

As with the pile strains, the superstructure rotational stiffness plays a role in increasing the maximum girder demands. Figure 32 compares bottom flange stresses at the abutment from pure thermal expansion for the same girder designation, but different span length combinations, and thus different k_θ values, of 45° skew bridges with HP14×73 piles. Analogous plots for different skews take on the same shape, but they differ in magnitude. For a given EEL, pile size, and girder design, maximum girder stresses increase as k_θ increases. All else equal, increasing superstructure rotational stiffness increases the bending moment that develops at the girder ends when the bridge tries to expand due to an increase in temperature, which acts to increase the magnitudes of the thermally induced stresses in the girder. At larger EEL, pile yielding leads to a reduction in restraint that the abutment imposes on the superstructure, which leads to an apparent "softening" shown in the girder stress vs. EEL plot. The girder bottom stress trends are similar for load cases that include thermal contraction; however, the magnitudes are governed by thermal expansion load cases due to the additional resistance that the backfill force places on the abutment. The backfill force—which does not engage during thermal contraction of the bridge—acts in the opposite direction of the internal girder axial force, and it also creates an external moment on the abutment that is in opposition to the superstructure internal moment.

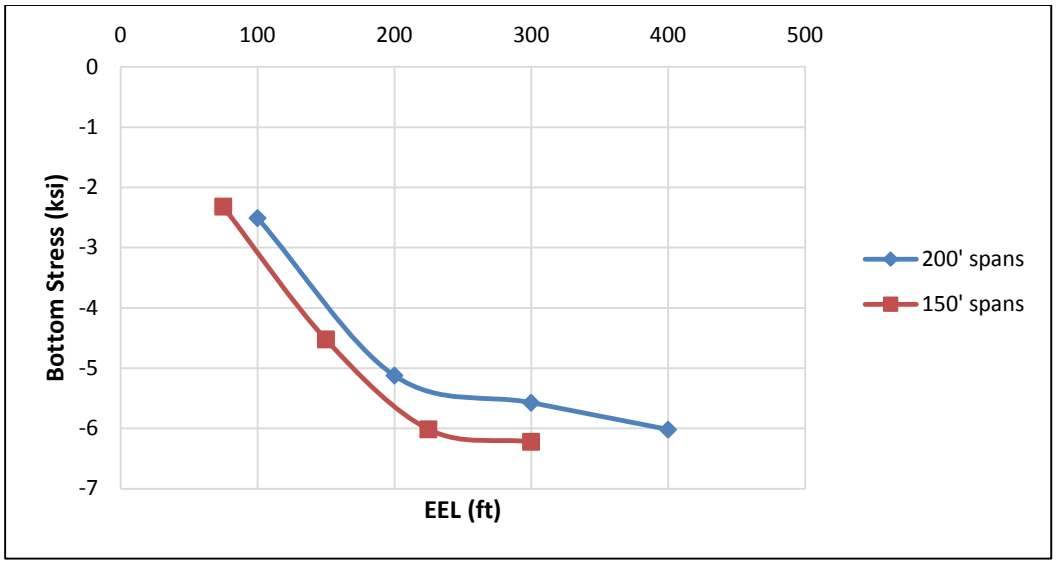

Figure 32. Girder bottom flange stresses at the abutment due to pure positive thermal loading for 45° skew bridges with HP14×73 piles.

Pile size acts to influence observed girder stresses as well. Figure 33 plots girder bottom fiber stresses (compressive) at the abutment (pure positive thermal loading) for non-skew models with all 100 ft spans. With k_θ essentially held constant in all of these cases, the maximum girder stresses increase with increasing EEL and pile stiffness. The maximum girder stress reaches 25 ksi for bridges with larger piles as EEL increases past 500 ft. For smaller piles (HP10 and HP12), pile yielding occurs once EEL increases past 200 ft, and maximum girder stress asymptotically approaches 10 ksi and 13 ksi for bridges with HP10 and HP12 piles, respectively.

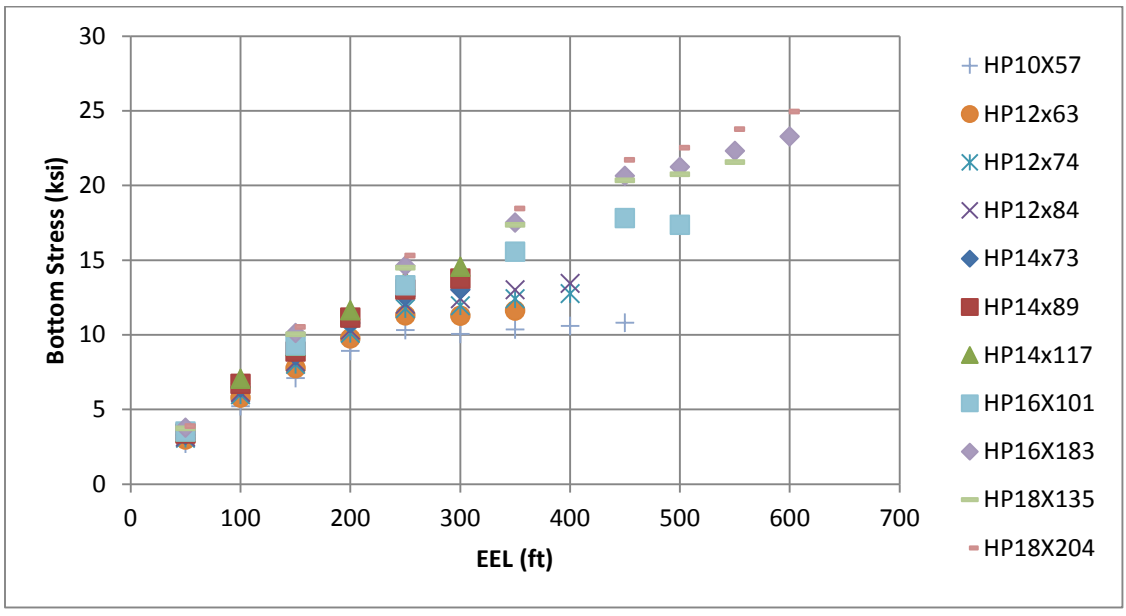

Figure 33. Girder bottom flange stresses at the abutment due to pure positive thermal loading for non-skew bridges with 100 ft spans.

CHAPTER 6: RESULTS FOR SECONDARY PARAMETERS

Secondary parameters that were also investigated include end-span ratio, bridge width, backfill properties, foundation soil properties, number of piles in foundation, pile top relief, strong-axis H-pile orientation, shell pile sections (pipe piles), and abutment height. These parameters were seen to have effects that would add to the responses observed in the primary study. For this reason, with the exception of end-span ratio and bridge width, secondary parameters were studied for non-skew bridges only. Various bridge responses to uniform temperature loads were investigated for each secondary parameter model, including pile deflections, peak pile strains, and girder forces/moments. Each secondary parameter presents a different boundary condition on the pile–abutment–superstructure interface, thus resulting in different structural demands. These results may also be used to adjust predicted IAB demands for bridges that are represented by primary parameter models but have different soil or pile design conditions.

6.1 END-SPAN RATIO

Models with varying end-span ratios were created for both non-skew and skewed bridges. The same trends are seen regardless of skew. Increased skew acts mainly to increase pile demands and decrease girder stresses, as discussed in the earlier chapter. As expected, smaller end spans result in larger k_θ values for a given EEL, causing pile strains and girder stresses to increase. Models with shorter end spans (and thus larger k_θ values) produce larger demands under pure thermal loads. However, shorter end spans distribute less gravity load to the abutment than longer spans, and therefore may produce smaller dead and live load demands than long spans.

Figure 34 compares compressive girder bottom fiber stresses at the abutment under pure positive thermal loading for non-skew bridges with HP14×73 piles with various span length combinations. As stated in Section 5.4, when pile size, EEL, and girder design are held equal, girder stresses increase with increased k_θ. This can be seen when comparing the uniform 100 ft span cases with the cases that have 100 ft interior spans and 50 ft end spans, which were both designed with W36×194 girders. Cases with shorter end spans have a larger k_θ, which leads to slightly higher stress for the same EEL. Select models were run with skew and the same trends were observed; the only difference was that stresses are lower with higher skews, as discussed in Chapter 5.

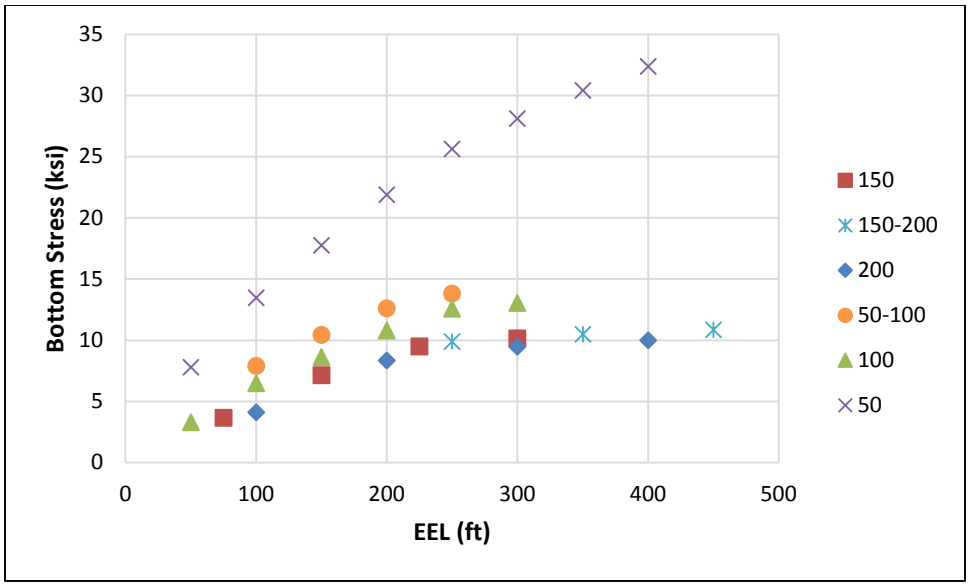

Figure 34. Girder bottom flange stresses (compressive) at the abutment due to pure positive thermal loading for non-skew bridges with HP14×73 piles.

A similar effect can be seen with the pile strains. Figure 35 shows pile strains due to pure positive thermal loading for two non-skew bridges of the same girder design for two different pile sizes. As was discussed in Chapter 5, lower strains are seen with larger piles because more demand is placed on the girders. Like what was observed with the girder stresses discussed above, the bridges with smaller end spans, and thus higher k_θ values, exhibit larger pile strains. Again, the end-span ratio models display the same skew effect with pile strains as was described in Chapter 5. However, when approaching higher skew values, the smaller end-span ratio has slightly less of an effect on pile strains. This is made evident by Figure 36, which plots pure positive thermal strains for non-skew and 45° skew bridges with the same girder design.

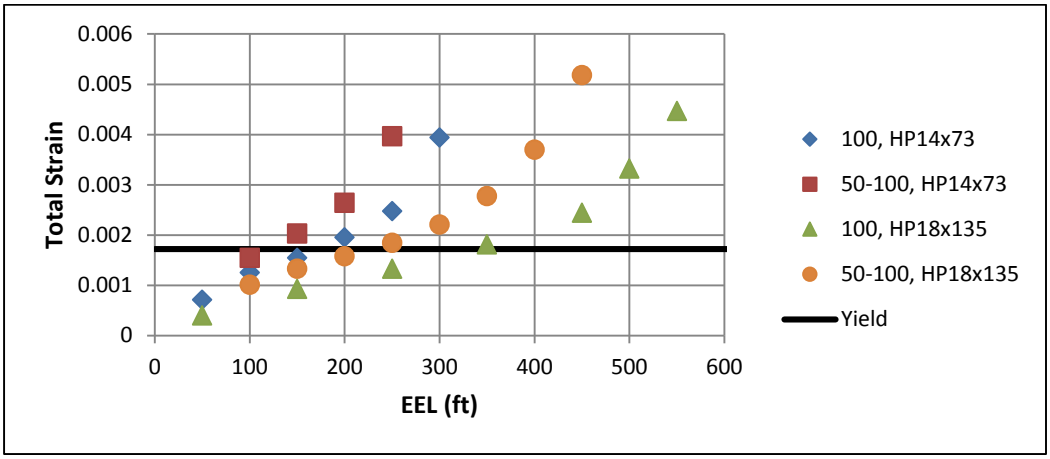

Figure 35. Pile strain due to pure positive thermal loading for non-skew bridges.

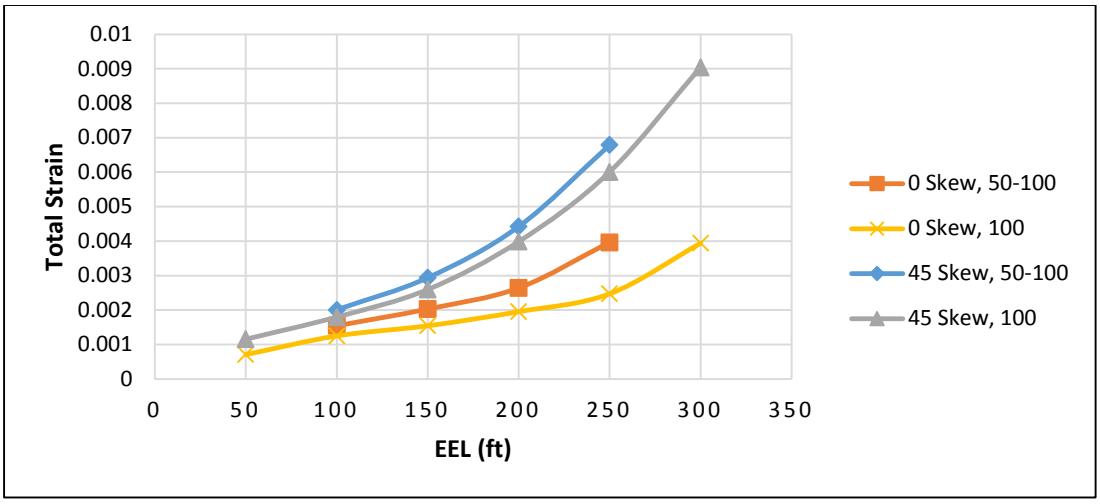

Figure 36. Total pile strain due to pure positive thermal loading for bridges with 100 ft spans and HP14×73 piles.

6.2 BRIDGE WIDTH

When skew is involved, bridge width can have a significant effect on pile strains. As stated in Chapter 5, increased skew acts to increase bridge transverse movement, which adds additional strong-axis bending demand on the piles. Wider bridges then amplify this transverse movement and increased bending demands. Figure 37 shows pile strains due to positive thermal loading for bridges with 100 ft spans and HP14×73 piles, with skew varied from 0° to 30° and width varied from the default 36 ft to 96 ft. It can be seen that the difference between the non-skew bridges is small; however, when looking at the 30° skew bridges, pile strains are significantly increased along with width. For example, for 30° skew bridges with an EEL of 200 ft, there is a 33.7% increase in total strain when the width increases from 36 ft to 96 ft.

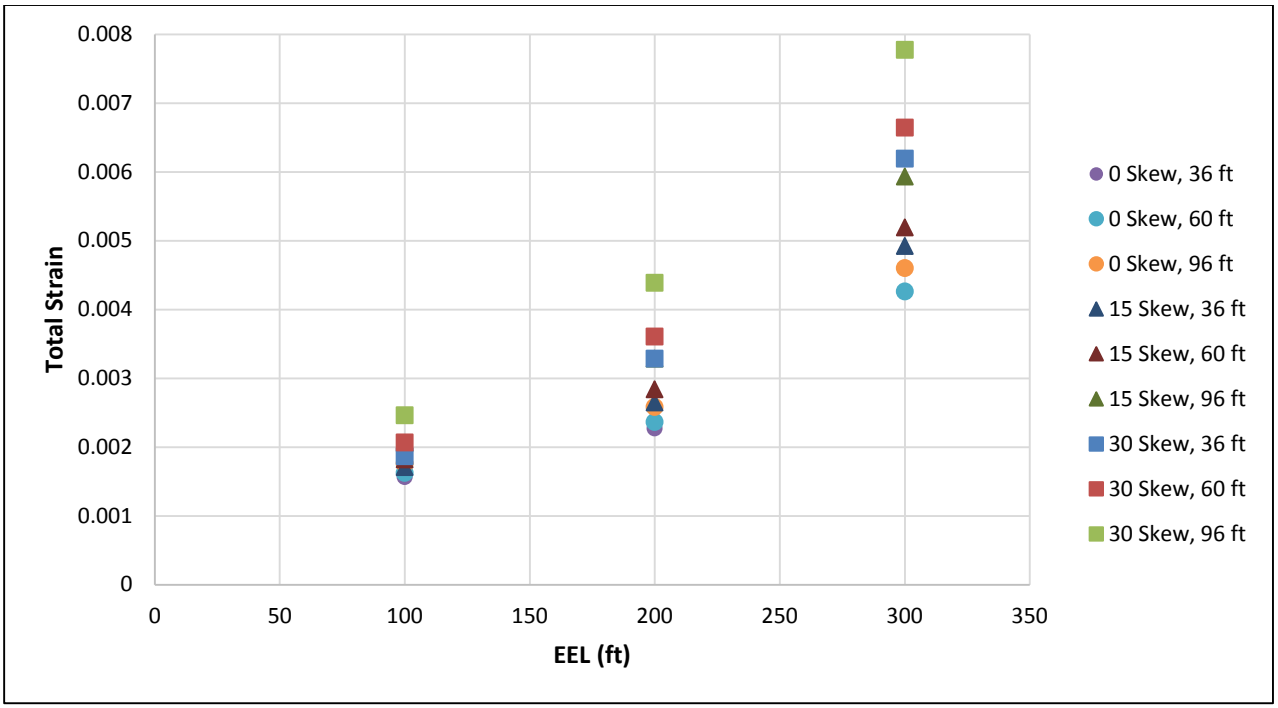

Figure 37. Pile strains due to positive thermal loading for bridges with 100 ft spans and HP14×73 piles.

The combined effect of width and skew is even more apparent in Figures 39 and 40. Both plots are again for positive thermal loading and display pile strains for a fixed EEL of 200 ft and various span lengths. For a given span length, the slope of the lines of width versus pile strain increases as skew increases from 0° to 45°. Clearly, for pile strain values, width gains significance when skew is increased. These two plots also display trends discussed in Chapter 5 regarding k_θ and pile size. As expected, the bridges with 200 ft spans exhibit higher pile strains because they have a larger value of k_θ. In comparing Figure 38 with Figure 39, it can be seen that increased pile size decreases pile strains, since more demand is placed on the superstructure.

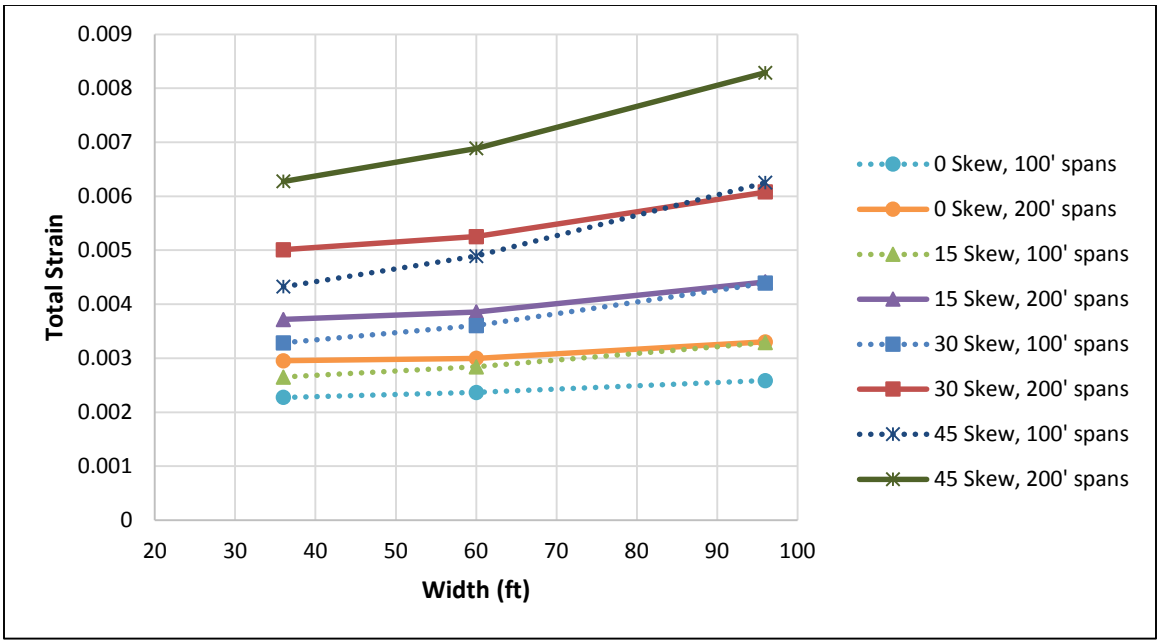

Figure 38. Pile strains due to positive thermal loading for bridges with an EEL of 200 ft and HP14×73 piles.

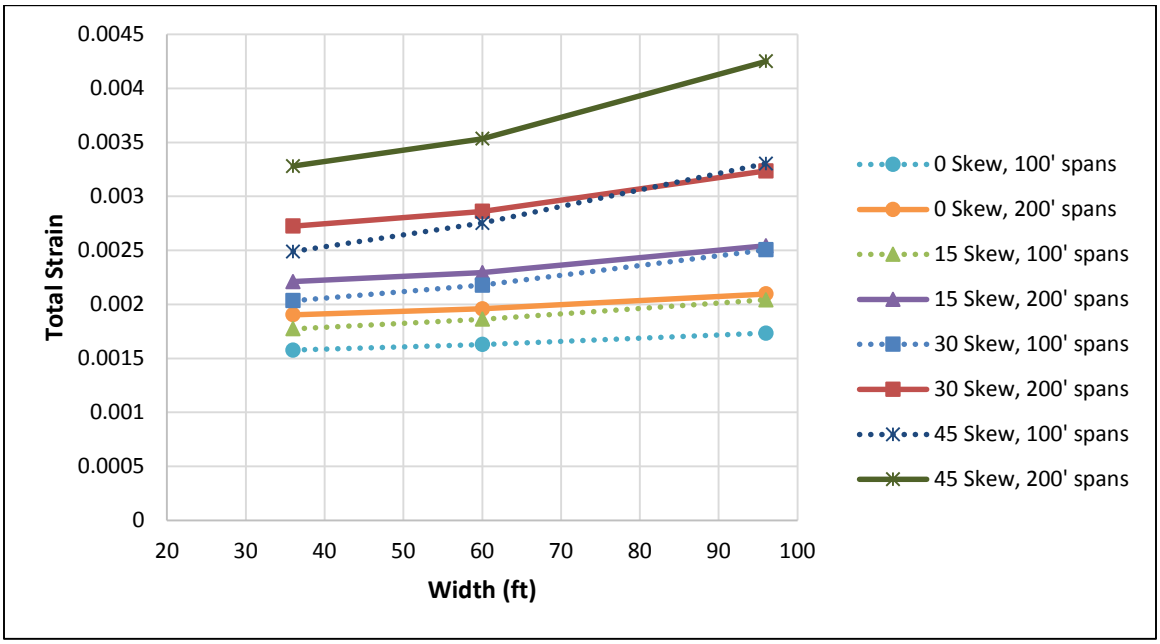

Figure 39. Pile strains due to positive thermal loading for bridges with an EEL of 200 ft and HP14×117 piles.

Although width can play a significant role in increasing expected pile strains, it has little effect on girder demands. Figure 40 shows the bottom flange stress due to positive thermal loading for the three different widths considered in the study of a six-span, 30° skew bridge with 100 ft spans and

HP14×117 piles. The larger skewed bridges shows greater variation in pile strains as width increases; however, that does not hold for the girder stresses. Little to no variation is seen in the observed girder stresses between the three different widths, indicating that the effect of width is negligible.

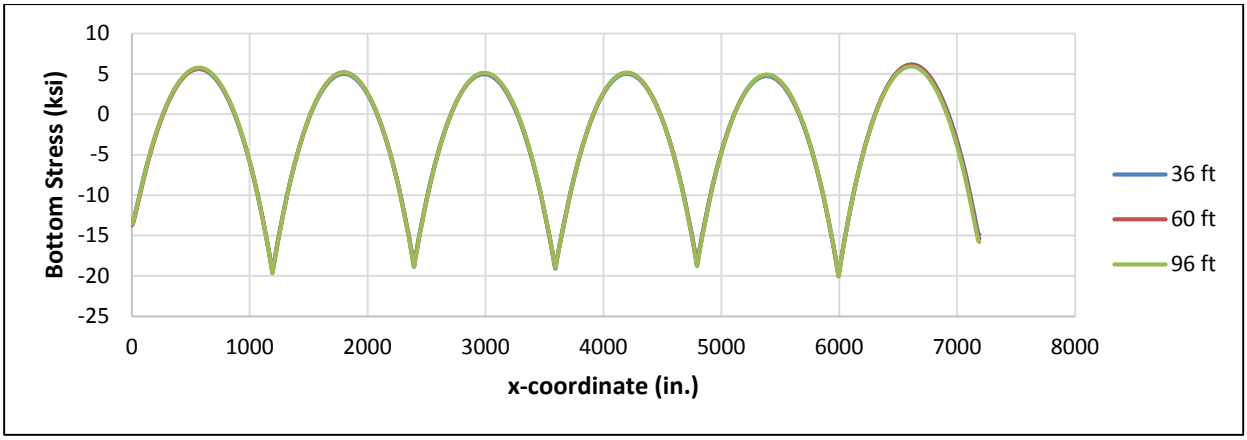

Figure 40. Bottom stress due to positive thermal loading for six-span, 30° skew bridges of various widths with 100 ft spans and HP14×117 piles.

6.3 EXTREME SKEW

Results for the extreme skew cases were presented along with the primary parameter study in Chapter 5. Trends for the 60° skew models generally followed the effects of increased skew as seen in the primary study of 0° to 45° skew.

6.4 PILE SOIL STIFFNESS

Foundation soil properties play a role in pile deflection, pile demands, and superstructure demands under thermal loads. In general, the pile demands due to positive thermal and negative thermal loads are consistent when the loose sand backfill is present. The positive thermal results will be discussed here. Figure 41 shows the peak pile strains for the models with varying soil foundation types. Pile demands are largely constant—regardless of soil type—for EEL up to 200 ft. The plot indicates that stronger soils provide for an increased demand at the pile. While stiffer soil does minimize the pile head lateral deflection, it also increases the elevation at which the pile is essentially fixed, as seen in Figure 42. This decreases the effective length of the pile that resists the lateral movement and rotation of the pile head, allowing for larger internal bending moments (see Figure 43). Thus, as soils become stiffer, the pile demand and superstructure demand both increase under thermal loads.

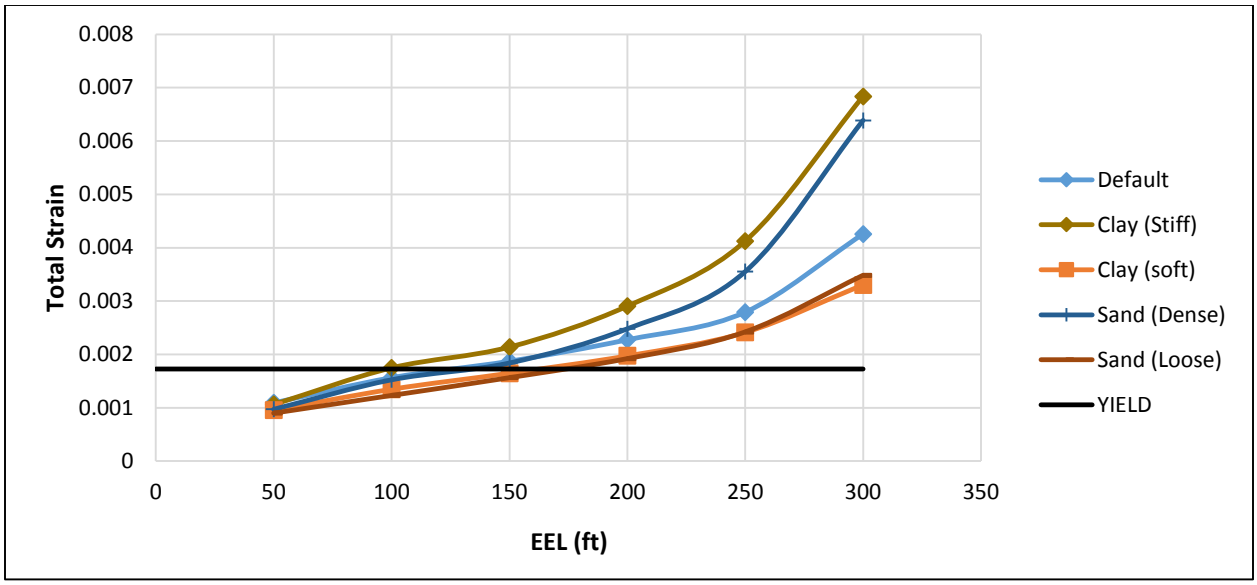

Figure 41. Total pile strains due to positive thermal loading for non-skew bridges with 100 ft spans and HP14×73 piles.

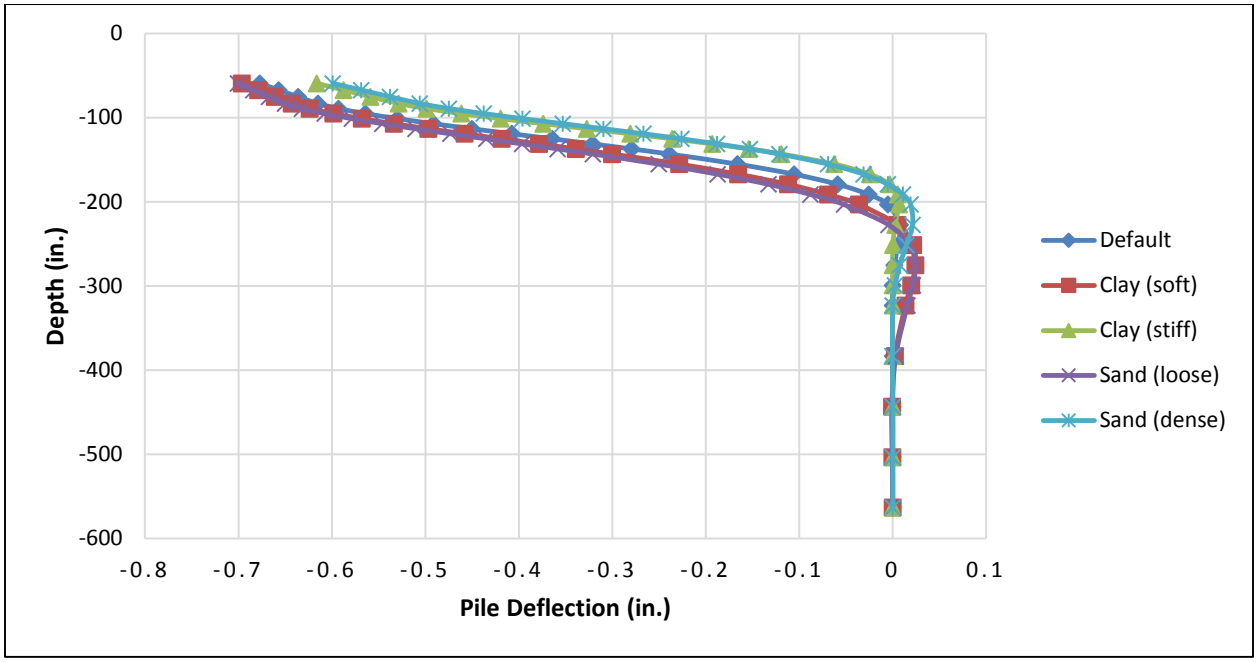

Figure 42. Pile deflection due to positive thermal loading for a three-span, non-skew IAB with 100 ft spans and HP14×73 piles.

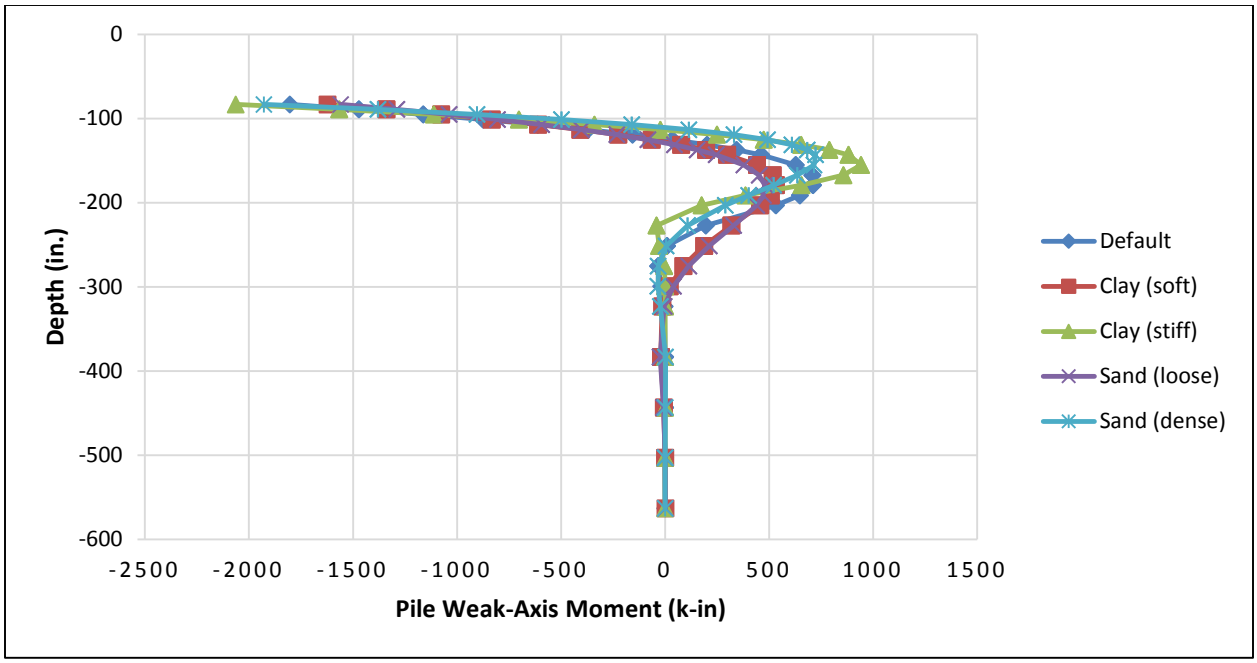

Figure 43. Pile weak-axis moments due to positive thermal loading for a three-span, non-skew IAB with 100 ft spans and HP14×73 piles.

6.5 ABUTMENT BACKFILL STIFFNESS

Backfill stiffness has significant influence on whether thermal expansion or thermal contraction of the superstructure will govern pile demands (excluding live loads). This is because the backfill force acts to reduce the moments applied to the pile head; thus, a stiffer backfill resistance will provide increased relief on pile head demands. Figure 44 shows the peak pile strain for the default and stiff backfill models at various bridge EELs under positive thermal and negative thermal loads (both including dead load), respectively. Because the backfill is engaged only during the expansion case, both results for the two contraction cases coincide. In expansion, a large decrease in peak strain is recovered due to the resistance of the stiff backfill. At a relatively large EEL of 300 ft, the stiff backfill reduces the peak pile strain due to expansion by 56%.

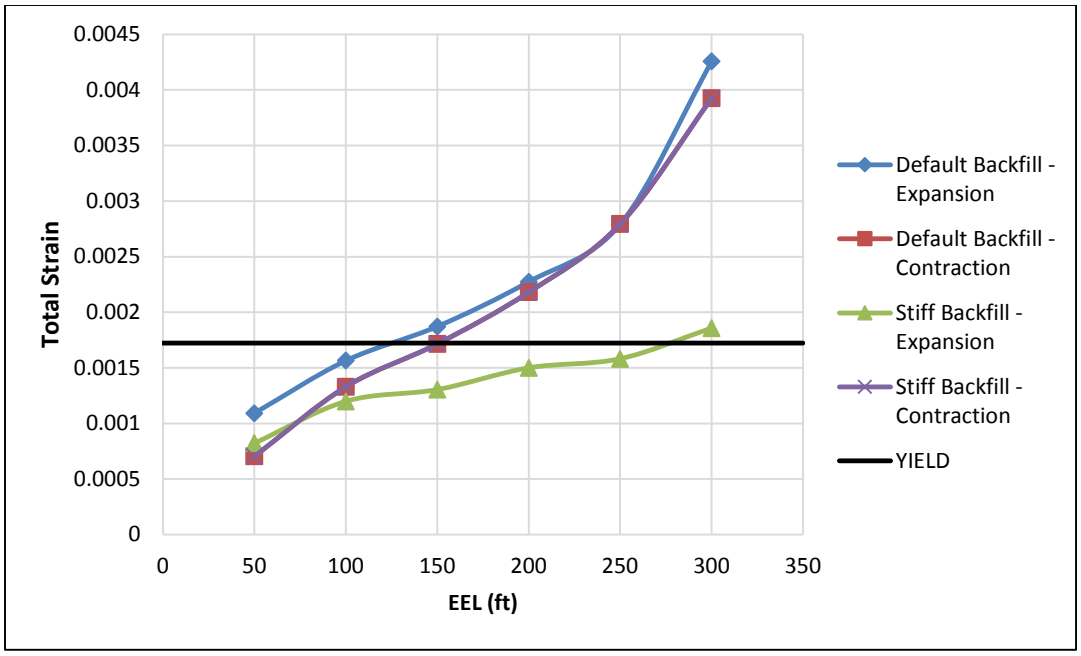

Figure 44. Peak pile strain for default and stiff backfill models due to positive thermal and negative thermal loads

While the stiff backfill causes the thermal contraction case to govern under positive thermal and negative thermal loads (these include dead loads), the addition of extreme live load effects causes the HL93-EXP case to govern over the HL93-CON case (except for very large EEL). Also note that the maximum peak strain due to thermal loads is relatively constant regardless of whether a stiff backfill is present (i.e., the maximum demand due to positive thermal or negative thermal loads is relatively constant).

This increased resistance on the backfill also results in larger internal force (axial force and bending moment) demands at the superstructure cross-section for positive thermal loads. Such is evident in Figure 45, which compares the total bottom flange stress values at the abutment for default and backfill models. The increased backfill force provides more axial and rotational restraint on the abutment, causing increased internal forces within the girder section.

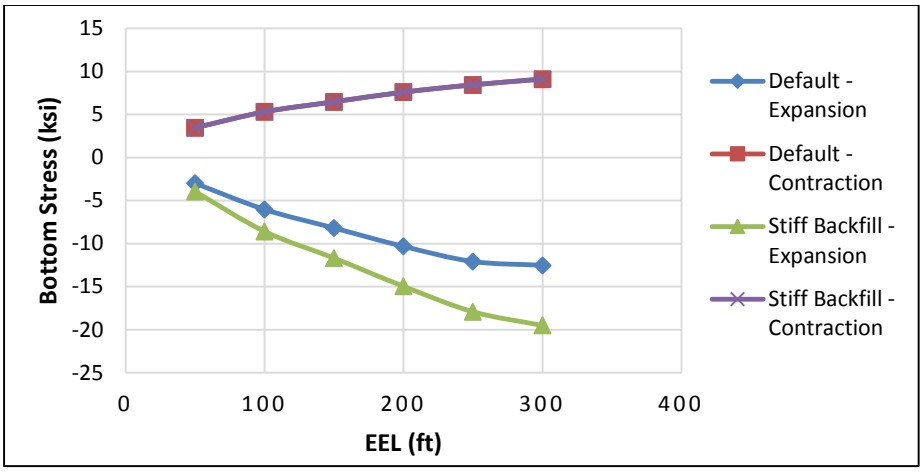

Figure 45. Girder bottom flange stress for default and stiff backfill models due to positive thermal and negative thermal loads.

6.6 PILE CONDITIONS

Pile details influence the stiffness of the substructure, which controls the structural demands of IABs. Pile orientation (weak axis versus strong axis) still remains a debated topic in IAB design. Weak-axis orientation is typically prescribed in order to maximize bridge expansion/contraction under thermal loads, effectively reducing the forces that are built up due to the restraint that the substructure imposes on the superstructure. However, weak-axis orientation allows larger deformations in the piles, and plastification at the pile head is much more likely to occur. Pile top relief is another method used to prescribe more pile flexibility. In this method, holes are predrilled at the pile locations (usually to a depth of 10 ft below the pile head location) and that portion of the pile is encased in a soft bentonite slurry. This provides for a more flexible pile foundation, reducing the internal forces within the piles and superstructure components. Designs with double piles include piles spaced at half the spacing of the girders, which simply provides more structural capacity of the pile group.

Figure 46 shows the peak positive thermal (dead plus positive thermal) loading pile strains for each of these three cases compared with the default parameter case. The pile relief case simply reduces the lateral restraint placed on the piles by the soil—thus, the pile relief case has the same effect (and benefits) of softer/weaker soils located at the foundation. Pile deflections are larger, but the longer effective length of the pile is increased, which increases the flexibility of the pile and reduces pile bending moments. Double piles and strong-axis orientation both effectively provide an increased stiffness at the foundation. This increased stiffness provides for reduced pile deflection and reduced peak pile strains, but larger internal forces at the pile and girder cross-sections. One benefit of the double piles is that this increased pile demand is distributed over twice the number of piles (compared with the default case); thus, individual pile moments are reduced. While the strong-axis piles attract larger forces than the default piles, they exhibit much smaller peak strains due to the sharp increase in area moment of inertia.

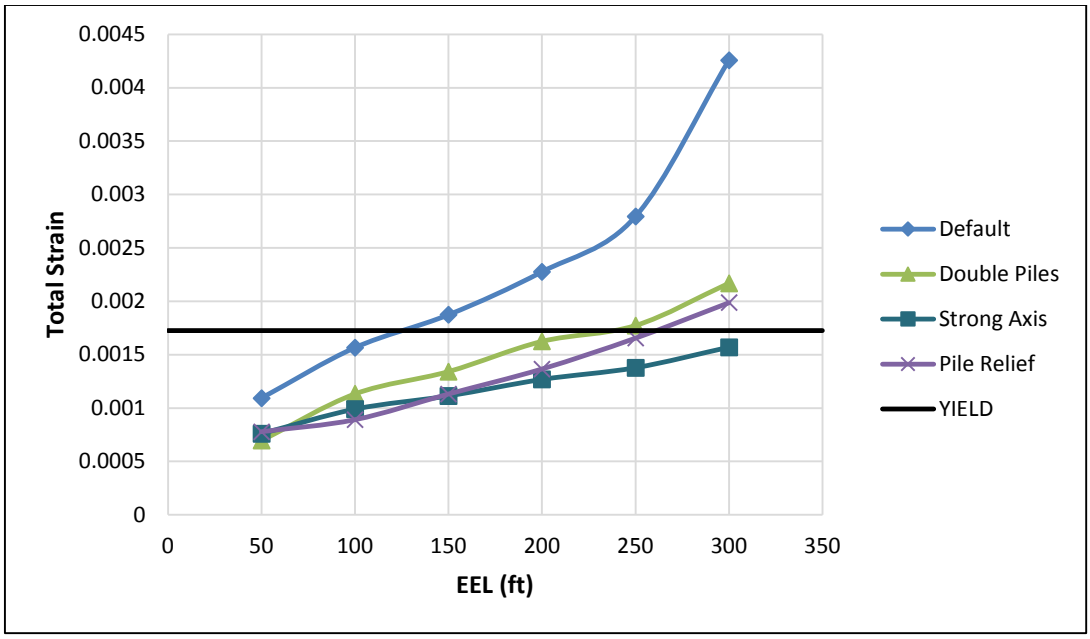

Figure 46. Peak pile strains due to positive thermal loads for models with different pile details.

The two steel pipe pile sections that were tested showed interesting results. The pipe piles provided more lateral stiffness (and bending moment capacity) than the H-piles oriented in weak-axis bending. However, at the onset of yielding in the pipe sections, the effective moment of inertia—that is, the moment of inertia of the section that has not yet yielded—sharply decreases as the pile head continues to rotate under increased loading. This is not the case for H-piles oriented in weak-axis bending (and could even be somewhat different for pipe piles if they were filled with concrete). Figure 47 shows the peak pile strains of the pipe sections compared with those of the default, double piles, and strong-axis cases. At small values of EEL (up to 150 ft), peak strains are relatively constant across the pile designs. However, once yielding occurs in the pipe piles, the peak strain value sharply increases as EEL (which is directly related to the applied pile demand) increases. The default case, which undergoes yielding around the same EEL, shows a much softer increase in strain past yielding. Yielding occurs around the same EEL for the pipe sections and the weak-axis H-piles (default) due to their similarity in section stiffness. The double piles and strong-axis cases exhibit more soil resistance (due to a larger number of piles) and much larger stiffness (due to strong-axis moment of inertia), respectively, preventing yielding at smaller values of EEL. The flange orientation of the default case (weak-axis orientation) prevents a sharp loss of stiffness as the pile head undergoes plastification, which is why the peak pile strain does not sharply increase after yielding has occurred. While the strong-axis models did not exhibit a large enough EEL to impose pile yielding, it is expected that the extrapolation of its peak pile strain curve shown in Figure 47 would have a shape similar to that of the pipe sections. This is because the effective stiffness of the strong-axis H-piles also sharply reduces once the flanges completely yield, leaving the slender web to resist further pile head rotation.

These results indicate that H-pile sections allow for bridge configurations to reach much larger EELs before parts of the pile section approach strain hardening. The H-piles oriented in strong-axis bending simply provide more stiffness—thus resulting in larger moment capacity than the pipe sections—and

the H-piles oriented in weak-axis bending exhibit more “ductile” behavior as strains increase past yield.

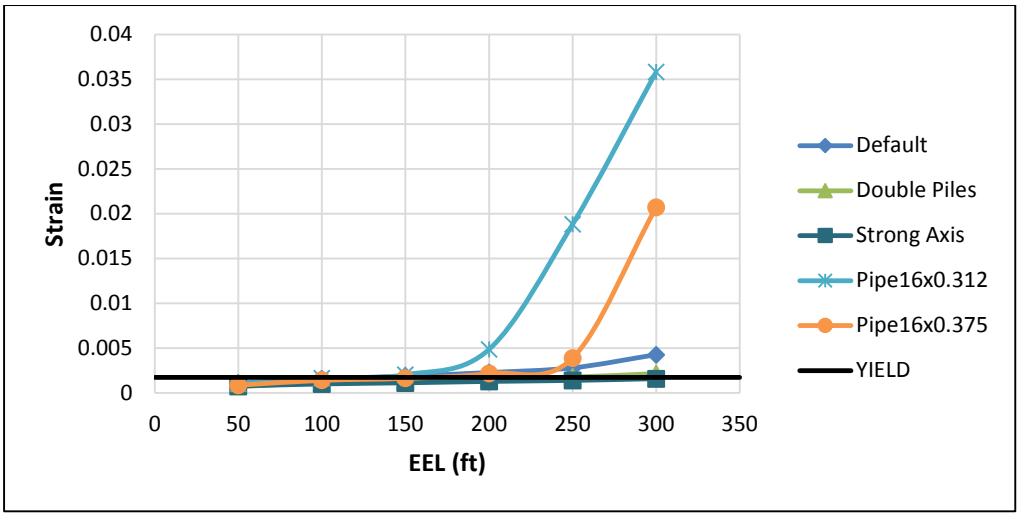

Figure 47. Elastic vs. plastic peak pile strains for different pile designs under positive thermal loads.

To sum up the effect of each pile and soil condition on the internal forces of the pile, weak-axis moments at the pile head (strong-axis moment for the strong axis–oriented model) for a select three-span bridge configuration are reported in Table 8. In comparing with the default case, it becomes clear which parameters act to increase or decrease pile strains induced by thermal loadings.

Table 8. Pile Head Moments for Secondary Parameters for a Three-Span, Non-Skew IAB with HP14×73 Piles

	Positive Thermal	Negative Thermal
Default	–1804	1612
Clay (Soft)	–1621	1458
Clay (Stiff)	–2064	1897
Double Piles	–1280	1209
Pile Top Relief	–1027	1000
Pipe 16×0312	–3181	3075
Pipe 16×0375	–3214	3123
Sand (Dense)	–1927	1789
Sand (Loose)	–1559	1264
Stiff Backfill	–1183	1612
Strong Axis	–2232	2118

6.7 ABUTMENT HEIGHT

Abutment depth influences the backfill passive resistance and overburden applied to the soil springs resisting pile deflection during thermal expansion. Abutment depth also plays a role in abutment rotation; because the displacement at the top of the abutment is primarily dependent on EEL and temperature change, the abutment depth dictates pile head deflections. For the case with deeper abutments (all else equal), pile strains are significantly reduced. Figure 48 shows the peak pile strains due to thermal loads. The effects of the increased backfill resistance are seen in the abutment case under positive thermal loads, with a great disparity between strains due to thermal expansion and contraction.

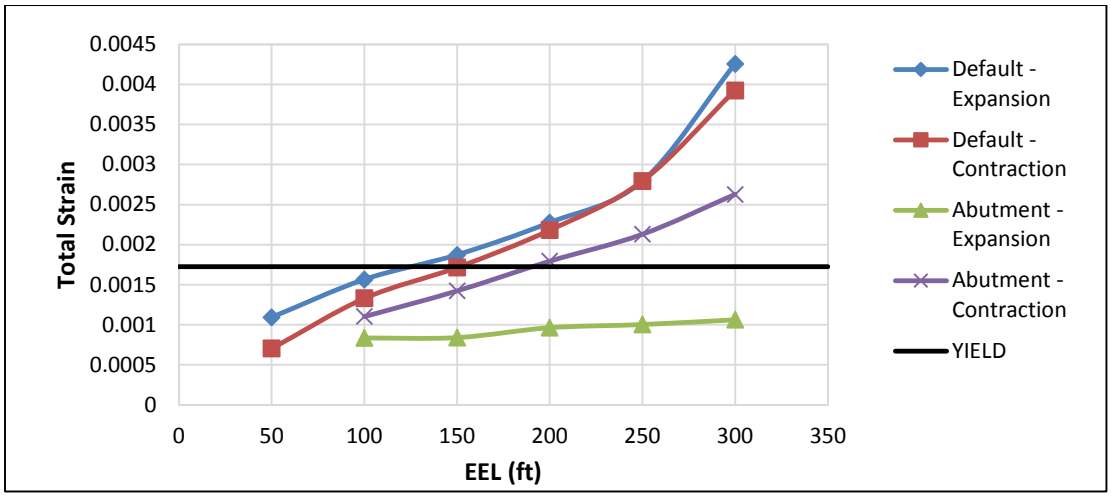

Figure 48. Peak pile strains for default and abutment cases under positive thermal and negative thermal loads.

Though increasing abutment depth serves to decrease service load pile demands, it does present an increase in superstructure demands. Figure 49 shows the composite section bending moment demands for IAB cases with the same girder proportions but with a different abutment height (100_abut) or a different span length combination ("50–100," which provides a varied superstructure rotational stiffness). For a given EEL, the superstructure bending moment demand significantly increases as the abutment depth is increased from 7.27 ft to 10.6 ft. The effects of the increased superstructure rotational stiffness is shown by the 50–100 case as presented in Section 6.1. These results indicate that abutment height influences superstructure demands more than superstructure rotational stiffness does. The increased moment demand is due to the larger rotations of the abutment in the case of the deep abutments. As shown in Figure 50, the deeper abutment mitigates pile head deflection, which allows for larger abutment rotations (using small angle theory, the proportion of $\Delta_2/\ \Delta_3$ is much larger than the proportion of abutment heights). These larger abutment rotations (which relieve pile bending) act to provide more rotational restraint—and, therefore, more bending moment demand—to the superstructure. Additionally, weak-axis pile hinging acts to soften the rotational restraint that the pile provides to the superstructure. In Figure 49, the default case exhibits a plateau in girder bending moments due to pile plasticity, while the abutment case allows for superstructure bending moment to increase as EEL increases (no pile yielding has occurred).

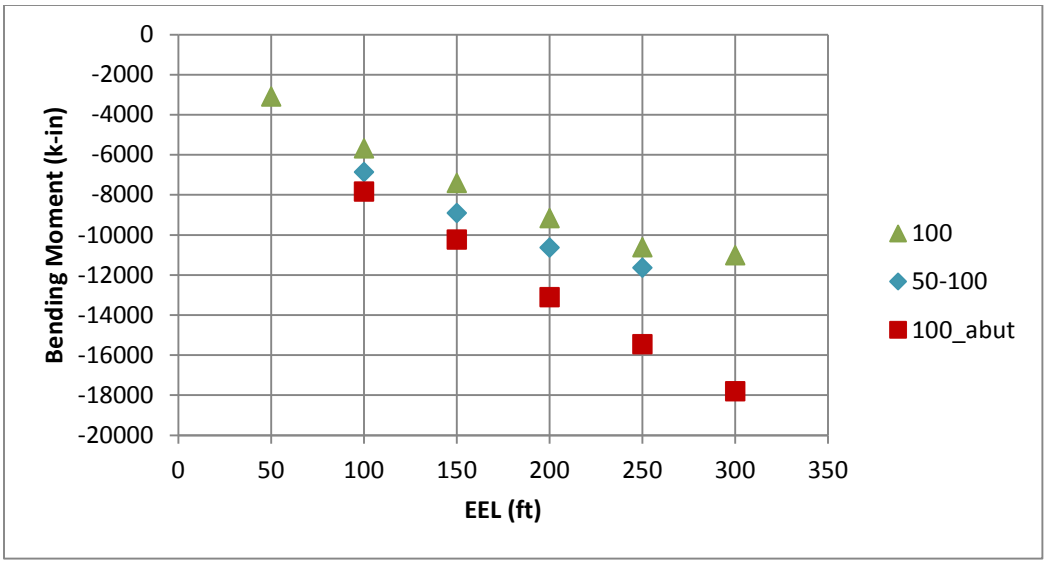

Figure 49. Composite girder section moment demand due to pure positive thermal load.

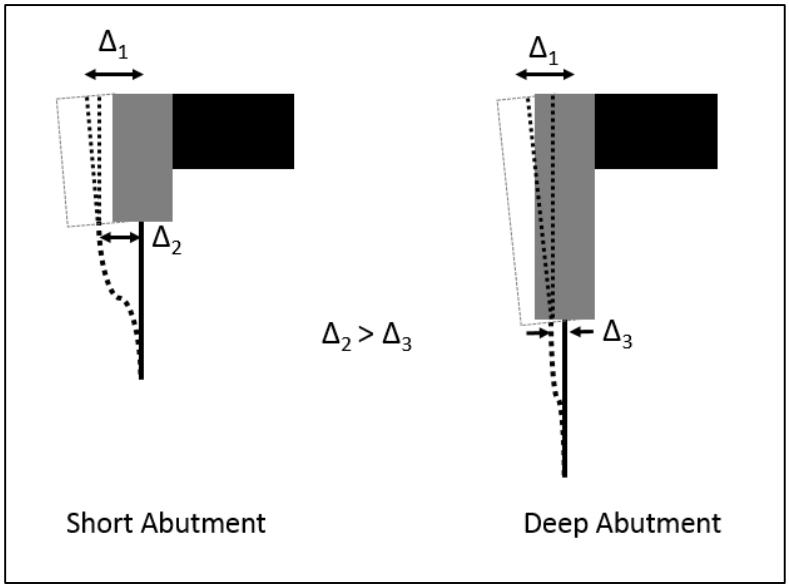

Figure 50. Abutment depth effects under positive thermal loads.

CHAPTER 7: DESIGN RECOMMENDATIONS AND CONSIDERATIONS

7.1 NONLINEAR REGRESSION EQUATIONS FOR KEY DESIGN VALUES

Numerical equations are useful tools for quick preliminary calculations of estimated stresses or strains. Expressions have been developed for both maximum pile strain and maximum girder stress, which align with data collected from the base suite of parametric study models. These expressions do not represent any LRFD load combinations, but rather they report service-level behavior instead; they do not reflect any possible contributions from factors such as section loss or additional eccentricity caused by pile driving tolerances.

7.1.1 Pile Strains

Maximum pile strain under thermal loading has been observed to closely follow a third-degree polynomial when plotted against EEL for a given pile and superstructure detail. If all piles plot the same general curve shape, their behavior can be scaled to a reference response shape. This reference shape will allow for easy determination of the pile strain under a certain set of independent variables, otherwise known as predictors, using an empirical relationship.

MATLAB was then used to perform parametric nonlinear regression analysis in the development of calibrated pile strain prediction models.

Maximum pile strains that occur at the abutment–pile interface due to positive thermal loading were compiled for all bridge models that were created for the primary parameter study (0 to 45° skew). Because expansion controlled for the primary models of the study, using the developed numerical model would be a conservative estimate for strains due to thermal contraction. The nonlinear regression was performed using bridge EEL, k_θ, pile cross-sectional area, pile weak-axis moment of inertia, and skew. These parameters were used to develop a pile strain influence coefficient, α_{pile}, which could then be used in a cubic polynomial to predict pile strain. The developed expressions for predicting pile strain are as follows:

$$\alpha_{pile} = EEL^{0.4699} k_\theta^{0.1336} I_{y,pile}^{0.0708} A_{pile}^{-0.4648} \cos(Skew)^{-0.5155}$$

$$\varepsilon_{pile} = (3.7112 \times 10^{-7})\alpha_{pile}^3 - (1.8059 \times 10^{-5})\alpha_{pile}^2 + (2.7614 \times 10^{-4})\alpha_{pile}$$

where EEL is in ft, k_θ is in k-in./rad, I_y is in in.^{4}, A is in in.^{2}, and skew is in radians. Figure 51 displays this cubic curve plotted over the collection of modeled data.

It should be noted that the above equations are valid only for the assumptions of the primary parameter models—that is, bridges of up to 45° skew with the default soil properties, 36 ft width, and 1:1 end-span ratios. If soil properties, pile conditions, width, or end-span ratio were to be altered, results might not align with the curve.

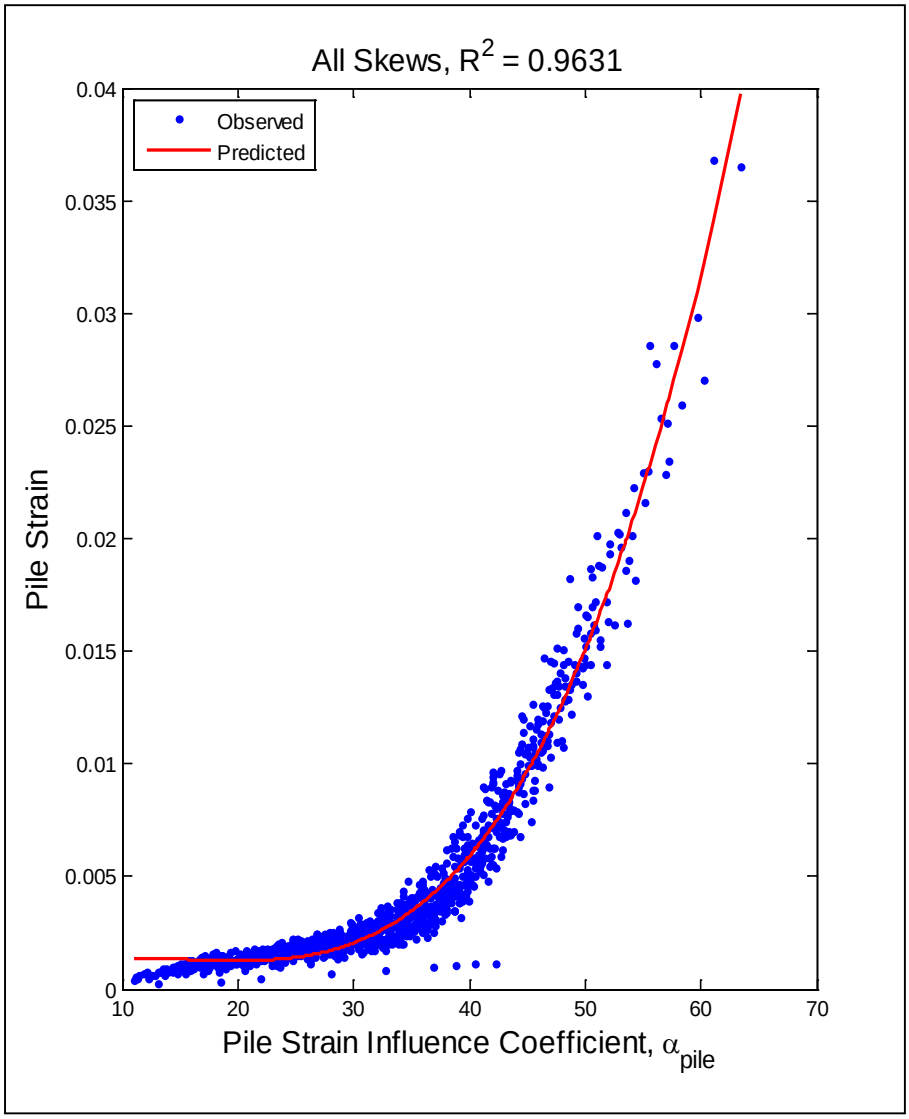

Figure 51. Pile strain data from parametric models against developed cubic curve.

7.1.2 Girder Stresses

Similar to the procedure for pile strains, bottom fiber stresses located at the abutment from a middle girder (near the bridge centerline) due to pure positive thermal loads were compiled for the base set of bridge models (0° to 45° skew) and examined to determine the relative influence of different parameters. As was discussed in Section 5.4, the bottom flange stress values were computed from strong axis flexure and girder axial force alone. It was determined that a linear relationship was sufficient in capturing the trends of girder stress, when using a scaled value of EEL. A nonlinear regression was performed with MATLAB using bridge EEL, girder cross-sectional area, pile weak-axis moment of inertia, and skew. These parameters were used to develop a pile strain influence coefficient, α_{girder}, which could then be used in a linear expression to predict pile strain. The developed expressions for predicting girder bottom fiber stress are as follows:

$$\alpha_{girder} = EEL^{0.5321} I_{y,pile}^{0.1840} A_{girder}^{-0.9273} \cos(Skew)^{1.8885}$$

$$\sigma_{girder} = (8.9800)\alpha_{girder}$$

where σ is in ksi, EEL is in ft, I_y is in in.^{4}, A is in in.^{2}, and skew is in radians. Figure 52 displays this linear expression over the collection of modeled data.

Again, the expressions above are valid only for the assumptions of the primary parameter models. Alterations would be needed following the trends discussed for the secondary parameters if bridge conditions do not align with the default of this study. It is also important to note that this regression predicts higher-than-expected girder stresses for the outlier cases, which are bridges of zero skew with large piles, large EELs, and small span lengths.

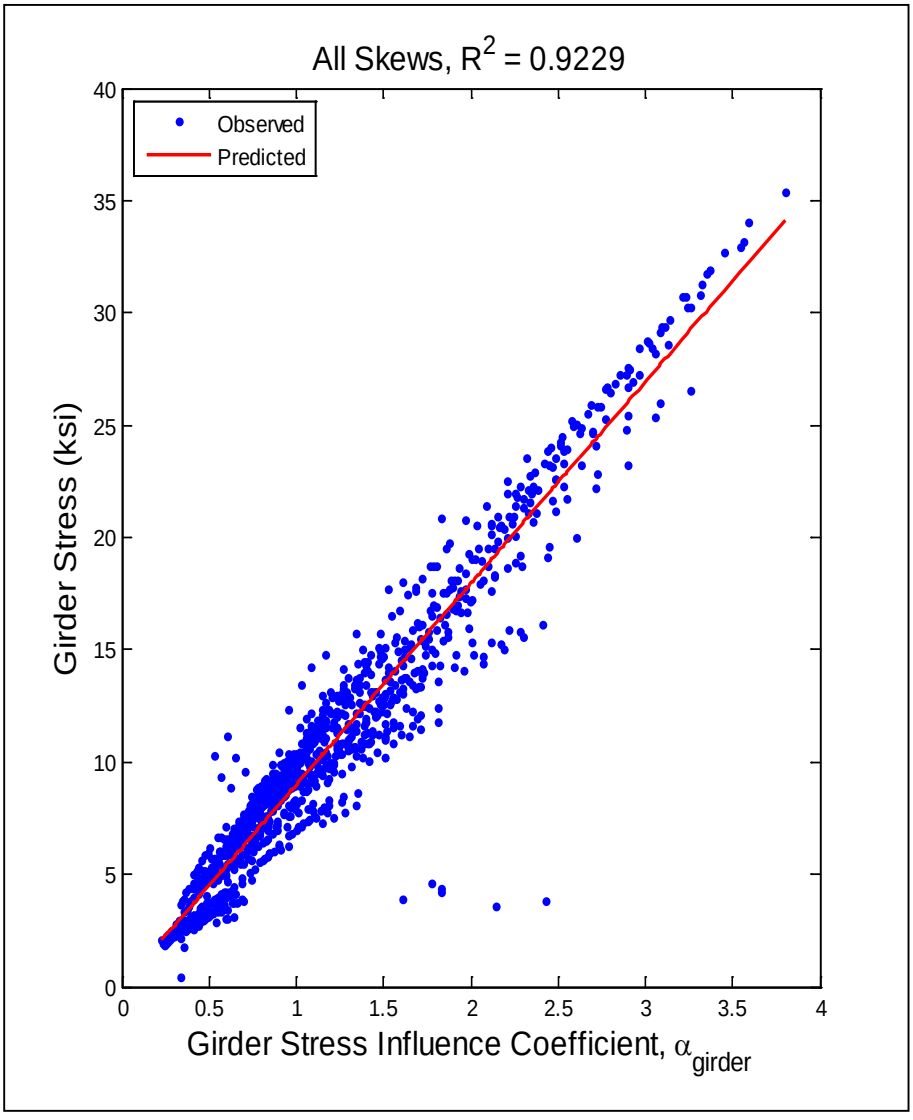

Figure 52. Girder stress data from parametric models against developed linear curve.

7.2 PILE CHARTS

Pile charts are a current tool used for the design of IAB behavior; however, they are limited by the fact that they oversimplify nonlinear behavior exhibited by the bridge. If the desire is to present a chart that is applicable to all bridges, a rotational stiffness value may be used that is sufficient to enforce an essential fixed rotational restraint on the abutment. This would be conservative for bridges with low rotational stiffness values. Other variables would still need to be accounted for though, which is why tools such as the nonlinear regression for pile strains in the previous section might prove to be more useful.

Nevertheless, comparisons can still be made with the data from the parametric study and the current IDOT pile charts. Figures 54 through 62 display pile charts generated by results from the base parametric study, along with the current IDOT curves (please note that three sets of data are all together on top of each other along the x-axis in Figure 54). Again, all load factors were set to unity in this study, and no load factors were used in the computation of pile strains. As the charts display, there is more flexibility on applicable EELs when some pile yielding is allowed. It should be noted that isolated cases fall below the IDOT recommended curves for a given allowable yield limit.

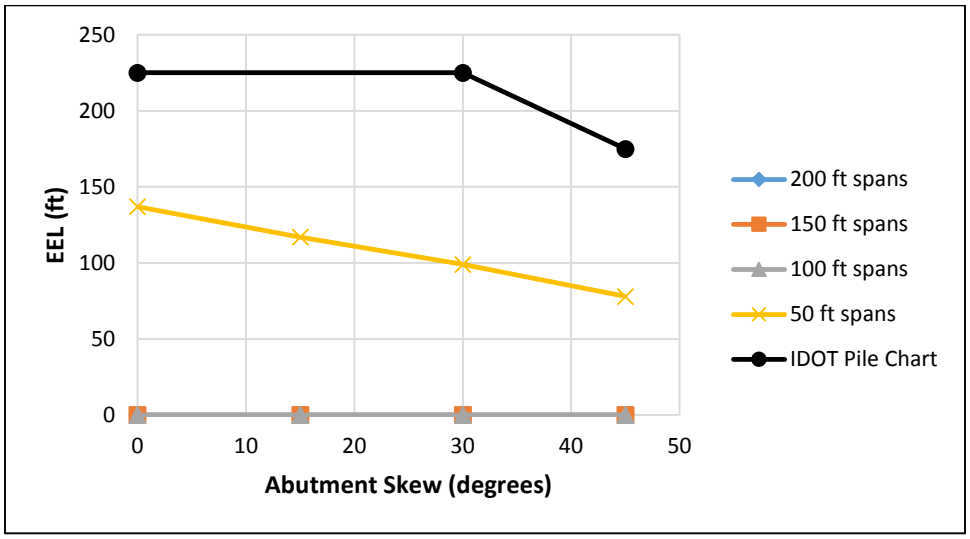

Figure 53. HP14×73 pile chart limiting strains at first yield under HL93-EXP loading.

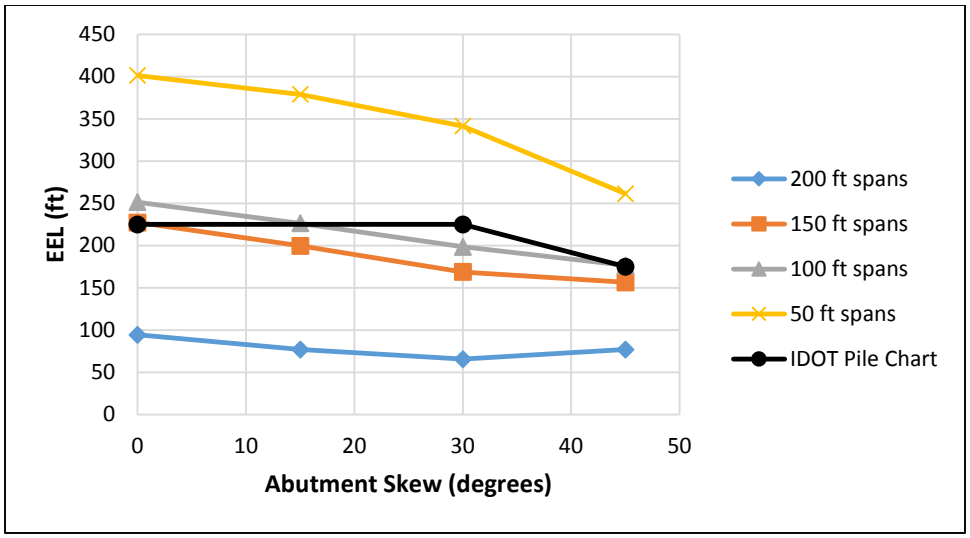

Figure 54. HP14×73 pile chart limiting strains to 3× yield under HL93-EXP loading.

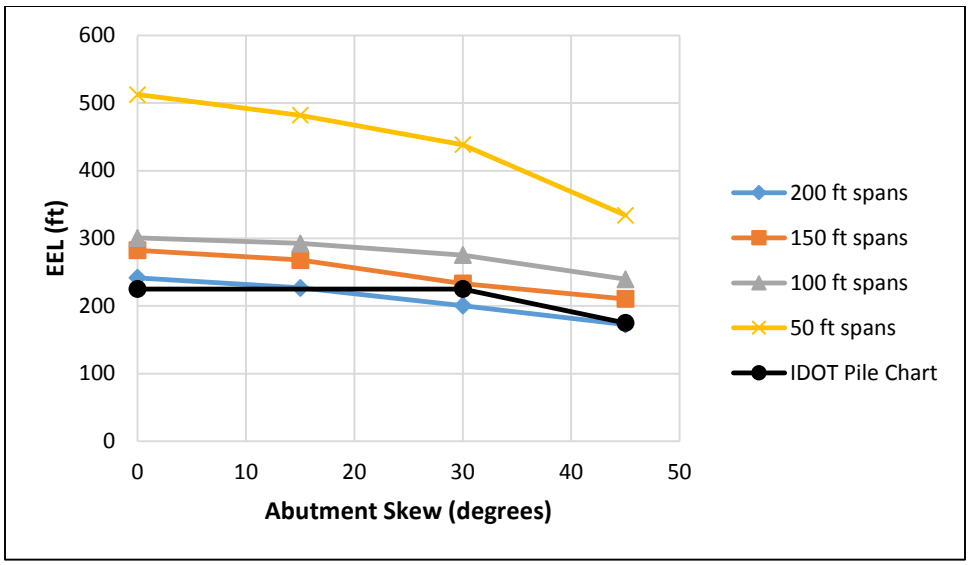

Figure 55. HP14×73 pile chart limiting strains to 5× yield under HL93-EXP loading.

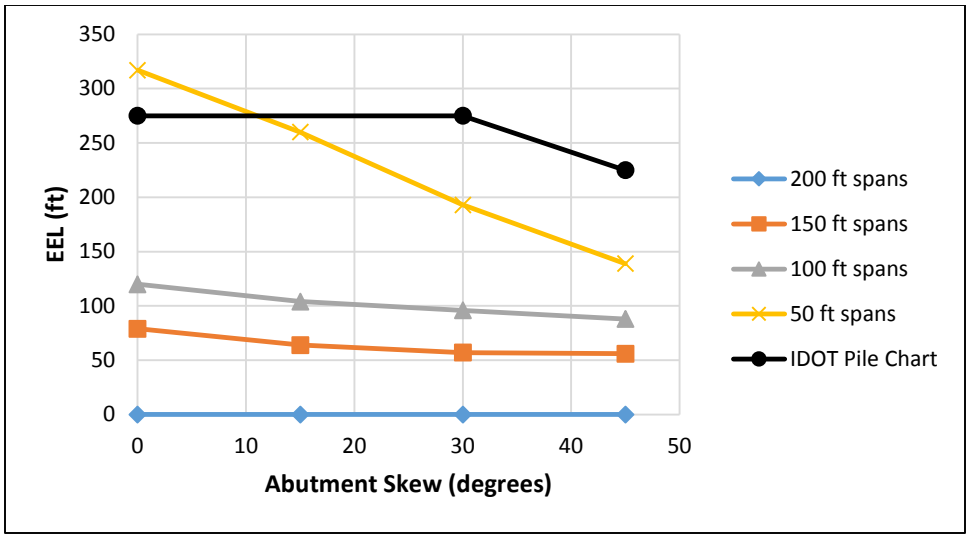

Figure 56. HP14×117 pile chart limiting strains to first yield under HL93-EXP loading.

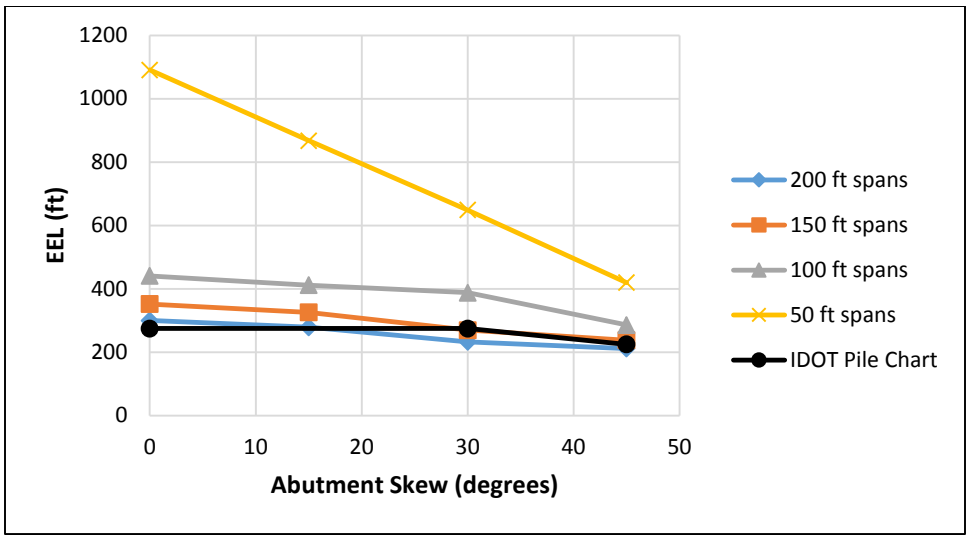

Figure 57. HP14×117 pile chart limiting strains to 3× yield under HL93-EXP loading.

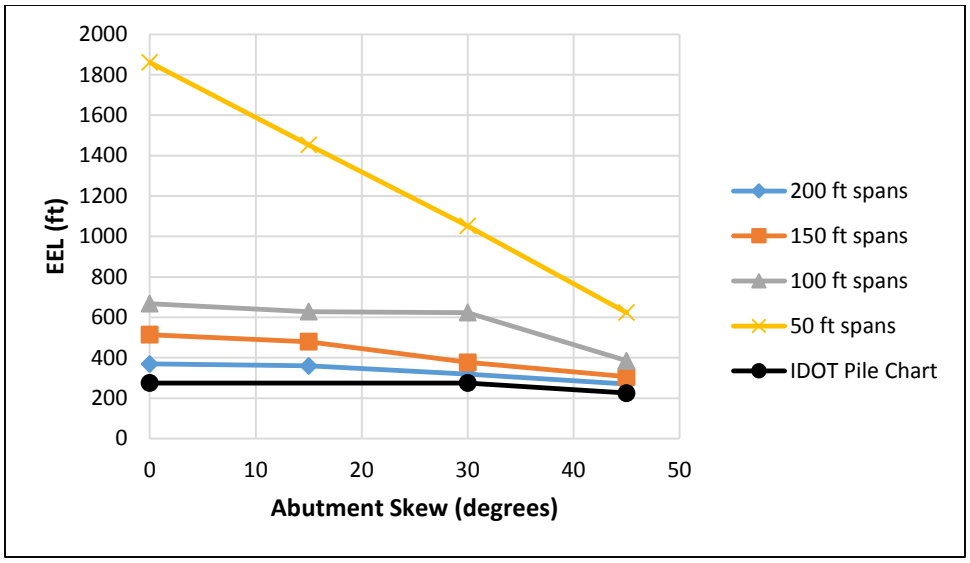

Figure 58. HP14×117 pile chart limiting strains to 5× yield under HL93-EXP loading.

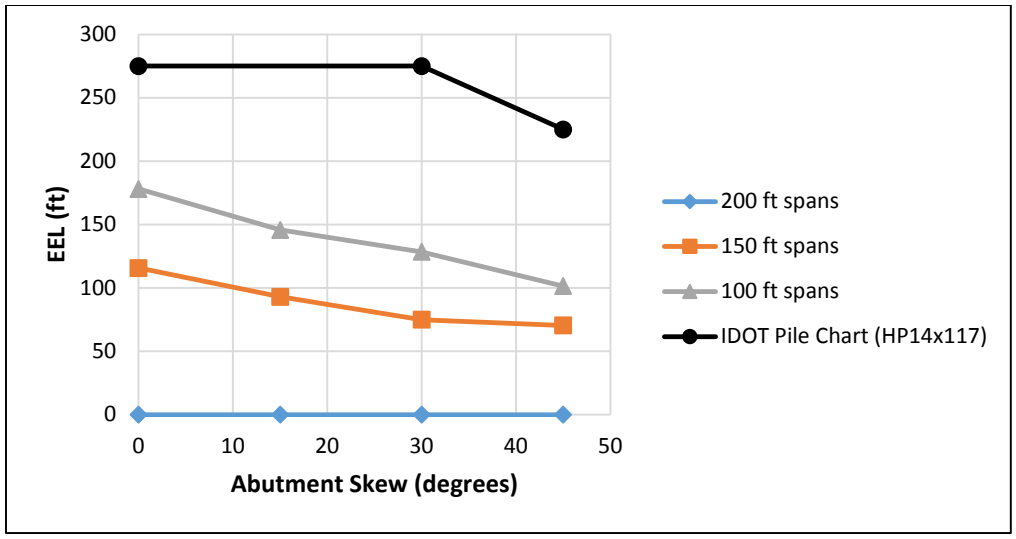

Figure 59. HP18×135 pile chart limiting strains to first yield under HL93-EXP loading.

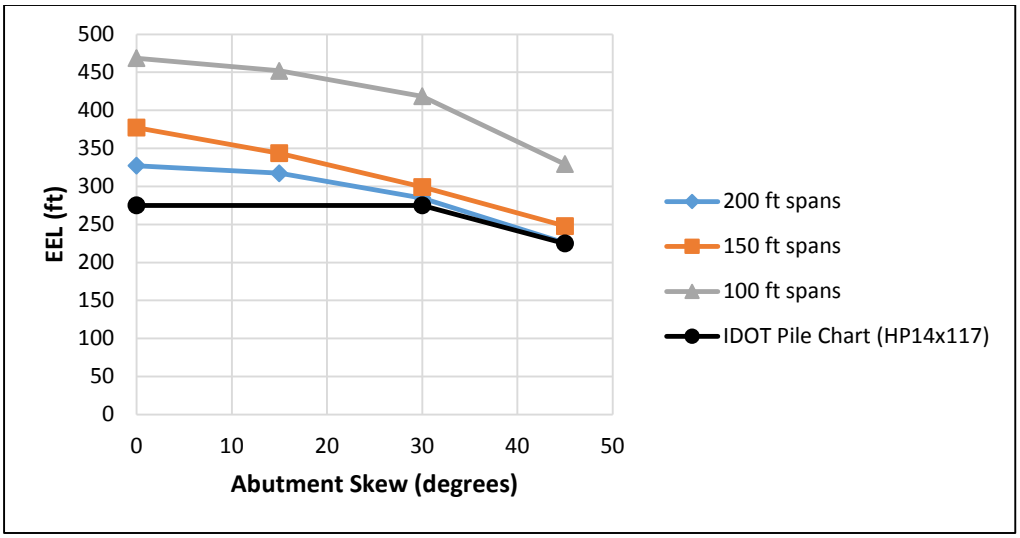

Figure 60. HP18×135 pile chart limiting strains to 3× yield under HL93-EXP loading.

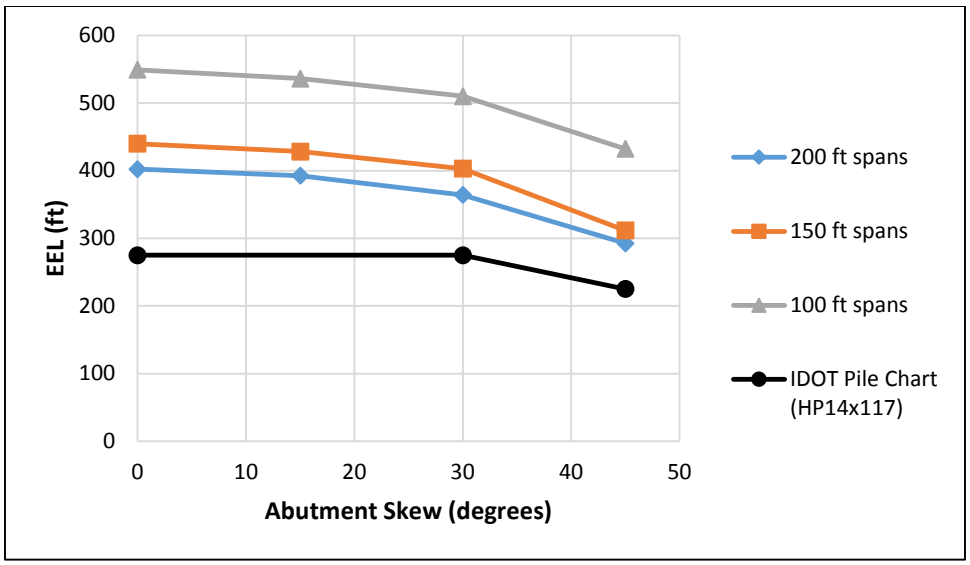

Figure 61. HP1×135 pile chart limiting strains to 5× yield under HL93-EXP loading.

7.3 STRIP SEAL DETAILS

IDOT currently employs a strip seal to accommodate bridge movement at the end of the approach slab. The strip seals can accommodate up to 2 in. of movement in either direction. This limiting value corresponds to a non-skew bridge of approximately 700 ft. This length is still moderately far beyond what IDOT currently allows for overall bridge length, but preliminary results have indicated that bridges longer than 700 ft are certainly possible with proper pile selection and abutment reinforcement detailing. Therefore, it would be prudent for IDOT to at least investigate and consider the use of different expansion joint details for the end of the approach slab that can accommodate more movement.

7.4 RECOMMENDATIONS FOR USE OF LARGER PILE SIZES

IDOT instructed the Illinois researchers to investigate the behavior of the larger HP piles as well as larger metal shell piles. Early investigations have shown the pile strains to be significantly lower in bridges with larger piles. As indicated in Chapter 6, pipe piles are not as advantageous as HP sections because peak pile strains significantly increase upon the onset of yielding. Therefore, pipe pile sections should be used with caution, keeping in mind the findings discussed in the previous chapter. However, larger H-pile sections, namely HP16s and HP18s, are extremely feasible for implementation in IAB design. Assuming the increased forces and moments can be accommodated by the abutment and the superstructure, larger piles will allow for IABs with significantly longer EELs.

CHAPTER 8: CONCLUSIONS

Numerical models were created in order to better understand the behavior of IABs under uniform temperature changes. Three key bridge responses that may control design are bridge displacement at deck level; strains that develop in the piles, which may behave inelastically due to integral abutment construction; and additional stresses that develop in the composite girder system. Results from the base set of bridge models, which consisted of composite steel plate girders and H-pile foundations, show that bridge longitudinal movement can be estimated as 90% of free expansion of the superstructure, regardless of pile stiffness, superstructure rotational stiffness, or abutment skew. Increased bridge skew acts to amplify displacements at the acute corner. Because bridges with large EELs are seen to exhibit movement greater than what is allowed by the 2 in. strip seal detail employed by IDOT, it may be beneficial to explore other expansion joint options. Additionally, with increasing skew and bridge length, extreme fiber strains of the pile head generally increase, although pile strain limits beyond yield strain can allow for permissible IAB lengths to increase, especially with the use of larger pile sections. As long as abutment detailing allows for proper transfer of the increased superstructure demand from the larger pile sizes, the use of piles such as HP16s and HP18s could be beneficial for long bridges. Unlike what is experienced by the piles, increasing skew is seen to generally relieve girder demands by reducing strong-axis bending of the girder. Thus, non-skew bridges were the most critical for girder stresses, with the highest demands resulting from bridges with large EELs and large pile sizes.

The secondary parameter study shows how the primary results might be altered if site conditions were changed from the default. End-span ratio affects the value of the superstructure rotational stiffness, k_θ. Increasing k_θ for a given girder design increases both pile strains and girder stresses. When combined with skew, increasing the width of an IAB beyond the default of 36 ft can significantly increase the pile demands. Additionally, pile demands may be decreased by stiffer backfill, softer pile foundation soils, pile top relief, double piles, and deeper abutments. Pipe piles and strong axis–oriented H-piles provide more lateral stiffness, but pile stiffness sharply decreases after the onset of yielding, which is undesirable.

Design tools and recommendations were established based on the findings of this study, which will be further elaborated on in conjunction with the IAB field instrumentation program in a companion second report, including even more discussion on key design parameters. The equations developed for predicting pile strains and girder stresses can be used by designers as an initial estimate as to the magnitude of these values before a detailed model is created. Currently, IDOT employs pile charts for the pile design selection process. Comparable charts were created with findings from this study; however, such charts are somewhat limited in nature and do not capture the true nonlinear IAB behavior. It would be more beneficial to consider parameters other than EEL and bridge skew in the selection of pile size.

REFERENCES

American Association of State Highway and Transportation Officials (AASHTO). 2012. *LRFD Bridge Design Specifications*, 6th ed., Washington, D.C.: AASHTO, 2012.

Burdette, E.G., Deatherage, J.H., and Goodpasture, D.W. 1999. "Behavior of Laterally Loaded Piles Supporting Bridge Abutments – Phase I," Final Report, Tennessee Department of Transportation Project TNSPR-RES1081. Knoxville: Center for Transportation Research, University of Tennessee, Knoxville.

Burdette, E. G., E. E. Ingram, J. B. Tidwell, D. W. Goodpasture, J. H. Deatherage, and S. C. Howard. 2004. "Behavior of Integral Abutments Supported by Steel H-Piles." *Transportation Research Record*, 1892, pp. 24–28.

Chang, L. M., and Y. Lee. 2001. "Evaluation and Policy for Bridge Deck Expansion Joints." Publication FHWA/IN/JTRP-2000/01. Joint Transportation Research Program, Indiana Department of Transportation and Purdue University, West Lafayette, IN.

Civjan, S. A., C. Bonczar, S. F. Brena, J. DeJong, and D. Crovo. 2007. "Integral Abutment Bridge Behavior: Parametric Analysis of a Massachusetts Bridge." *Journal of Bridge Engineering*, ASCE, 12(1), pp. 64–71.

Computers and Structures, Inc. (CSI). 2009. SAP2000 Advanced 14.1.0 Structural Analysis Program, Berkeley, CA. http://www.csiamerica.com/

Computers and Structures, Inc. (CSI). 2013. CSI Knowledge Base, 2013. http://www.csiamerica.com

Department of the Navy. 1971. *Soil Mechanics, Foundations, and Earth Structures*. Alexandria, VA: Department of the Navy, Naval Facilities Engineering Command.

Dicleli, M. 2005. "Integral Abutment-Backfill Behavior on Sand Soil – Pushover Analysis Approach." *Journal of Bridge Engineering*, ASCE, 10(3), pp. 354–364.

Ensoft, Inc. 2005. *LPILE Plus v.5.0 Geotechnical Analysis Program (Student Version)*, http://www.ensoftinc.com

Fennema, J. L., J. A. Laman, and D. G. Linzell. 2005. "Predicted and Measured Response of an Integral Abutment Bridge." *Journal of Bridge Engineering*, ASCE, 10(6), pp. 666–677.

Frosch, R. J., V. Chovichien, K. Durbin, and D. Fedroff. 2006. "Jointless and Smoother Bridges: Behavior and Design of Piles." Publication FHWA/IN/JTRP-2004/24. Joint Transportation Research Program, Indiana Department of Transportation and Purdue University, West Lafayette, IN.

Frosch, R. J., and M. D. Lovell. 2011. *Long-Term Behavior of Integral Abutment Bridges*. Publication FHWA/IN/JTRP-2011/16. Joint Transportation Research Program, Indiana Department of Transportation and Purdue University, West Lafayette, IN. doi: 10.5703/1288284314640.

Huang, J., C. French, and C. Shield. *Behavior of Concrete Integral Abutment Bridges*. Nov. 2004. Rep. Minnesota Local Road Research Board, http://www.cts.umn.edu/Publications/ ResearchReports/reportdetail.html?id=967

Huang J., C. K. Shield, and C. E. W. French. 2008. “Parametric Study of Concrete Integral Abutment Bridges.” *Journal of Bridge Engineering*, ASCE, 13(5), pp. 511–526.

Illinois Department of Transportation (IDOT). 2012. *Bridge Manual*. IDOT Bureau of Bridges and Structures, Springfield, IL.

“IDOT Memorandum: 2012 Integral Abutment Bridge Policies and Details.” Jul. 25, 2012. Illinois Department of Transportation Bureau of Bridges and Structures, http://www.idot.illinois.gov/Assets/uploads/files/Doing-Business/Memorandums-&-Letters/Highways/Bridges/ABD-Memos/abd123.pdf

Ingram, E. E., E. G. Burdette, D. W. Goodpasture, J. H. Deatherage, and R. M. Bennett. 2004. “Behavior of Steel H-Piles Supporting Integral Abutments.” *Proceedings of the ASCE Structures Congress*, Nashville, TN, pp. 219–225.

Iowa Department of Transportation (Iowa DOT). 2012. *LRFD Bridge Design Manual*. Office of Bridges and Structures, Ames, IA.

Khodair, Y. A., and S. Hassiotis. 2005. “Analysis of Soil-Pile Interaction in Integral Abutment.” *Computers and Geotechnics*, 32, pp. 201–209.

Kim, W., and J. A. Laman. 2010. “Numerical Analysis Method for Long-Term Behavior of Integral Abutment Bridges,” *Engineering Structures*, 32, pp. 2247–2257.

Olson, S.M., Long, J.H., Hansen, J.R., Renekis, D., and LaFave, J.M. 2009. “Modification of IDOT Integral Abutment Design Limitations and Details,” Illinois Center for Transportation Research Report, ICT-09-054. Illinois Center for Transportation, Rantoul, IL.

Olson, S. M., K. P. Holloway, J. M. Buenker, J. H. Long, and J. M. LaFave. 2012. “Thermal Behavior of IDOT Integral Abutment Bridges and Proposed Design Modifications.” Illinois Center for Transportation Research Report, ICT-12-022. Illinois Center for Transportation, Rantoul, IL.

Paul, M.D., J.A. Laman, and D.G. Linzell. 2005. “Thermally Induced Superstructure Stresses in Prestressed Girder Integral Abutment Bridges.” *Journal of the Transportation Research Board*, CD 11-S. Transportation Research Board of the National Academies, Washington, D.C., pp. 287–297.

Rodriguez, L. E., P. J. Barr, and M. W. Halling. 2014. “Temperature Effects on a Box-Girder Integral-Abutment Bridge.” *Journal of Performance of Constructed Facilities*, ASCE, 28(3), pp. 583–591.

William, G. W., S. N. Shoukry, and M. Y. Riad. 2012. “Study of Thermal Stresses in Skewed Integral Abutment Steel Girder Bridges.” *Structural Engineering International*, 22(3), pp. 308–317.


Illinois Department
of Transportation


ILLINOIS
UNIVERSITY OF ILLINOIS AT URBANA-CHAMPAIGN